2020 年度（令和二年度） 博士論文

-博士論文-

Study on High Quality bulk GaN Single Crystal Growth by Halide Vapor Phase Epitaxy

ハライド気相成長法による 高品質バルク GaN 単結晶成長に関する研究

名古屋大学 工学研究科

電子工学専攻 博士後期課程

劉 強

（天野 研究室）

Abstract

High quality freestanding GaN wafers are in strong demand to improve state-of-the-art III-Nitride optoelectronic, electronic and RF devices. However, due to the high melting points and high equilibrium N_2 over pressures at high temperatures, growth of bulk GaN is extremely challenging. Comparing with ammonothermal method and flux method, Halide vapor phase epitaxy (HVPE) is the most promising technique for mass production. HVPE is the most cost-effective method due to its favorable growth conditions, namely, low pressure and relatively low growth temperature, high growth rate and ability to high purity material.

This dissertation studied thick epilayer growth by HVPE on native GaN seed with high crystallinity, low threading dislocation density and small lattice bow. Epilayers were grown on seeds fabricated with different methods, namely Na-flux method, ammonothermal method and HVPE method, and the epilayers on different seeds were studied and compared. The most important issue for realizing thick GaN epilayer growth is the stress control, especially the stress caused by various edge effects ranging from spurious growth on the edges or formation of facets. By using W ring to protect the edge, eventually 2.3 mm crack free thick GaN epilayer was grown.

This dissertation also introduced the reactor with showerhead configuration and independent controlled inner and outer flow for large size wafer growth. For large size wafer growth, uniform growth on a large area becomes an innegligible issue. The uniform growth was achieved on 4-inch wafer by optimizing the inner and outer flow balance. To further improve the performance of the showerhead, simulation was used

to optimize the showerhead design. The experiment result with the new showerhead fits with the simulation result.

Contents

Chapter 1

1 Introduction

1.1 Freestanding GaN substrate and its application

Nitride-based devices fabricated with hetero-epitaxial GaN layers on foreign substrates such as sapphire, silicon carbide, and silicon have significantly limited performance. This is mainly due to the disadvantages of the hetero-epitaxy, such as lattice mismatch, thermal expansion coefficient mismatch and chemical incompatibility leading to high-dislocation density, mosaic crystal structure, biaxial induced stress, and wafer bowing. Efforts were done to reduce these structural defects. Special methods have been developed such as low temperature buffer technologies, epitaxial lateral overgrowth techniques, etc., but these methods will complicate and extend the device growth process. Additional drawbacks are related to the lower electrical and/or thermal conductivity of most foreign substrates, which require more complicated and expensive device designs. By applying freestanding GaN substrates, the device performance will be greatly improved because the structural defects can be greatly eliminated and a better vertical electrical and thermal conductivity can also be achieved. Furthermore, epitaxial growth process and device processing can be more cost-efficient because they can both be simplified by eliminating the need for low-temperature buffer layers.

However, due to the high cost of freestanding GaN substrate, currently there are only limited applications based on three branches of GaN devices, they are light emitting

devices, such as laser diodes (LDs) and high brightness light emitting diodes (HB-LEDs); vertical power devices, such as GaN Schottky diodes [1], p-n junction-based junction field effect transistors [2] and current aperture vertical electron transistors [3,4]; and RF devices fabricate on freestanding GaN substrates for the purpose of better performance and reliability.

The application of LDs has been widely used in projectors, Blu-ray disc writers and some application scenarios which require small size lasers in industrial and medical fields. HB-LEDs are used in lighting products such as car headlight, and table lamp. GaN power devices have the potential to apply in solar power inverters, EV/HEV cars and power supply and power factor correction (PFC). RF devices have been already applied in phased array radars, and soon they can also be applied in 5G communication systems. The applications and devices based on freestanding GaN substrate have been summarized in Figure 1.1.

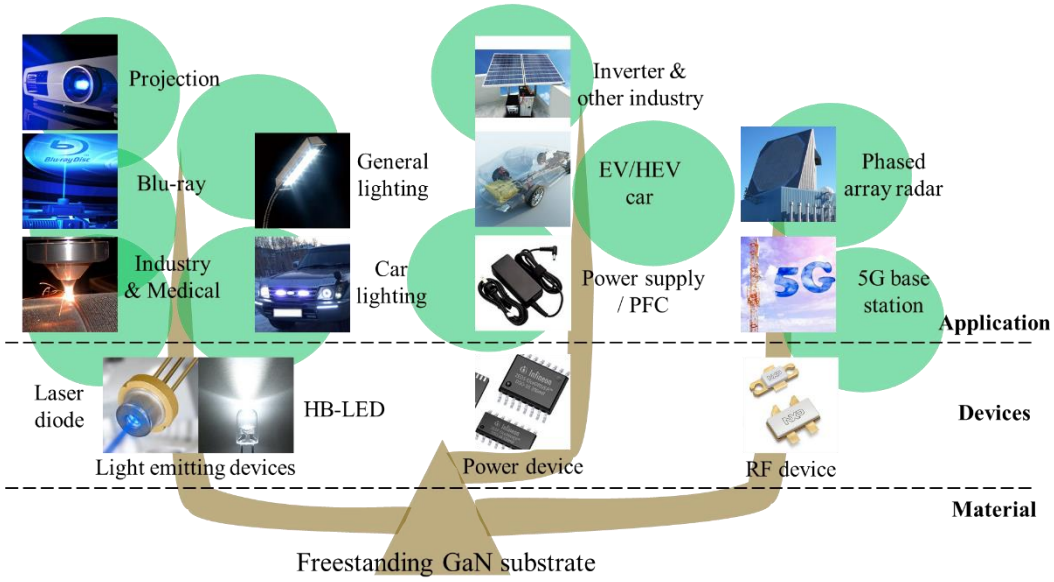

Figure 1.1 Applications and devices based on freestanding GaN substrate.

1.2 Methods of growing GaN freestanding substrate

1.2.1 A history of GaN crystal growth

Table 1.1 Summary of history of GaN crystal growth

Contribution	Year	Researcher	Country
First report of GaN structure	1937	Lirman	German
First report about GaN synthesis	1938	Juza, Hahn	German
First GaN growth by HVPE	1969	Maruska, Tietjen	USA
First GaN growth by MOVPE	1971	Manasevit	USA
First GaN growth by PVT	1980	Vodakov	Russian
First GaN growth by HPSG	1982	Porowski	Poland
First GaN growth by MBE	1983	Yoshida	Japan
First GaN growth by ammonothermal	1995	Dwiliński	Poland
First GaN growth by Na-flux	2000	Yamane	Japan

Gallium nitride (GaN) crystal structure was firstly reported in 1937 by Lirman and Zhdanov [5], but the first GaN synthesis was reported by Juza and Hahn in 1938 [6]. They observed GaN needles when NH_3 flew through hot Ga metal at 1200 ºC. Later in 1959, Grimmeiss and Koelmans also produced small GaN crystal in the same way [7]. After that in 1969, Maruska and Tietjen synthesize a large area layer of GaN on sapphire by firstly flowing HCl through Ga then react with NH_3 [8], this is the first reported halide vapor phase epitaxial (HVPE) method of GaN synthesis. In 1971, Manasevit has reported syntesis of GaN layers by metalorganic vapor phase epitaxial (MOVPE) method [11]. In 1980, GaN sublimation method (PVT) was reported by Vodakov [9]. In 1982, Porowski successfully obtained GaN crystal with high quality (dislocation density < 10^6 cm^{-2}) by flowing N_2 through Ga metal at high temperature (1700 ºC) and high pressure (2 GPa (20 kbar)). At approximately the same time in 1983, Yoshida found the GaN quality can be improved grown on AlN/sapphire by molecular beam epitaxy (MBE) method [10]. The first ammonothermal growth of GaN was reported by Dwiliński in 1995 [12], unlike the solution growth based on a Ga melt, ammonothermal

growth uses supercritical NH_3 as a solvent. Yamane et al. reported successful growth of GaN using a Na flux method in 2000 [13]. The main GaN crystallization methods were all proposed as summarized in Table 1.1, and these methods kept developing respectively.

1.2.2 Methods to fabricate freestanding GaN substrate

Due to high melting points and high equilibrium N_2 pressure at high temperature as shown in Figure 1.2, growth of bulk GaN from liquid is extremely difficult unless under high pressure over 6 GPa and high temperature over 2200 ºC. But due to a high demand for homoepitaxial substrates for III-nitride devices and its large potential market, alternative methods were developed.

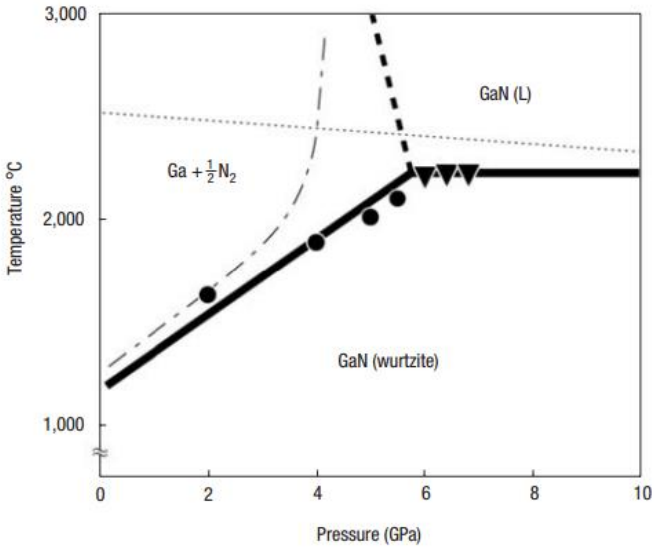

Figure 1.2 Phase diagram of GaN under high pressure and temperature [14].

Currently there are mainly three kinds of methods that can produce commercially available GaN substrates, and they have their own pros and cons.

1.2.2.1 Flux method

Flux method is an alternative method of high-pressure solution growth (HPSG) method proposed by Porowski in 1982. In the HPSG method, high pressure (1.2 to 2 GPa) and high temperature (1400 to 1700 ˚C) was used. By employing alkali or alkali

earth metal as a flux, the Na flux reduces the growth pressure down to the order of 10 MPa and the temperature down to 700 ˚C [13]. In addition, it was reported that the growth pressure could be reduced to 1 MPa by adding Ca into Na-Ga melt [15]. The Li-Ga melt is also investigated [16].

Up to now, there are totally three generations of Na-flux technique [17], (the first generation [18-20], the second generation [21-23], and the third generation [24]).

The size of substrate made by this method is larger than 2-inch, threading dislocation density (TDD) in Na-Flux GaN substrate is in the order of $10^3 - 10^5$ cm^{-2}, the growth rate for Na-flux method is in the order of 10^1 μm/h, and the O background impurity concentration is in the level of 10^{17} cm^{-3} [17,24].

1.2.2.2 Ammonothermal Growth

Ammonothermal method was initially motivated by the successful application of hydrothermal growth to the production of quartz (α-SiO_2) and ZnO [25]. By using of supercritical ammonia instead of water, GaN crystal can be grown under pressure below 0.6 GPa and temperature in the range of 400 to 750 ˚C [26,27]. And unlike the solution growth based on a Ga melt, ammonothermal growth uses supercritical NH_3 as a solvent. Some mineralizers are added to ammonia in order to accelerate its dissociation and enhance the solubility of Ga or GaN.

Currently there are two type of ammonothermal method determined by the choice of mineralizers [28]. Basic ammonothermal growth makes use of alkali metals or their amides as mineralizers (NH_2^- ions are introduced into the supercritical solution) [26,29,30], while in acidic ammonothermal growth halide compounds are present (NH_4^+ ions are introduced into the supercritical solution) [27].

Ammonothermal technique allows large-scale wafer growth and scalable production approach by conducting multiple seeded growths in a single run. The curvature of

samples with diameter up to 2 inches has been measured to be more than 1000 m. The typical TDD in the order of 10^4 cm^{-2}, O and Si background impurity concentration in the order of 10^{18} and 10^{17} cm^{-3}, respectively [28]. However, the maximum growth rate for all direction is in the order of 10^1 μm/h [31].

1.2.2.3 Halide vapor phase epitaxy (HVPE)

HVPE method for GaN crystal growth was firstly introduced by Maruska and Tietjen in 1969 [8]. In typical HVPE, GaCl and NH_3 are used as precursors. GaCl is synthesized by flowing HCl over a heated Ga melt in the reactor. The typical growth temperature is about 1000 ˚C and the temperature of the Ga melt is about 800 ˚C. The growth is usually carried out under atmospheric pressure. The fundamental growth physics and chemistry of HVPE growth of GaN are well understood. The available models [32,33] of the kinetics of the process and growth mechanisms occurring at the solid/vapor interface during HVPE growth of GaN assume a surface process involving several steps and allow simulation of the growth rates. Based on a quasi-thermodynamic growth model, simulations of gas dynamics, temperature distribution, and partial pressures can be simulated for any specific reactor design [34-36].

Most of the commercially available GaN substrate in the market are fabricated by separating HVPE-grown GaN thick layers on foreign substrates. The main challenges of this process are dislocation reduction and stress control. Several techniques have been developed. Epitaxial lateral overgrowth (ELOG) [37,38], dislocation elimination by epitaxial growth with inverse-pyramidal pits (DEEP) [39,40], and nano-mask [41] method are commonly used to enhance the dislocation annihilation for dislocation reduction and help to release the growth and thermal stress. Besides, in order to separate the quasi-bulk epilayers from foreign substrate, there are usually two methods: void-assisted separation (VAS) based self-separation method [42-49] and laser lift-off method.

Recently, O and Si background impurity concentration were also successfully decreased to the level of 10^{16} cm^{-3} in quartz-free HVPE reactor [50], the threading dislocation density (TDD) of HVPE GaN substrate is in the order of 10^{6} cm^{-2} [51]. Although many techniques were applied to control the stress, the lattice bow is still very large.

The required growth condition and the quality of commercially available freestanding GaN substrate fabricated by three different methods have been summarized in Table 1.2.

Table 1.2 The-state-of-the-art quality of commercially available freestanding GaN substrate fabricated by three different methods

Conditions/Capability	Unit	HVPE	Ammonothermal	Na-flux
Growth pressure	MPa	0.1	100-600	5-10
Growth temperature	˚C	950-1100	500-800	700-900
Wafer size	inch	2~6	1 - 2	1 - 7
Largest boule size Diameter/Height	inch/mm	2/10	2/10	1/12
Growth rate level	μm/h	10^{2}	10^{1}	10^{1}
Dislocation density level	cm-2	10^{6}	10^{4}	10^{3} - 10^{5}
O concentration level	cm-3	10^{16}	10^{18}	10^{17}
Si concentration level	cm-3	10^{16}	10^{17}	Not exist
Lattice bow	M	2 – 20	> 1000	> 30

1.3 Approach of this research

In this study, we are aiming to develop a technology to fabricate high quality freestanding GaN substrate. High crystallinity, high purity, low TDD, small lattice bow is mostly expected.

Current GaN freestanding substrates by HVPE has significant disadvantages. Firstly, the process cost is high because HVPE is an open system. Therefore, source gas can be wasted during mass transportation process. Secondly, throughput of wafer to wafer

process is not efficient. Thirdly, stress control, dislocation reduction and separation of GaN epilayers from foreign substrate are very difficult.

In order to overcome some of these problems, countermeasures were done. Firstly, vertical HVPE systems was employed in this study because they have much higher source gas yield than a horizontal one. Secondly, we are trying to obtain thick GaN boules that can be sliced to fabricate native bulk substrates. Thirdly, high quality native GaN seed with low TDD, high crystallinity and small lattice bow was used to cancel dislocation reduction and separation problems. With these countermeasures, the only difficulty in this study is the stress control during thick homoepitaxial growth.

And to further solve above problems, efforts were done in this study. Firstly, growth condition in HVPE was systematically studied. Fluid dynamic models and thermal dynamic calculations were combined to find the way to improve source gas yield. Secondly, native GaN substrate fabricated by different methods were compared to select the best seed with lowest TDD, highest crystallinity and smallest lattice bow. Thirdly, the thickness limitation of homoepitaxial growth was attributed to non-polar and semi-polar growth of "wings", which will lead to formation of large stress in the growing crystal close to the edges [52]. Therefore, rings with materials that can decompose GaN crystal was designed at edge to prevent lateral growth in non-polar and semi-polar directions. Additionally, to further increase the freestanding wafer size and improve the source gas yield, the showerhead of another vertical reactor for large size wafer growth was studied and optimized.

1.4 Dissertation overview

1.4.1 Contribution of this work

1.4.1.1 Route selection to true bulk GaN crystal

Among all the bulk growth techniques under investigation today for nitrides, HVPE is still the most promising technique due to mainly three reasons. Firstly, it utilizes a process at more favorable conditions, namely, low pressure and relatively low growth temperature. Secondly, the growth rate is at least one order of magnitude higher than other methods. Thirdly, the purity is the highest and still have potential to be further improved by further optimization of the reactor. However, there are also shortcomings for this method. Firstly, the source gas yield is low because the reactor is an open system, part of the source gas will waste during mass transportation process. Secondly, the stress control during growth is still facing problems. By considering these pros and cons comprehensively, HVPE is still the most cost-effective method.

According to analysis of the strain generation mechanism in HVPE epilayers, by applying native seed with high crystallinity, low TDD and small lattice bow, similar epilayers can be copied at a high growth rate.

In summary, the route to obtain true bulk GaN crystal by this approach is most promising.

1.4.1.2 Thick epilayer growth

Among commercially available seeds fabricated with different methods, ammonothermal seed is the most promising one.

Although there is no direct observation, by analyzing the stress generation mechanism and excluding the impossible reasons, various edge effects ranging from

spurious growth on the edges or formation of facets is considered as the main cause of stress. A similar view was also proposed by other researchers in Ref. [53].

The phenomenon appeared at interface during homoepitaxial growth on native GaN seed fabricated with different substrate are different, which is neither yet studied nor optimized by changing growth parameters. This will be an interesting direction to further research.

In this study, Tungsten (W) ring was used to try to decompose lateral growth in non-polar and semi-polar directions, but it is not very effective. Crystal still will crack after approximately 2 mm growth, and the wings was also observed by cross sectional view of SEM image. An effective countermeasure to deal with this challenge is still under research.

1.4.1.3 Parasitic deposition prevention

Parasitic deposition was prevented by extra barrier flow. However, this method will trade-off the gas mixing distance and further decrease source gas yield and growth rate.

Using metal and their compound with catalyst effect such as W, Ru, Mo, and WC is another effective method to prevent parasitic deposition in the reactor. Furthermore, the catalyst effect of W can be improved after several cycles of aging. It is hopefully to prevent parasitic deposition by simply using aged W metals.

Besides, the impurity introduced by W metal was not systematically studied yet, and this method is waiting for further research.

1.4.1.4 Large size wafer growth

A prototype reactor with showerhead configuration was introduced.

By employing the design of independently controlled inner and outer flow, uniformity can be optimized by changing the flow balance.

The area ratio of inner region and outer region can be further optimized to 0.94 by simulation, and experimental demonstration is waiting for further research.

1.4.2 Chapter composition of this dissertation

In Chapter 1, I explained that the demand for freestanding GaN substrates is increasing more and more. A history of GaN crystal growth was surveyed, and commercially available GaN fabrication methods were also compared. Objective of this research is trying to develop a technology to fabricate high quality freestanding GaN substrate with high crystallinity, high purity, low TDD and small lattice bow. Thick GaN epitaxial growth on high quality native seeds by HVPE method was employed to approach the aim.

In Chapter 2, growth condition in HVPE was systematically studied, fluid dynamic models and thermal dynamic calculations were combined to find the way to improve source gas yield.

In Chapter 3, native GaN substrate fabricated by different methods were compared to select the best seed with lowest TDD, highest crystallinity and smallest lattice bow. GaN on ammonothermal substrate was expected. Thick epitaxial growth technologies including protection rings, seed fixation, long time growth and regrowth was studied. Finally, a 3.5 mm thick GaN finally achieved with regrowth method.

In Chapter 3, native GaN substrate fabricated by different methods were compared to select the best seed with lowest TDD, highest crystallinity and smallest lattice bow. GaN on ammonothermal substrate was expected. Thick epitaxial growth technologies including protection rings, seed fixation, long time growth and regrowth was studied.

In Chapter 4, the reactor for large size wafer crystal was introduced. Optimized growth condition was obtained. The ability to decompose GaN crystal was found to be enhanced after cycles of aging procedure. From long time growth result, we concluded

parasitic deposition can be prevented by only W plate. Showerhead version II was designed based on this concept, and changes were done to decrease the mixing distance. By simulation study, the optimized area ratio of inner to outer region was 0.94. A new showerhead was fabricated based on the simulation result shown at last.

In Chapter 5, the dissertation was concluded and further improvement ideas was proposed in two research directions in thick epilayer growth and large size wafer growth.

1.5 References

[1] *R.P. Tompkins, M.R. Khan, R. Green, K.A. Jones, J.H. Leach, IVT measurements of GaN power Schottky diodes with drift layers grown by HVPE on HVPE GaN substrates, J. Mater. Sci. Mater. Electron. 27 (2016) 6108–6114. https://doi.org/10.1007/s10854-016-4536-z.*

[2] *H. Fujikura, K. Hayashi, F. Horikiri, Y. Narita, T. Konno, T. Yoshida, H. Ohta, T. Mishima, Elimination of macrostep-induced current flow nonuniformity in vertical GaN PN diode using carbon-free drift layer grown by hydride vapor phase epitaxy, Appl. Phys. Express. 11 (2018) 045502. https://doi.org/10.7567/APEX.11.045502.*

[3] *H. Nie, Q. Diduck, B. Alvarez, A.P. Edwards, B.M. Kayes, M. Zhang, G. Ye, T. Prunty, D. Bour, I.C. Kizilyalli, 1.5-kV and 2.2-mΩ-cm2 Vertical GaN Transistors on Bulk-GaN Substrates, IEEE Electron Device Lett. 35 (2014) 939–941. https://doi.org/10.1109/LED.2014.2339197.*

[4] *S. Chowdhury, Vertical Gallium Nitride Technology, in: M. Meneghini, G. Meneghesso, E. Zanoni (Eds.), Power GaN Devices Mater. Appl. Reliab., Springer International Publishing, Cham, 2017: pp. 101–121. https://doi.org/10.1007/978-3-319-43199-4_5.*

[5] *J.V. Lirman, H.S. Zhdanov, First reported GaN structure, in: Acta Physicochim. URSS, Academy of Sciences of the U.S.S.R., 1937: p. 306.*

[6] *R. Juza, H. Hahn, Über die Kristallstrukturen von Cu3N, GaN und InN Metallamide und Metallnitride, Z. Für Anorg. Allg. Chem. 239 (1938) 282–287. https://doi.org/10.1002/zaac.19382390307.*

[7] *H.G. Grimmeiss, H. Koelmans, Über die Kantenemission und andere Emissionen des GaN, Z. Für Naturforschung A. 14 (1959) 264–271. https://doi.org/10.1515/zna-1959-0309.*

[8] *H.P. Maruska, J.J. Tietjen, THE PREPARATION AND PROPERTIES OF VAPOR-DEPOSITED SINGLE-CRYSTAL-LINE GaN, Appl. Phys. Lett. 15 (1969) 327–329. https://doi.org/10.1063/1.1652845.*

[9] *Y.A. Vodakov, M.I. Karklina, E.N. Mokhov, A.D. Roenkov, Growth of GaN epitaxial layers on sapphire and SiC substrates, Inorg. Mater. 16 (1980) 537.*

[10] *S. Yoshida, S. Misawa, S. Gonda, Epitaxial growth of GaN/AlN heterostructures, J. Vac. Sci. Technol. B Microelectron. Process. Phenom. 1 (1983) 250–253. https://doi.org/10.1116/1.582496.*

[11] H.M. Manasevit, F.M. Erdmann, W.I. Simpson, The Use of Metalorganics in the Preparation of Semiconductor Materials: IV . The Nitrides of Aluminum and Gallium, J. Electrochem. Soc. 118 (1971) 1864. https://doi.org/10.1149/1.2407853.

[12] R. Dwiliński, A. Wysmo\lek, J. Baranowski, M. Kamińska, R. Doradziński, J. Garczyński, L. Sierzputowski, H. Jacobs, GaN synthesis by ammonothermal method, Acta Phys. Pol. A. 88 (1995) 833–836.

[13] M. Aoki, H. Yamane, M. Shimada, T. Sekiguchi, T. Hanada, T. Yao, S. Sarayama, F.J. DiSalvo, Growth of GaN single crystals from a Na–Ga melt at 750°C and 5MPa of N2, J. Cryst. Growth. 218 (2000) 7–12. https://doi.org/10.1016/S0022-0248(00)00518-2.

[14] W. Utsumi, H. Saitoh, H. Kaneko, T. Watanuki, K. Aoki, O. Shimomura, Congruent melting of gallium nitride at 6 GPa and its application to single-crystal growth, Nat. Mater. 2 (2003) 735–738. https://doi.org/10.1038/nmat1003.

[15] F. Kawamura, T. Iwahashi, M. Morishita, K. Omae, M. Yoshimura, Y. Mori, T. Sasaki, Growth of transparent, large size GaN single crystal with low dislocations using Ca-Na flux system, Jpn. J. Appl. Phys. 42 (2003) L729.

[16] W.J. Wang, X.L. Chen, Y.T. Song, W.X. Yuan, Y.G. Cao, X. Wu, Assessment of Li–Ga–N ternary system and GaN single crystal growth, J. Cryst. Growth. 264 (2004) 13–16.

[17] Y. Mori, M. Imanishi, K. Murakami, M. Yoshimura, Recent progress of Na-flux method for GaN crystal growth, Jpn. J. Appl. Phys. 58 (2019) SC0803. https://doi.org/10.7567/1347-4065/ab112e.

[18] Y. Mori, M. Imade, M. Maruyama, M. Yoshimura, H. Yamane, F. Kawamura, T. Kawamura, Na flux 1st generation, in: Handb. Cryst. Growth Bulk Cryst. Growth Basic Tech. Growth Mech. Dyn. 2nd Ed Ed P Rudolph, Amsterdam: Elsevier, 2015: p. 505.

[19] M. Imade, Y. Hirabayashi, Y. Konishi, H. Ukegawa, N. Miyoshi, M. Yoshimura, T. Sasaki, Y. Kitaoka, Y. Mori, Growth of large GaN single crystals on high-quality GaN seed by carbon-added Na flux method, Appl. Phys. Express. 3 (2010) 075501.

[20] F. Kawamura, M. Morishita, N. Miyoshi, M. Imade, M. Yoshimura, Y. Kitaoka, Y. Mori, T. Sasaki, Study of the metastable region in the growth of GaN using the Na flux method, J. Cryst. Growth. 311 (2009) 4647–4651.

[21] M. Imanishi, K. Murakami, H. Imabayashi, H. Takazawa, Y. Todoroki, D. Matsuo, M. Maruyama, M. Imade, M. Yoshimura, Y. Mori, Coalescence Growth of Dislocation-Free GaN Crystals by the Na-Flux Method, Appl. Phys. Express. 5 (2012) 095501.

[22] M. Imanishi, K. Murakami, H. Imabayashi, H. Takazawa, Y. Todoroki, D. Matsuo, M. Maruyama, M. Imade, M. Yoshimura, Y. Mori, Coalescence growth of GaN crystals on point seed crystals using the Na flux method, Phys. Status Solidi C. 10 (2013) 400–404.

[23] M. Imade, M. Imanishi, Y. Todoroki, H. Imabayashi, D. Matsuo, K. Murakami, H. Takazawa, A. Kitamoto, M. Maruyama, M. Yoshimura, Fabrication of low-curvature 2 in. GaN wafers by Na-flux coalescence growth technique, Appl. Phys. Express. 7 (2014) 035503.

[24] M. Imanishi, K. Murakami, T. Yamada, K. Kakinouchi, K. Nakamura, T. Kitamura, K. Okumura, M. Yoshimura, Y. Mori, Promotion of lateral growth of GaN crystals on point

seeds by extraction of substrates from melt in the Na-flux method, Appl. Phys. Express. 12 (2019) 045508. https://doi.org/10.7567/1882-0786/ab0db6.

[25] K. Byrappa, M. Yoshimura, Handbook of Hydrothermal Technology, Cambridge University Press, 2008.

[26] R. Dwiliński, R. Doradziński, J. Garczyński, L.P. Sierzputowski, A. Puchalski, Y. Kanbara, K. Yagi, H. Minakuchi, H. Hayashi, Excellent crystallinity of truly bulk ammonothermal GaN, J. Cryst. Growth. 310 (2008) 3911–3916. https://doi.org/10.1016/j.jcrysgro.2008.06.036.

[27] Y. Mikawa, T. Ishinabe, S. Kawabata, T. Mochizuki, A. Kojima, Y. Kagamitani, H. Fujisawa, Ammonothermal growth of polar and non-polar bulk GaN crystal, in: Gallium Nitride Mater. Devices X, International Society for Optics and Photonics, 2015: p. 936302.

[28] M. Zajac, R. Kucharski, K. Grabianska, A. Gwardys-Bak, A. Puchalski, D. Wasik, E. Litwin-Staszewska, R. Piotrzkowski, J. Z Domagala, M. Bockowski, Basic ammonothermal growth of Gallium Nitride – State of the art, challenges, perspectives, Prog. Cryst. Growth Charact. Mater. 64 (2018) 63–74. https://doi.org/10.1016/j.pcrysgrow.2018.05.001.

[29] R. Dwiliński, R. Doradziński, J. Garczyński, L. Sierzputowski, R. Kucharski, M. Zając, M. Rudziński, R. Kudrawiec, W. Strupiński, J. Misiewicz, Ammonothermal GaN substrates: Growth accomplishments and applications, Phys. Status Solidi A. 208 (2011) 1489–1493.

[30] R. Dwilinski, R. Doradzinski, J. Garczynski, L.P. Sierzputowski, M. Zajac, M. Rudzinski, Homoepitaxy on bulk ammonothermal GaN, J. Cryst. Growth. 311 (2009) 3058–3062.

[31] M. Saito, D.S. Kamber, T.J. Baker, K. Fujito, S.P. DenBaars, J.S. Speck, S. Nakamura, Plane Dependent Growth of GaN in Supercritical Basic Ammonia, Appl. Phys. Express. 1 (2008) 121103. https://doi.org/10.1143/APEX.1.121103.

[32] R. Cadoret, A. Trassoudaine, Growth of gallium nitride by HVPE, J. Phys. Condens. Matter. 13 (2001) 6893–6905. https://doi.org/10.1088/0953-8984/13/32/302.

[33] Koukitu, N. Takahashi, H. Seki, Thermodynamic Study on Metalorganic Vapor-Phase Epitaxial Growth of Group III Nitrides, Jpn. J. Appl. Phys. 36 (1997) L1136–L1138. https://doi.org/10.1143/JJAP.36.L1136.

[34] A.S. Segal, A.V. Kondratyev, S.Yu. Karpov, D. Martin, V. Wagner, M. Ilegems, Surface chemistry and transport effects in GaN hydride vapor phase epitaxy, J. Cryst. Growth. 270 (2004) 384–395. https://doi.org/10.1016/j.jcrysgro.2004.07.018.

[35] C.E.C. Dam, A.P. Grzegorczyk, P.R. Hageman, R. Dorsman, C.R. Kleijn, P.K. Larsen, The effect of HVPE reactor geometry on GaN growth rate—experiments versus simulations, J. Cryst. Growth. 271 (2004) 192–199. https://doi.org/10.1016/j.jcrysgro.2004.07.059.

[36] Ł.J. Sytniewski, A.A. Lapkin, Sergey. Stepanov, W.N. Wang, CFD optimisation of up-flow vertical HVPE reactor for GaN growth, J. Cryst. Growth. 310 (2008) 3358–3365. https://doi.org/10.1016/j.jcrysgro.2008.04.017.

[37] Usui, H. Sunakawa, A. Sakai, A.A. Yamaguchi, Thick GaN Epitaxial Growth with Low Dislocation Density by Hydride Vapor Phase Epitaxy, Jpn. J. Appl. Phys. 36 (1997) L899. https://doi.org/10.1143/JJAP.36.L899.

[38] K. Hiramatsu, K. Nishiyama, A. Motogaito, H. Miyake, Y. Iyechika, T. Maeda, Recent Progress in Selective Area Growth and Epitaxial Lateral Overgrowth of III-Nitrides: Effects of Reactor Pressure in MOVPE Growth, Phys. Status Solidi A. 176 (1999) 535–543.

[39] K. Motoki, T. Okahisa, R. Hirota, S. Nakahata, K. Uematsu, N. Matsumoto, Dislocation reduction in GaN crystal by advanced-DEEP, J. Cryst. Growth. 305 (2007) 377–383. https://doi.org/10.1016/j.jcrysgro.2007.03.038.

[40] K. MOTOKI, Development of Gallium Nitride Substrates, SEI Tech Rev. (2010) 8.

[41] J. Huang, K. Xu, X.J. Gong, J.F. Wang, Y.M. Fan, J.Q. Liu, X.H. Zeng, G.Q. Ren, T.F. Zhou, H. Yang, Dislocation cross-slip in GaN single crystals under nanoindentation, Appl. Phys. Lett. 98 (2011) 221906. https://doi.org/10.1063/1.3593381.

[42] Y. Oshima, T. Eri, M. Shibata, H. Sunakawa, A. Usui, Fabrication of Freestanding GaN Wafers by Hydride Vapor-Phase Epitaxy with Void-Assisted Separation, Phys. Status Solidi A. 194 (2002) 554–558.

[43] Y. Oshima, T. Eri, M. Shibata, H. Sunakawa, K. Kobayashi, T. Ichihashi, A. Usui, Preparation of Freestanding GaN Wafers by Hydride Vapor Phase Epitaxy with Void-Assisted Separation, Jpn. J. Appl. Phys. 42 (2003) L1. https://doi.org/10.1143/JJAP.42.L1.

[44] C. Hennig, E. Richter, M. Weyers, G. Tränkle, Self-separation of thick two inch GaN layers grown by HVPE on sapphire using epitaxial lateral overgrowth with masks containing tungsten, Phys. Status Solidi C. 4 (2007) 2638–2641.

[45] T. Yoshida, Y. Oshima, T. Eri, K. Ikeda, S. Yamamoto, K. Watanabe, M. Shibata, T. Mishima, Fabrication of 3-in GaN substrates by hydride vapor phase epitaxy using void-assisted separation method, J. Cryst. Growth. 310 (2008) 5–7.

[46] F. Lipski, T. Wunderer, S. Schwaiger, F. Scholz, Fabrication of freestanding 2 "-GaN wafers by hydride vapour phase epitaxy and self-separation during cooldown, Phys. Status Solidi A. 207 (2010) 1287–1291.

[47] W. Luo, J. Wu, J. Goldsmith, Y. Du, T. Yu, Z. Yang, G. Zhang, The growth of high-quality and self-separation GaN thick-films by hydride vapor phase epitaxy, J. Cryst. Growth. 340 (2012) 18–22.

[48] T. Sato, S. Okano, T. Goto, T. Yao, R. Seto, A. Sato, H. Goto, Nearly 4-inch-diameter free-standing GaN wafer fabricated by hydride vapor phase epitaxy with pit-inducing buffer layer, Jpn. J. Appl. Phys. 52 (2013) 08JA08.

[49] V. Nikolaev, A. Golovatenko, M. Mynbaeva, I. Nikitina, N. Seredova, A. Pechnikov, V. Bougrov, M. Odnobludov, Effect of nano-column properties on self-separation of thick GaN layers grown by HVPE, Phys. Status Solidi C. 11 (2014) 502–504.

[50] H. Fujikura, T. Konno, T. Yoshida, F. Horikiri, Hydride-vapor-phase epitaxial growth of highly pure GaN layers with smooth as-grown surfaces on freestanding GaN substrates, Jpn. J. Appl. Phys. 56 (2017) 085503. https://doi.org/10.7567/JJAP.56.085503.

[51] K. Fujito, S. Kubo, H. Nagaoka, T. Mochizuki, H. Namita, S. Nagao, Bulk GaN crystals grown by HVPE, J. Cryst. Growth. 311 (2009) 3011–3014. https://doi.org/10.1016/j.jcrysgro.2009.01.046.

[52] M. Amilusik, D. Wlodarczyk, A. Suchocki, M. Bockowski, Micro-Raman studies of strain in bulk GaN crystals grown by hydride vapor phase epitaxy on ammonothermal GaN seeds, Jpn. J. Appl. Phys. 58 (2019) SCCB32. https://doi.org/10.7567/1347-4065/ab1390.

[53] M. Bockowski, M. Iwinska, M. Amilusik, M. Fijalkowski, B. Lucznik, T. Sochacki, Challenges and future perspectives in HVPE-GaN growth on ammonothermal GaN seeds, Semicond. Sci. Technol. 31 (2016) 093002. https://doi.org/10.1088/0268-1242/31/9/093002.

Chapter 2

2 Flow calculation, simulation and growth condition optimization in a vertical HVPE reactor

2.1 Homemade HVPE reactor

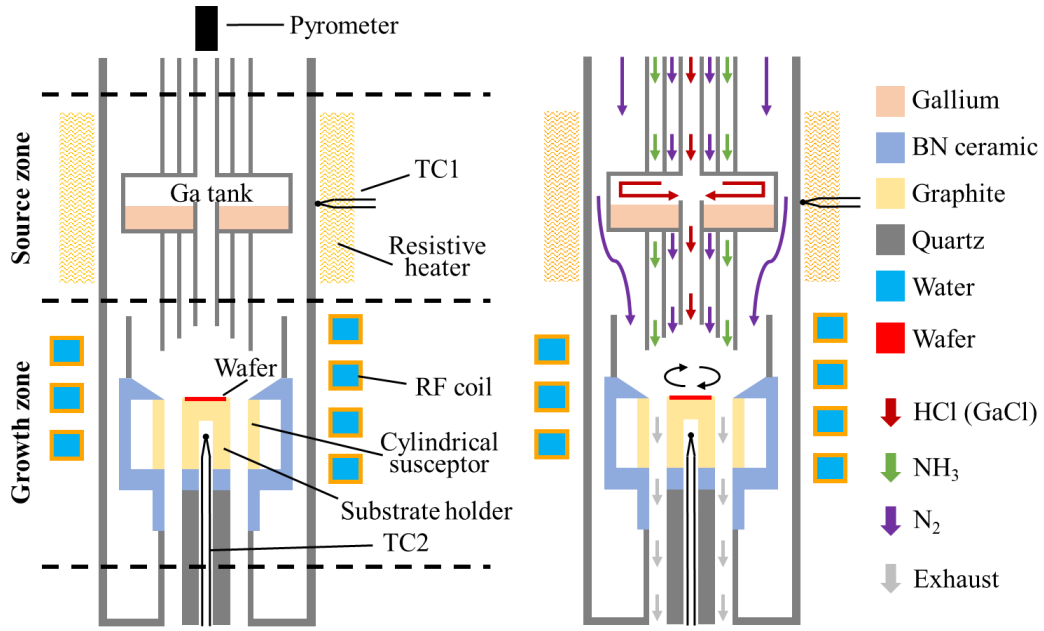

Figure 2.1 Schematic diagram of homemade reactor, (left) structure, (right) flow and material list.

The schematic of the reactor is shown in Figure 2.1. The Ga metal in the source zone was heated resistively and the temperature was controlled by a thermocouple in contact

with the quartz reactor wall. Herein, liquid Ga reacted with HCl to form GaCl. The growth zone, where GaN crystal growth occurred, was heated by RF power coupled into a cylindrical graphite susceptor. The temperature of the graphite substrate holder was controlled by a thermocouple placed in the center of the holder about 10 mm below the surface. A pyrometer with a spot size of ~10 mm was used to monitor the surface temperature of the center of the rotating wafer during growth.

The process gases entered the reactor through the top inlets and were exhausted at the bottom. They were injected into the growth zone through three concentric nozzles: GaCl was supplied through the center nozzle, N_2 flowing through the middle nozzle was used as a separation gas to delay the reaction between the Ga and nitrogen species and to prevent parasitic deposition on the injection nozzles, while NH_3 was injected through the outer most nozzle. Deposition on the inner quartz reactor wall was minimized by an N_2 curtain gas flow.

2.2 Pre-reaction optimization

The pre-reaction in HVPE reactor is necessary because GaCl is not stable below 420 ºC, which will spontaneously self-react to form a stable low-temperature gallium trichloride ($GaCl_3$) and excess gallium metal, so GaCl cannot be easily kept in a high-pressure bottle like other source gases. To study the pre-reactions in Ga tank, thermal dynamic calculation was employed.

The chemical reactions and corresponded equilibrium constants are listed in formula 2.1 to 2.4.

$$Ga(l) + HCl(g) \leftrightarrow GaCl(g) + \frac{1}{2}H_2(g) \qquad K_1 = \frac{P_{GaCl}P_{H_2}^{\frac{1}{2}}}{P_{HCl}} \qquad 2.1$$

$$Ga(l) + 2HCl(g) \leftrightarrow GaCl_2(g) + H_2(g) \qquad K_2 = \frac{P_{GaCl_2}P_{H_2}}{P_{HCl}^2} \qquad 2.2$$

$$Ga(l) + 3HCl(g) \leftrightarrow GaCl_3(g) + \frac{3}{2}H_2(g) \qquad K_3 = \frac{P_{GaCl_3} P_{H_2}^{\frac{3}{2}}}{P_{HCl}} \qquad 2.3$$

$$2GaCl_3(g) \leftrightarrow Ga_2Cl_6(g) \qquad K_4 = \frac{P_{Ga_2Cl_6}}{P_{GaCl_3}^2} \qquad 2.4$$

The thermal dynamic data of equilibrium constants K_1 to K_4 are calculated by formula 2.5.

$$K = e^{\frac{-\Delta G^0}{RT}} \qquad 2.5$$

where ΔG^0 is the Gibbs free energy change of the reaction taken at the standard pressure of 1 atm, R is the universal gas constant, and T is the reaction temperature. ΔG^0 is calculated from the thermal dynamic data listed in Appendix I.

The pressure in the tank universally equals to 100kPa. Because there is no deposition consisting of Cl, N and H atoms during the reactions, the gas phase molar quantity of Cl, N and H atoms conserves. The ratio of $n_{Cl}/(n_H + n_N)$ and $n_H/(n_H + n_N)$ remain constant at equilibrium state with the input values.

$$\sum P_i = P_{GaCl} + P_{GaCl_2} + P_{GaCl_3} + P_{Ga_2Cl_6} + P_{HCl} + P_{H_2} + P_{N_2} \qquad 2.6$$

$$A = \frac{P_{GaCl} + 2P_{GaCl_2} + 3P_{GaCl_3} + 6P_{Ga_2Cl_6} + P_{HCl}}{2P_{H_2} + P_{HCl} + 2P_{N_2}} \qquad 2.7$$

$$F = \frac{2P_{H_2} + P_{HCl}}{2P_{H_2} + P_{HCl} + 2P_{N_2}} \qquad 2.8$$

By considering formula of 2.1 to 2.8, the partial pressure of 7 species of gases at equilibrium state can be solved. Figure 2.2 shows the calculation results of equilibrium state changing with temperature, input HCl concentration and carrier gas. HCl conversion rate dependence is also plotted.

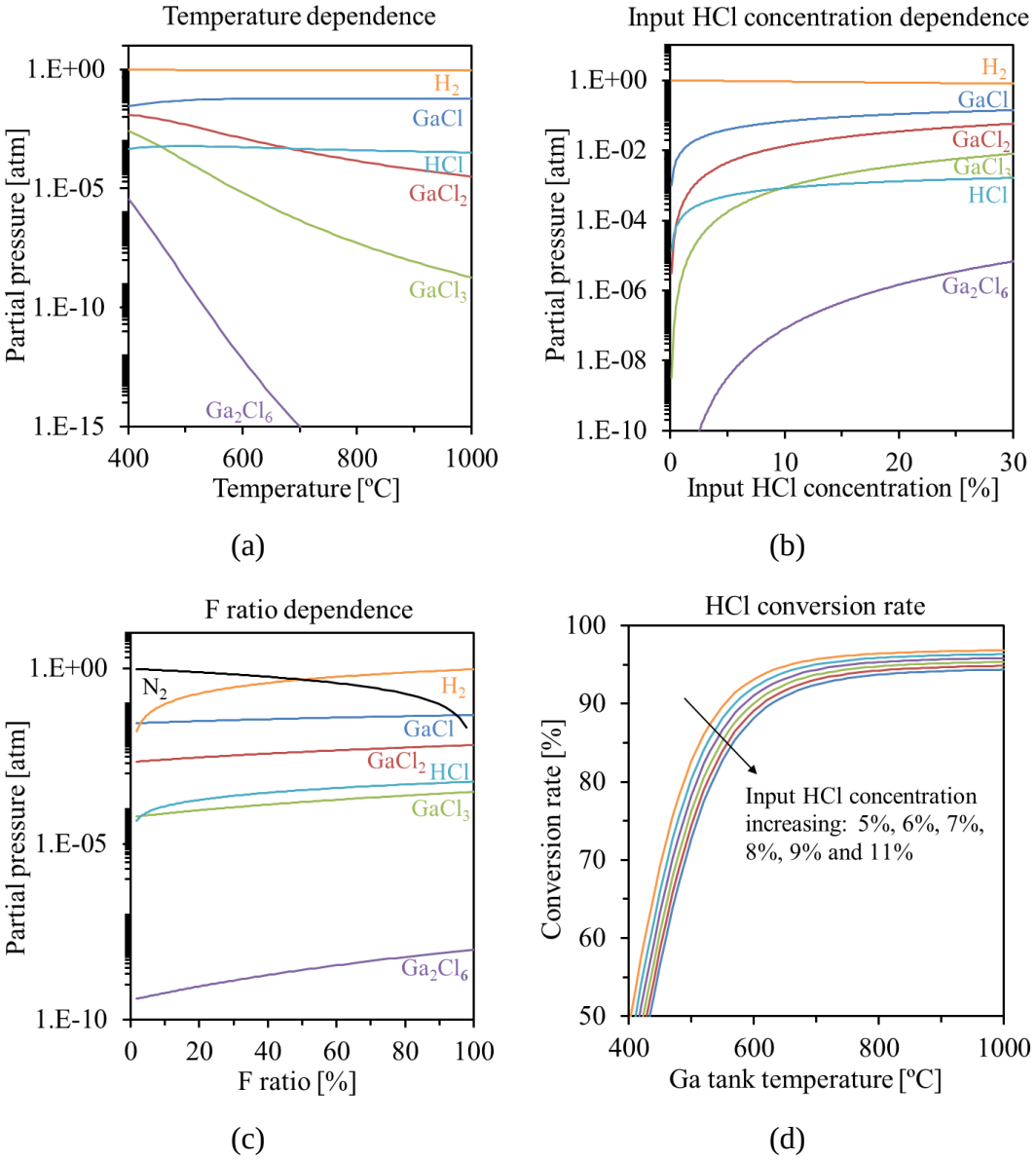

Figure 2.2 Thermal dynamic calculation result, partial of each species on the dependence of (a) temperature, (b) input HCl concentration and (c) F ratio; (d) HCl conversion rate dependence on different input HCl concentration and Ga tank temperature.

From Figure 2.2, it is known that to enhance HCl conversion rate, higher temperature, lower input HCl concentration and H_2 carrier gas is preferred. HCl conversion rate is higher than 90% with temperature over 700 ºC and input HCl concentration lower than 10%.

To apply the calculation in the actual situation, reaction gas duration time and diffusion length are necessary to take into consideration. The schematic diagram of this process is shown in Figure 2.3.

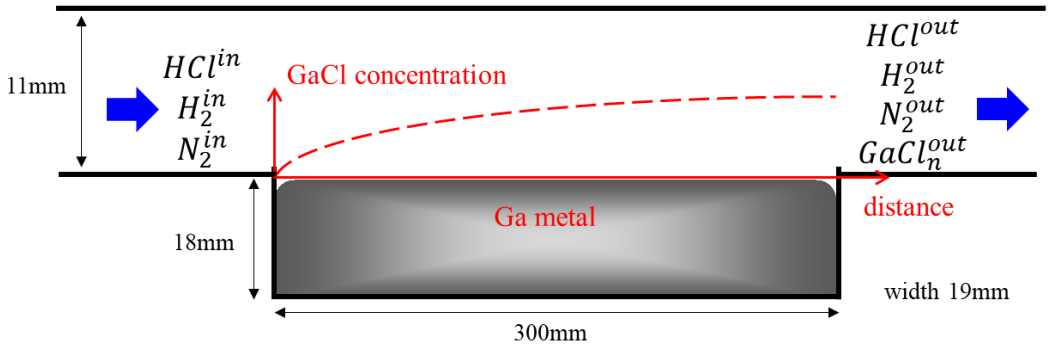

Figure 2.3 Reaction schematic diagram in the Ga tank, Ga tank of the actual can be simplified to a tunnel above Ga metal surface with height of 11 mm, length of 300 mm and width of 19 mm.

Reactant gas flows into the Ga tank from left side, reacts with Ga metal, and then the product gas mixture flows out from right side. Because the reaction only happens at Ga surface, concentration is distributed along vertical direction to Ga liquid surface. With flow moving rightward, diffusion will finally balance the GaCl concentration to an equilibrium state. To reach the equilibrium state, the reactant gas should have long enough time in the Ga tank, which constrains the maximum total flow rate. And the maximum total flow rate will affect the maximum HCl flow rate with keeping the input HCl concentration.

For an optimized Ga tank, the gas flow channel should be long enough to provide a relatively long reaction duration time. The Ga tank of the reactor used in this study can be simplified into a 300 mm length channel with width of 19 mm, the distance between Ga metal surface to channel top is 11 mm, and this can increase to maximum 29 mm with consumption of Ga metal, as shown in Figure 2.3.

One-dimensional advection-diffusion model can be used here to roughly estimate the diffusion in this Ga tank. Formula 2.9 is the analytical solution of the model [1],

$$\mathbf{C(x,t)} = \frac{\mathbf{C_0}}{\mathbf{2}}\left[\mathbf{erfc}\left(\frac{\mathbf{x-ut}}{\mathbf{2\sqrt{D_x t}}}\right) + \mathbf{e^{\frac{ux}{D_x}}erfc}\left(\frac{\mathbf{x+ut}}{\mathbf{2\sqrt{D_x t}}}\right)\right] \qquad 2.9$$

Where $C(x,t)$ is the concentration at position of x and time of t, C_0 is the input concentration, D is the diffusivity, and u is the advective flow velocity.

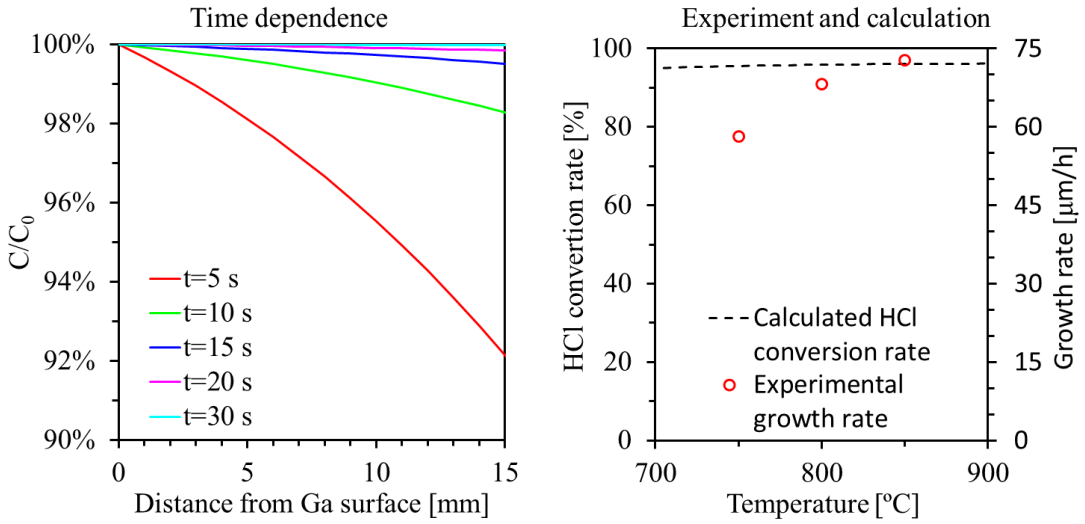

(a) (b)

Figure 2.4 (a) Calculation result of 1D advection-diffusion model, (b) Comparison of experiment result of growth rate and calculation result of HCl conversion rate.

Diffusivity of different gas species varies from 10^{-4} to 10^{-3} m^2/s [2], to calculate the maximum time, diffusivity is 10^{-4} m^2/s, the advection velocity is 8 mm/s. The calculated result is shown in Figure 2.4 (a). From the calculation, after 20 second, the concentration above Ga surface 11 mm will be the same to the concentration at Ga surface. With the simplified model of the Ga tank, when the total flow rate is fixed at 95 sccm, it requires 40s for the reactant gas flow through the channel across Ga surface. And this period is long enough to make the reaction in the Ga tank fully carried out.

Figure 2.4 (b) plots the experimental result. The three experiments were all with V/III ratio of 200, where NH_3 was saturated and the growth rate was only controlled by GaCl conversion rate. Ga tank temperature varied among 750 ºC, 800 ºC and 850 ºC, the growth rate (red circle) and calculated HCl conversion rate (break line) are plotted in Figure 2.4 (b). The growth rate was measured by SEM cross sectional with accuracy of ±1 μm.

The temperature dependence of experimental growth rate is much stronger than that of calculated HCl conversion rate. This may come from three reasons. Firstly, from Figure 2.1, the Ga tank temperature is taken by the thermocouple close to outer quartz wall, and there is no thermal isolation design at top and bottom of the heater, the actual temperature in Ga tank may be much lower. Secondly, lower HCl conversion rate will make the mixture gas from Ga tank consists more HCl. This may further decrease the growth rate at growth zone. Thirdly, The Ga tank temperature will also influence the flow speed in the system, higher flow speed from nozzle will also influence the growth rate. With above three reasons, the calculation deviate from experiment results.

The second and third reason are related to the reaction at growth zone and is too complex to discuss. Here I just fitted the experiment result with the calculation by estimating the actual temperature in Ga tank. As shown in Figure 2.5, by assuming the reaction temperature in Ga tank is 275 ºC lower than the thermocouple detected temperature, the experimental result well fitted with the calculation. In fact, the temperature in Ga tank may not be this lower, the deviation is the cumulative effect of above mentioned three reasons.

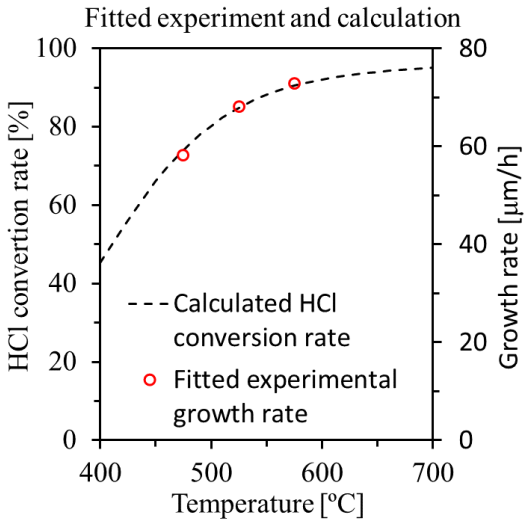

Figure 2.5 Fitted experimental growth rate with calculated HCl conversion rate, by assuming the actual reaction temperature at Ga surface is 275 °C lower than the thermocouple detected temperature

The total flow in the Ga tank is finally fixed to 95 sccm, and the temperature is fixed to 800 °C to reduce variables. The HCl flow rate in Ga tank can vary within 30 sccm (lower than 31.6%).

2.3 Flow optimization

The flow pattern in a vertical reactor can be described by stagnation point flow model as shown in Figure 2.6. Uniform vertical flow from nozzle transported to plate surface, the boundary layer thickness is uniform on the whole plate.

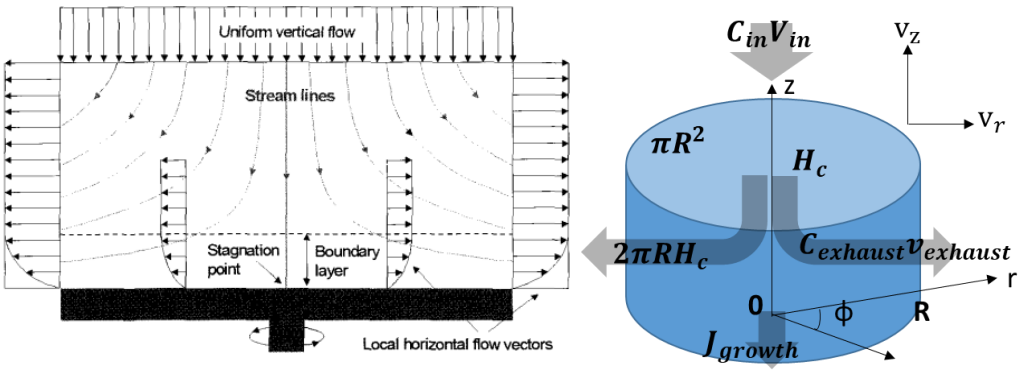

Figure 2.6 Stagnation flow model (a) from Ref. [3], (b) simplified model.

In order to make the result simple enough to derive an analytical expression for the gas velocity in a showerhead configuration under incompressible flow approximation, where the gas is incompressible (also ignoring thermal expansion) and volume in is the same as volume out, and vertical velocity of the bottom boundary (wafer surface) equals to 0. The vertical velocity at top boundary (inlet) is V_{in}, and concentration is C_{in}, the radius of the wafer is R, and height is H_C, exhaust gas outlet area is $2\pi RH_C$. To summarize the boundary conditions in cylindrical coordinates, we have,

$$\begin{cases} \mathbf{v_z}(\mathbf{r}, \boldsymbol{\varphi}, \mathbf{H_c}) = -\mathbf{V_{in}} \\ \mathbf{v_r}(\mathbf{r}, \boldsymbol{\varphi}, \mathbf{H_c}) = \mathbf{0} \\ \mathbf{c_{in}}(\mathbf{r}, \boldsymbol{\varphi}, \mathbf{H_c}) = \mathbf{C_{in}} \\ \mathbf{v_z}(\mathbf{r}, \boldsymbol{\varphi}, \mathbf{0}) = \mathbf{0} \end{cases} \tag{2.10}$$

and the flow is incompressible flow (the equivalent statement that implies incompressibility is that the divergence of the flow velocity is zero), so

$$\nabla \cdot v = \frac{1}{r}\frac{\partial}{\partial r}(rv_r) + \frac{\partial v_z}{\partial z} = 0 \tag{2.11}$$

from formula 2.11, we can solve the equation with the boundary conditions,

$$\begin{cases} v_z = v_{in}(-\dfrac{z}{H_c}) \\ v_r = v_{in}\dfrac{r}{2H_c} \end{cases} \tag{2.12}$$

In the analysis above, we didn't account the viscosity of the fluid. To further balance the convection and diffusion inside the chamber, we consider the concentrations of species are uniform radially in an ideal reactor, and transport in the vertical direction is decoupled from transport in the radial direction [4]. Because the concentration is uniform in r, the source gas carried in along a streamline from an inner point has the same concentration as the source gas that is leaving, except for the dependence on z.

From steady-state convection–diffusion equation

$$\nabla \cdot (D_i \nabla c_i) - \nabla \cdot (c_i \vec{v}) + R_i = \frac{\partial c_i}{\partial t} = 0 \quad 2.13$$

where index **i** denotes the **i**th species, **c** is the concentration (mol/m^3), **D** is the diffusivity, $\vec{v}$ is the velocity field that the quantity is moving with, **R** describes "sources" or "sinks" of the quantity. And because there is no sinks or source, so

$$D_i \nabla c_i - c_i \vec{v} = 0 \quad 2.14$$

As discussed above, the vertical velocity is approximately linear to position

$$v_z = -\frac{z}{H_c} v_{in} \quad 2.15$$

finally, we can have the following balance equation between diffusion and convection,

$$-v_{in} \frac{z}{H_c} \frac{\partial c_i}{\partial z} = D_i \frac{\partial^2 c_i}{\partial z^2} \quad 2.16$$

to solve the equation, we can have

$$c_i(z) = C_{in} \frac{erf(z/d)}{erf(H_c/d)} \quad 2.17$$

where

$$erf(x) = \frac{2}{\sqrt{\pi}} \int_0^x e^{-t^2} dt \quad 2.18$$

$$d = \sqrt{\frac{2DH_c}{v_{in}}} \quad 2.19$$

The input source gas is the sum of exhausted source gas and flux finally reached wafer surface, to integrate the exhausted gas

$$C_{exhaust} = \frac{1}{H_c} \int_0^{H_c} C(z, R) dz \quad 2.20$$

finally, we can have following equations.

$$\begin{cases} C_{in}V_{in}(\pi R^2) = J_{growth}(\pi R^2) + C_{exhaust}v_{exhaust}(2\pi R H_c) \\ v_{exhaust}(2\pi R H_c) = V_{in}(\pi R^2) \end{cases} \quad 2.21$$

From formula 2.21, we can get mass flux and mass transportation efficiency, which corresponding to growth rate and Ga yield in HVPE process,

$$\begin{cases} J_{growth} = \dfrac{C_{in}v_{in}}{1 + \dfrac{H_c v_{in}}{2D}} \\ Ga_{yield} = \dfrac{1}{1 + \dfrac{H_c v_{in}}{2D}} \end{cases}, d > H_c \quad 2.22$$

$$\begin{cases} J_{growth} = C_{in}\sqrt{\dfrac{D v_{in}}{2H_c}} \\ Ga_{yield} = \sqrt{\dfrac{D}{2H_c v_{in}}} \end{cases}, d < H_c \quad 2.23$$

From above solutions, we can depic the streamline with the streamline equation

$$\frac{\partial r}{\partial z} = \frac{v_r}{v_z} = -\frac{r}{2z} \quad 2.24$$

and the solution is

$$r = r_0\sqrt{\frac{H_c}{z}}, r_0 \in (0, R] \quad 2.25$$

The stagnation point is at $r_0 = 0$, so this singularity must be excluded from the streamline equation 2.25.

To have a more intuitive understand of the calculation, we used the boundary condition of the actual reactor, where $\boldsymbol{H_c} = 4.0$ cm, $\boldsymbol{R} = 25$ mm, $\boldsymbol{C_{in}} = 14\ g/m^3$ and $\boldsymbol{V_{in}} \in [\boldsymbol{0.1}, \boldsymbol{1}]$ m/s. The calculated streamline and growth rate and Ga yield dependence is shown in Figure 2.7 (a) and (b), where all the source gas transported onto wafer surface was assumed to be absorbed by the crystal. Growth rate and Ga yield is a pair of trade-offs depending on input flow velocity. When input concentration is fixed, increasing the input flow will lead to two changes. Firstly, it will lead to higher

source gas flow, hence more source gas will finally reach plate surface. Secondly, it will increase lateral flow speed, higher ratio of source gas will flow away from lateral direction before reaching plate surface. Besides, according to the calculation, the growth rate and Ga yield will both increase with smaller $\boldsymbol{H_c}$. Growth rate increases with increasing input source gas concentration, while Ga yield is independent with input source gas concentration as shown in Figure 2.7 (c) and (d).

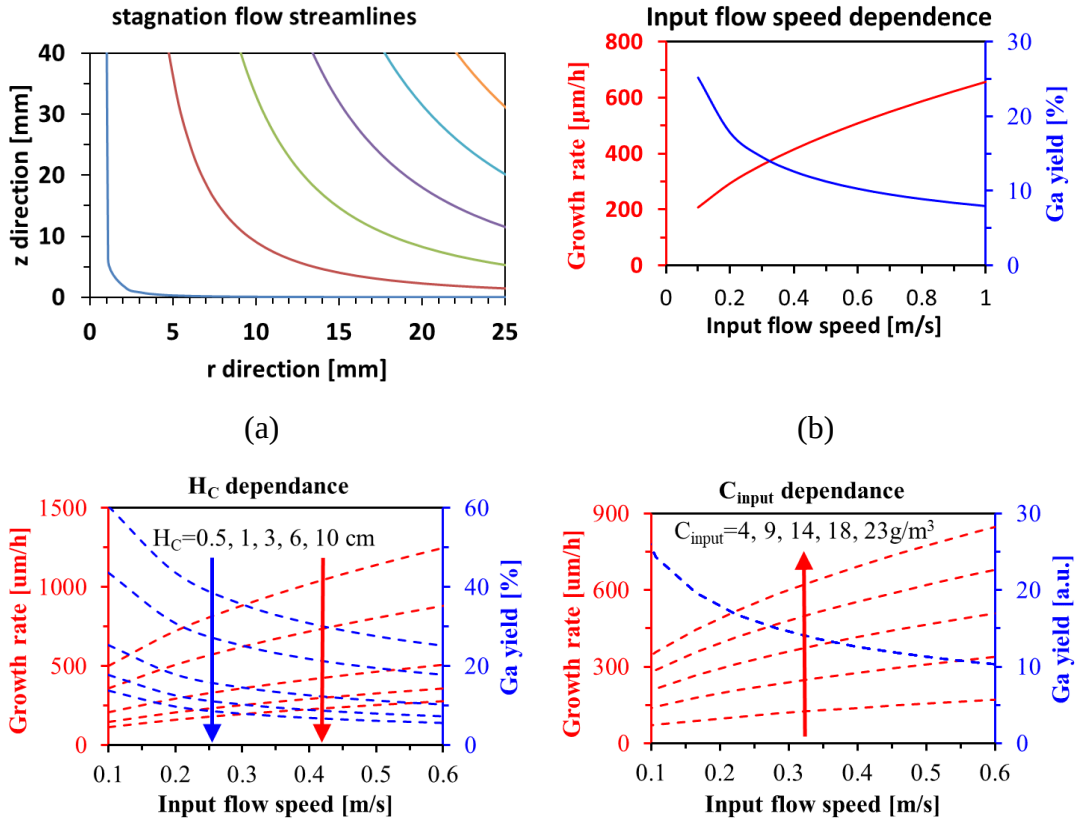

Figure 2.7 Calculation result of (a) streamline, (b) Ga yield and growth rate on input flow speed dependence, (c) constant C_{in}, H_C = 0.5, 1.0, 3.0, 6.0 and 10.0 cm, (d) constant H_C, C_{in} = 4, 9, 14, 18 and 23 g/m3.

For the actual reactor, the source gas was separately input into the growth zone from different nozzles as shown in Figure 2.8 (a). To make sure the source gas was fully mixed before reaching wafer surface, the input flow speed is limited. Besides, the

mixing of source gas is expected to be delayed from nozzles to prevent the strong parasitic deposition on nozzles.

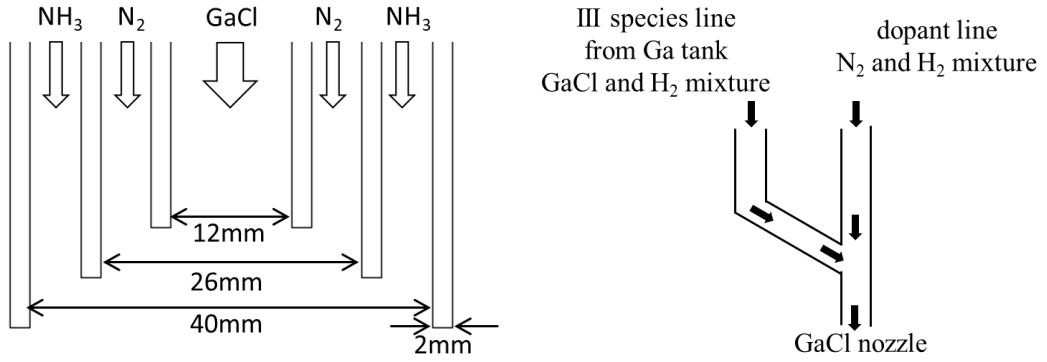

(a) (b)

Figure 2.8 (a) Actual nozzle structure, three concentric cylinder, the dimension of each nozzle is labeled, (b) Gas mixing before GaCl nozzle schematic.

Under this situation, it is hard to estimate the lateral diffusion distance by 1-D advection-diffusion equation because the lateral flow speed is increasing along z direction towards wafer surface according to the calculation. To make sure the flow can mix over 0.1s before reacting to the surface, the total flow is limited to 15 slm in the reactor. Three experiments and corresponding simulation were done to study the flow in the reactor. Their corresponded flow conditions are listed in Table 2.1. The N_2 gas from barrier nozzle is always higher than the gas from GaCl and NH_3 nozzles to make sure the source gas of GaCl and NH_3 can diffuse to the other nozzles across the barrier curtain gas. The flow speed ratio of barrier gas is 1.5 to 2.0 time higher than the source gas based on the flow speed, the ratio is lower with a higher flow speed to make sure the gas has enough time to fully mix before reaching to wafer surface.

To have a higher HCl conversion rate in Ga tank, pure H_2 carrier is used in Ga tank. Because the diffusivity of H_2 is 4 times higher than that of N_2 [2], the H_2 ratio of total flow is expected to keep at a constant value. Although the H_2 ratio in GaCl nozzle was different, the H_2 ratio of total flow was kept constant at 5%. The insufficient H_2 gas was

supplemented by dopant line as shown in Figure 2.8 (b), and the carrier gas in NH_3 nozzle was pure N_2.

Table 2.1 Experiment flow condition list, H_2 gas ratio was kept constant at 5% for all cases to make sure the mixture gas has a similar diffusivity

		Unit	Condition 1	Condition 2	Condition 3
Flow speed	GaCl nozzle	cm/s at 300K	10	15	20
	N_2 nozzle		20	25	30
	NH_3 nozzle		10	15	20
Flow rate GaCl nozzle	GaCl Ga tank	sccm	30	30	30
	N_2 Ga tank		0	0	0
	H_2 Ga tank		65	65	65
	N_2 Dopant line		202	393	633
	H_2 Dopant line		381	530	630
Flow rate N_2 nozzle	N_2		3958	4948	5938
Flow rate NH_3 nozzle	NH_3		3000	3000	3000
	N_2		299	1948	3597
	H_2		0	0	0
Total flow	Gas mixture	slm	8.925	11.903	13.892
H_2 ratio in GaCl nozzle		a.u.	65.76%	58.47%	51.18%
H_2 ratio of total flow		a.u.	5%	5%	5%

Figure 2.9 shows the parasitic deposition result on nozzles with different flow conditions after 6 hours growth and 12 hours growth.

Simulation was also used to study the flow condition in the reactor. And we employed commercially available computational fluid dynamics (CFD) simulator STR Virtual Reactor HVPE edition (HepiGANS). The simulator has the ability to calculate "2-D plane and axisymmetric rotational viscous gas mixture flows inside highly heated modern engineering devices like chemical vapor deposition (CVD) reactors" [5].

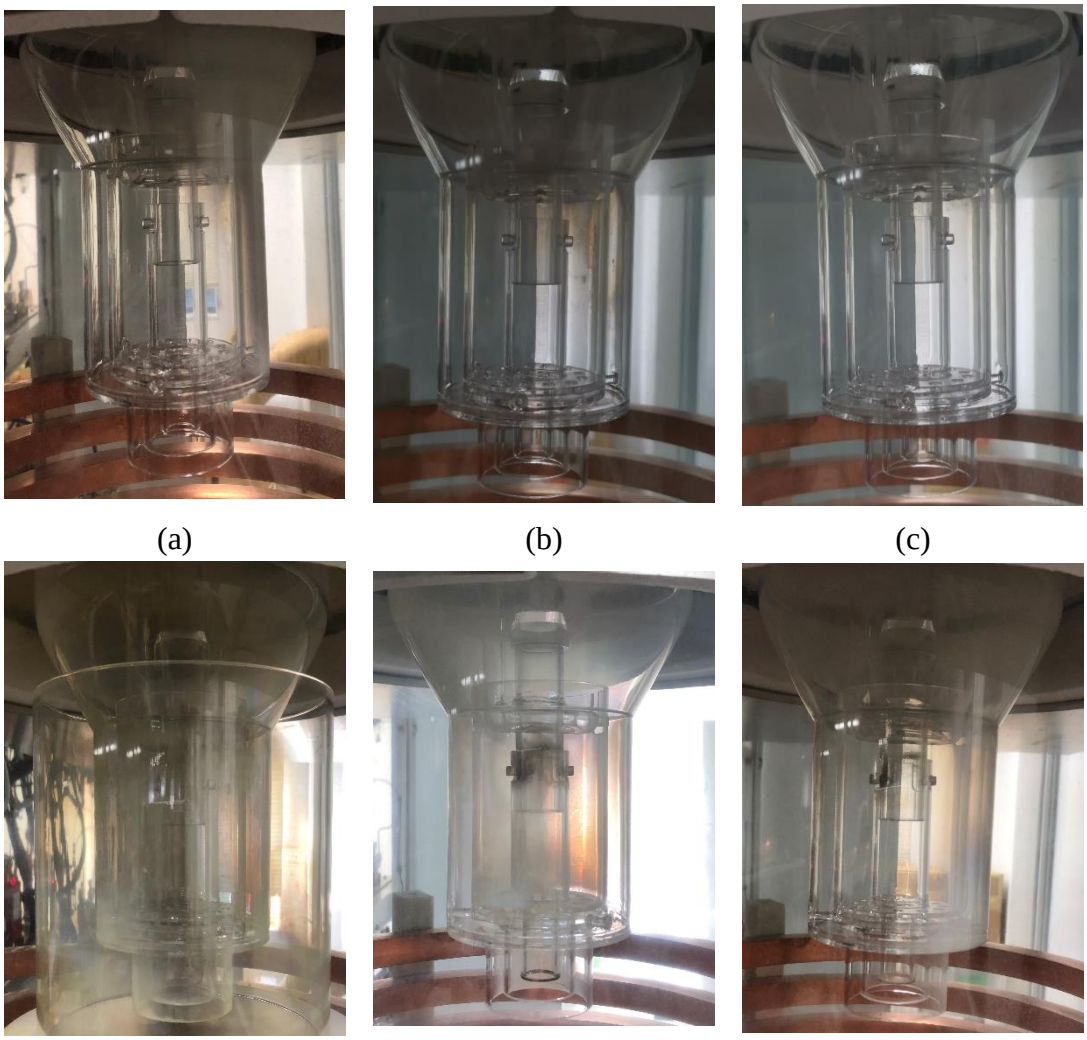

(a) (b) (c)

(d) (e) (f)

Figure 2.9 Nozzle deposition appearance after 6 hours growth with (a) flow condition 1, (b) flow condition 2 and (c) flow condition 3, and after 12 hours growth with (d) flow condition 1, (e) flow condition 2 and (f) flow condition 3.

The physical models are used to describe the gas flow dynamics, heat transfer, and multi-species diffusion in the reactor. There are some preset conditions to simplify the physical model and well customize for the situation in the HVPE reactor for crystal growth.

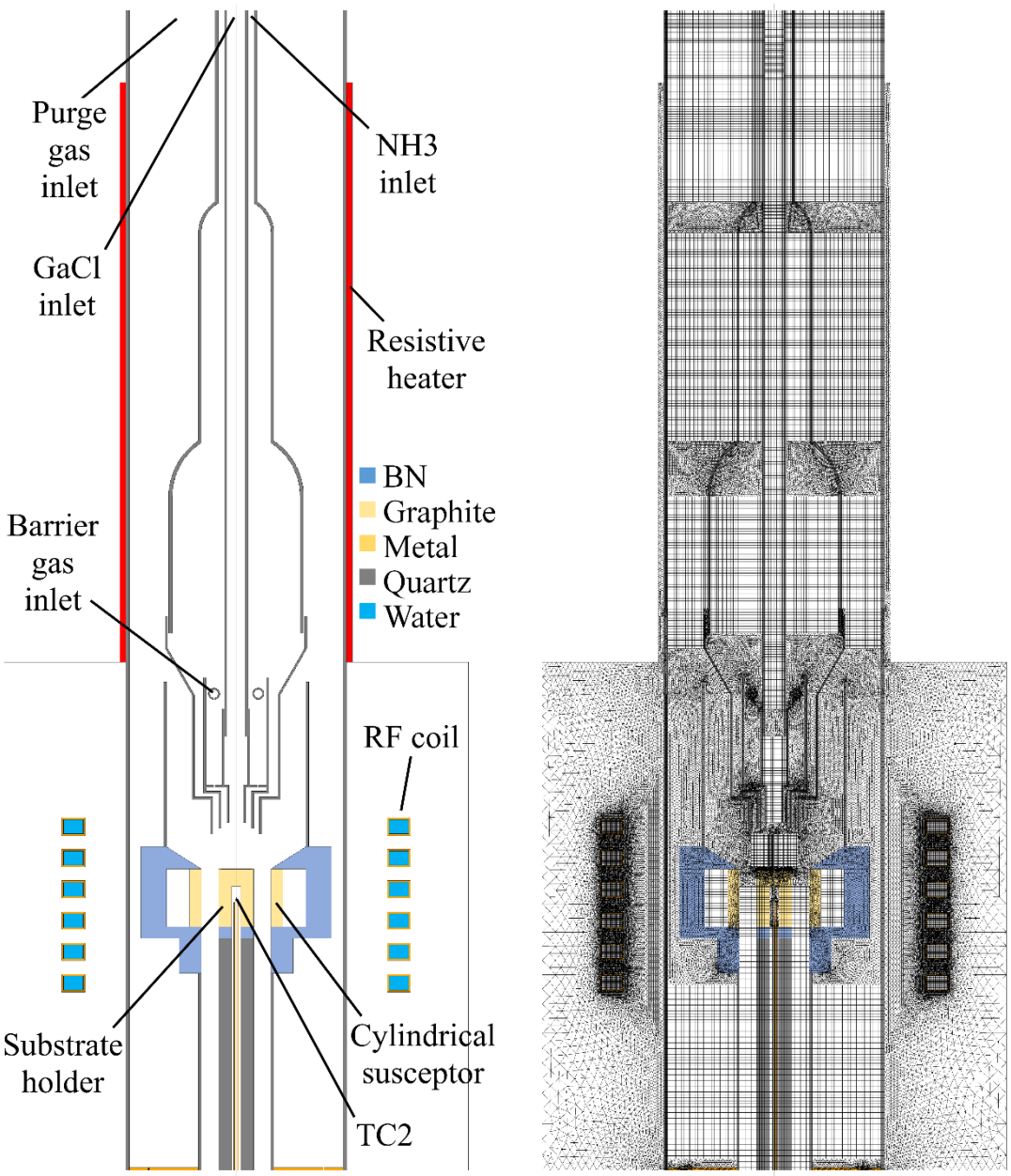

Figure 2.10 (a) Simulation model, (b) Simulation model with mesh grid

The Navier-Stokes equations were employed to describe the fluid dynamics of the gas mixture in the reactor. The gas mixture was treated as ideal gas. And the gas mixture was single phase fluid in which the possible phase conversion and vapor phase reaction during mass transfer were ignored. The involved species in the simulation were all in vapor phase, and crystallization on wafer surface was merely treated as the mass

generation and consumption boundary. The boundary shape changes due to crystal growth on crystal surface was ignored, and the wafer surface was treated as absolute flat surface. The crystallization reaction on wafer surface is exothermic (smaller than 100 kJ/mol), but the reaction quantity (less than 100 μmol/s) was too small, so the heat of chemical reactions was ignored. The growth rate (smaller than 0.15 μm/s) of crystal was negligible compared with the flow speed, hence the flow field can be approximately considered at statistical equilibrium state, and all the time derivatives in the equations were set to zero. The parasitic deposition on reactor walls was neglected for simplification. All the reactor walls were treated as non-chemical surface.

The simulation model is shown in Figure 2.10 (a) and the mesh grid of the model is shown in Figure 2.10 (b). The model is 1:1 ratio to actual reactor. To obtain accurate enough simulation result, the model is cut into 99680 cells and over 7815 boundary faces. The simulator control criterion were convergence and maximum number of iterations. Residual values can directly quantify the error in the solution of the system of equations and is used as convergence criterion. The residual criterion for temperature, chemical species, fluid velocity, growth rate and pressure were 10^{-3}, 10^{-7}, 10^{-5}, 10^{-3} and 10^{-3}, respectively. The maximum number of iterations was 50000. The input flow condition at GaCl inlet, NH_3 inlet, barrier gas inlet and purge gas inlet are the same as the experiment conditions listed in Table 2.1. The temperature of resistive heater (the red color boundary) is set to 800 ºC, and the power of RF coil is fitted to make the temperature at TC2 point to 1050 ºC.

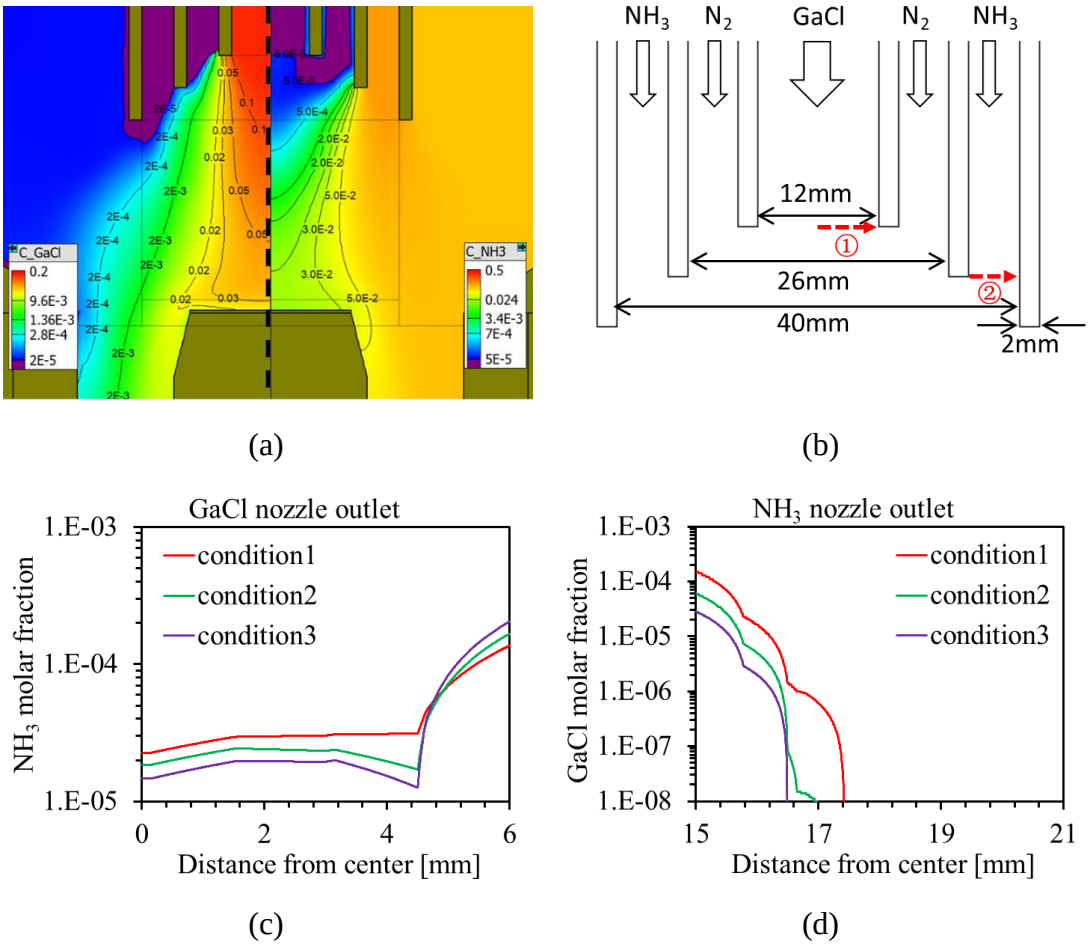

Figure 2.11 (a) Simulation model with GaCl (left half side) and NH_3 (right half side) molar fraction distribution; (c) NH_3 molar fraction along GaCl nozzle outlet (along ①) in (b); (d) GaCl molar fraction along NH_3 nozzle outlet (along ②) in (b).

The molar fraction distribution of GaCl and NH_3 near the growth zone is shown in Figure 2.11 (a), left part (GaCl concentration) and the right part (NH_3 concentration), respectively. From the simulation result (Figure 2.11 (a), (c) and (d)), GaCl and NH_3 diffusion to the other source gas nozzle is at 100 ppm level and can be ignored, but for long growth time like 12 hours, this slight diffusion will also be strong enough to pollute the nozzles.

The growth rate and Ga yield from calculation, simulation and experiment were further compared as shown in Figure 2.12 (a).

The calculation is based on formula 2.22 and 2.23. In the experiment, nozzle size is 40 mm, and wafer is 6.0 cm away from nozzle. The input flow speed is calculated by total flow (as listed in Table 2.1) and nozzle diameter of 40 mm (as shown in Figure 2.11 (b)). The input source gas concentration (GaCl concentration, calculated by GaCl flow and total flow listed in Table 2.1). The parameters used for calculation are listed in Table 2.2. Because the calculation was only based on mass transportation by flow and diffusion without considering the growth at surface, to fit the calculated growth rate with the experiment result, a selected absorption ratio of 0.23 involved, which means 23% of the source gas reached on wafer was absorbed by the crystal. The calculation result is plotted in Figure 2.12 (a) with dash lines.

Table 2.2 Calculation input parameters calculated from experiment condition 1~3.

Input parameters	Unit	Condition 1	Condition 2	Condition 3
H_C	cm	6.0		
R	mm	40		
C_{in}	g/m^3	17.738	12.898	10.133
V_{in}	m/s	0.05 to 0.25		

The growth rate distribution of experiment (with symbol) and simulation (dashed line) is shown in Figure 2.12 (b). The experimental growth rate was measured by SEM cross sectional with accuracy of ±1 μm. The simulation results were fitted with a ratio of 0.51, because in the simulation surface sticking coefficient was 1.0, but in the actual situation it is always smaller than 1.0.

By comparing the calculation, simulation, and experiment growth rate, we can conclude that the different growth rate distribution under these 3 conditions are mainly caused by mass transportation. Both the growth rate and Ga yield of calculation curves have the biggest difference through condition 1 to 3 because the calculation only considered the mass transportation. The simulation results moderate the difference because the simulation involve the chemical reaction at surface, the reaction balance

weaken the effect of mass transportation once, but the simulation model did not consider surface kinetics. For the actual growth, surface kinetics further moderate the difference, so the difference in growth rate of condition 1 to 3 is much smaller than the simulation, as shown in Figure 2.12 (b).

Besides, according to experiment result, the uniformity of condition 3 was not acceptable. This variation is attributed to the high flow speed of flow condition 3. Finally flow condition 2 was selected as the standard flow condition for further experiment.

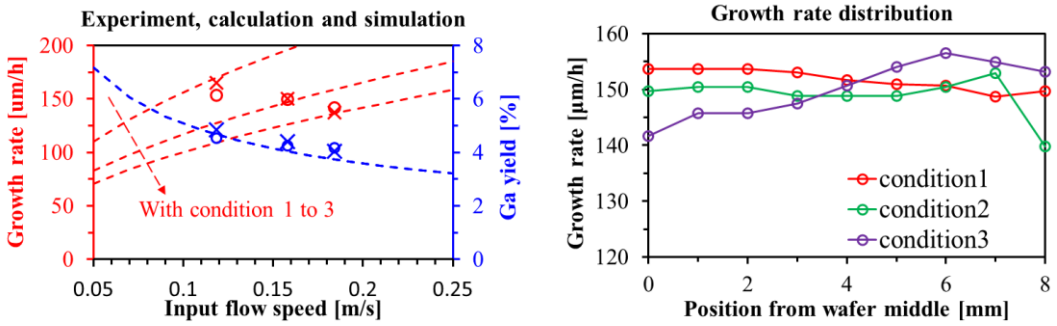

(a) (b)

Figure 2.12 (a) growth rate and Ga yield comparison of experiment result (dot symbol), calculation result (dash lines) and simulation result (cross symbol) with different condition, (b) growth rate distribution of the experiment result with different flow condition

2.4 Growth zone optimization

The growth on wafer surface was also studied by thermodynamic calculation. The main chemical reactions and corresponded equilibrium constants are listed in formula 2.26 to 2.27.

$$GaCl(g) + NH_3(\mathrm{g}) \leftrightarrow \mathrm{GaN(s)} + \mathrm{HCl(g)} + H_2(g) \qquad \mathbf{K_1} = \frac{\mathbf{P_{HCl}P_{H_2}}}{\mathbf{P_{GaCl}P_{NH_3}}} \qquad 2.26$$

$$GaCl(g) + 2\mathrm{HCl(g)} \leftrightarrow \mathrm{Ga}Cl_3(\mathrm{g}) + H_2(g) \qquad \mathbf{K_2} = \frac{\mathbf{P_{GaCl_3}P_{H_2}}}{\mathbf{P_{GaCl}P_{HCl}^2}} \qquad 2.27$$

The pressure in the tank universally equals to 100 kPa, and Ga and N atom are equally absorbed into GaN crystal as shown in formula 2.28, where α denote the NH_3 decomposition ratio during mass transportation (α=0.03 in this calculation, because there is no stainless steel in the reactor and NH_3 decomposition rate is low [6]). The A ratio and F ratio are shown in formula 2.30 and 2.31.

$$\sum \mathbf{P_i} = \mathbf{P_{GaCl}} + \mathbf{P_{GaCl_3}} + \mathbf{P_{HCl}} + \mathbf{P_{NH_3}} + \mathbf{P_{H_2}} + \mathbf{P_{N_2}} \quad 2.28$$

$$\mathbf{P^0_{GaCl}} - \left(\mathbf{P_{GaCl}} + \mathbf{P_{GaCl_3}}\right) = (\mathbf{1} - \boldsymbol{\alpha})\mathbf{P^0_{NH_3}} - \mathbf{P_{NH_3}} \quad 2.29$$

$$\mathbf{A} = \frac{\mathbf{P_{GaCl}} + \mathbf{3P_{GaCl_3}} + \mathbf{P_{HCl}}}{\mathbf{2P_{H_2}} + \mathbf{3P_{NH_3}} + \mathbf{P_{HCl}} + \mathbf{2P_{N_2}}} \quad 2.30$$

$$\mathbf{F} = \frac{\mathbf{2P_{H_2}} + \mathbf{3P_{NH_3}} + \mathbf{P_{HCl}}}{\mathbf{2P_{H_2}} + \mathbf{3P_{NH_3}} + \mathbf{P_{HCl}} + \mathbf{2P_{N_2}}} \quad 2.31$$

By considering formula of 2.25 to 2.30, the partial pressure of 7 species of gases at equilibrium state can be solved. The thermal dynamic data of equilibrium constants for K1 and K2 can also be calculated by formula 2.5, and the thermal dynamic data for calculation are also listed in Appendix I. With the flow condition 2 in Table 2.1, the thermodynamic calculation results with dependence of temperature, input GaCl concentration, F ratio and V/III ratio are shown in Figure 2.13.

The growth rate can be calculated from the decreasing of Ga atoms, and the growth rate dependence was then plotted in Figure 2.14. With flow condition 2 listed in Table 2.1, the H_2 ratio of total flow was kept constant at 5%, so the F ratio was fixed in the calculation. The growth rate decreases with increasing temperature, and increase with higher V/III ratio. With fixed V/III ratio, the growth rate increases linearly with increasing input GaCl concentration. Either increasing input GaCl with constant input NH_3 or increasing input NH_3 with constant input GaCl, the growth rate will increase following different curves.

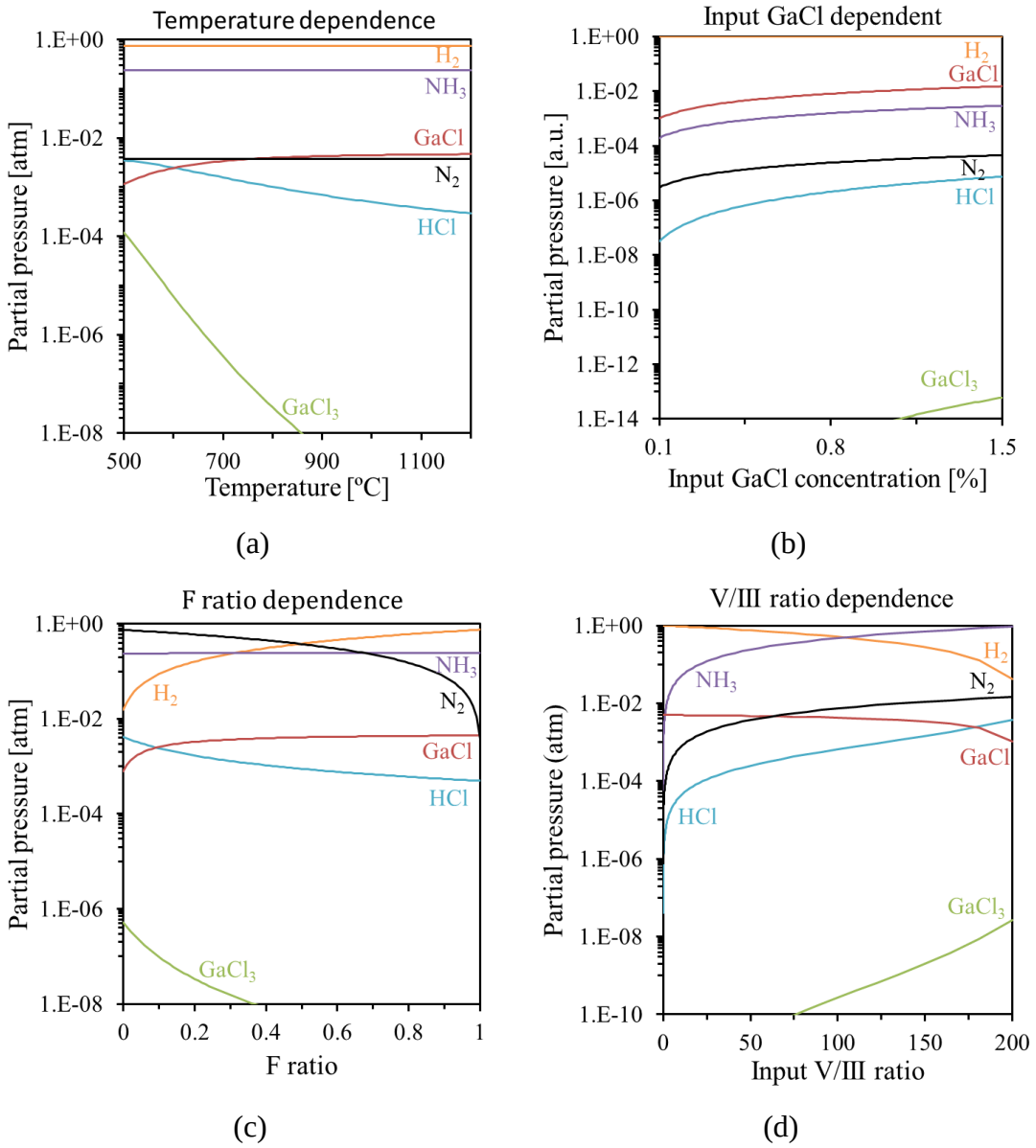

Figure 2.13 Thermal dynamic calculation result, partial pressure of each species on the dependence of (a) temperature, (b) input GaCl concentration, (c) F ratio and (d) V/III ratio.

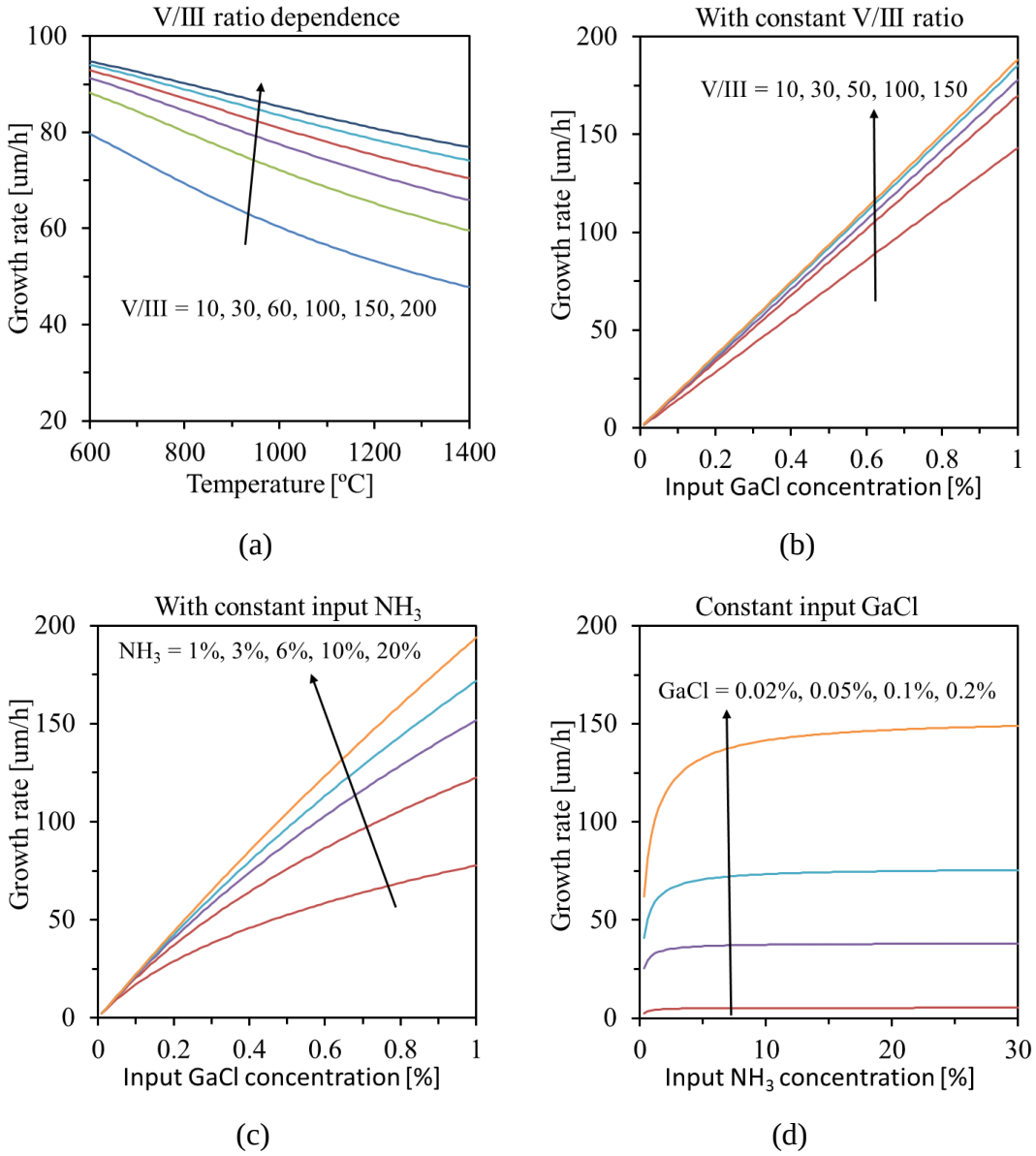

Figure 2.14 Thermal dynamic calculation result, partial pressure of each species on the dependence of (a) temperature, (b) input GaCl concentration, (c) F ratio and (d) V/III ratio.

The experimental growth rate was fitted with the calculation result with different fitting coefficient k as shown in Figure 2.15. Different k can correct the differences introduced by mass transportation, Ga atom absorption rate at crystal interface and other aspects.

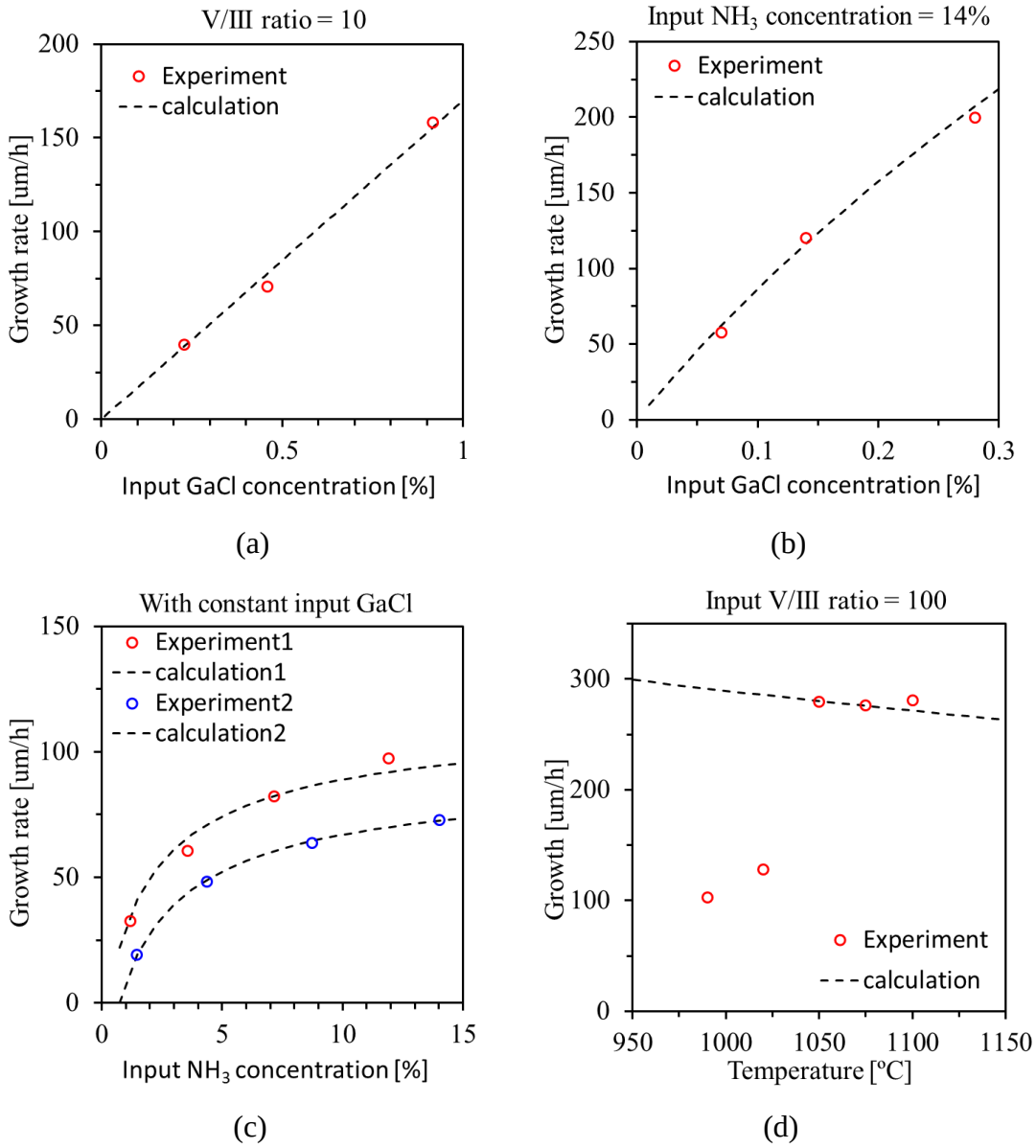

Figure 2.15 Fitting of experimental growth rate with thermal dynamic calculated growth rate, (a) constant input V/III ratio, dependence on input GaCl concentration, k=0.55 (b) constant input NH_3 concentration, dependence on input GaCl concentration, k=0.73 (c) constant input GaCl concentration with different position of 0mm and 20mm, k1=0.75, k2=0.63 and (d) constant input V/III ratio, dependence on growth temperature, k=1.55.

The growth rate dependence on input GaCl, NH_3 and V/III ratio roughly follow the thermal dynamic calculation result, but for temperature lower than 1050 ºC, the surface kinetics control the growth rate, the experimental result deviates from calculation.

2.5 Summary of growth condition optimization

In this chapter, thermal dynamic calculation was applied to help optimize the growth condition at pre-reaction zone and growth zone. The mass transportation of reactant gas through the advection and diffusion of flow was studied by solving a stagnation point flow model in cylindrical coordinates and by simulation study.

In the pre-reaction zone, GaCl conversion rate is the key parameter. A higher GaCl conversion rate will result in a higher Ga yield and a higher growth rate. To obtain a higher GaCl conversion rate, the total flow rate was fixed to 95 sccm to ensure the reactant gas stay long enough time in the Ga tank. The carrier gas is fixed to pure H_2 to improve the GaCl conversion rate. The pre-reaction zone temperature was set to 800 ºC to take a balance point between heating time and GaCl conversion rate.

The mass transportation in the reactor can be simplified to a stagnation point flow model in cylinder coordinates. From the analytical solution of the model, input flow speed (total flow rate), input source concentration and the distance from wafer to nozzle are the variables. Ga yield (the ratio source gas reaching on wafer surface) and growth rate (the amount source gas reaching on wafer surface per unit time) are the key parameters. Firstly, a smaller distance from wafer to nozzle will result in a higher Ga yield and higher growth rate at the same time, but this will trade off the mixing distance. Because the source gas in HVPE reactor usually mixed after inject out from nozzles, so there is always a limitation for the minimum value of this distance. Secondly, by keeping the distance from wafer to nozzle, the growth rate and Ga yield is a pair of trade-offs by changing the input flow speed. Thirdly, by increasing the input source concentration, only the growth rate will increase but the Ga yield will remain.

Another one important factor that needs to be taken care of is the parasitic deposition on the nozzles. In this reactor, the design with three concentric nozzles (see Figure 2.1)

was used, barrier gas flow from the middle nozzle to separate GaCl flow in the middle and the NH_3 flow from outermost. The flow speed ratio among these three nozzles is important. The flow speed of barrier gas is preferred to be always faster than the rest two to ensure the source gas mixing is delayed from the nozzle outlet. Three different flow conditions with different input flow speed ratio (GaCl:barrier:NH_3) of 1:2:1, 1:1.67:1 and 1:1.5:1 and different total flow of 8.925 slm, 11.903 slm and 13.892 slm were studied by experiment, calculation and simulation. To ensure the separation effect the same and to ensure the gas have enough time to mix, for a higher total flow rate, the ratio of barrier is always higher. By considering the parasitic deposition on the nozzles and the epilayer thickness uniformity, flow condition 2 was selected as the optimized flow condition.

In growth zone, the chemical reaction near wafer surface was studied by fitting the thermal dynamic calculation result and the experiment result with a proper fitting coefficient k (which can eliminate the difference due to difference between the calculation model and the experiment). The growth rate dependence on input GaCl concentration with either a constant V/III ratio or a constant input NH_3 concentration. The growth rate dependence on input NH_3 concentration with constant input GaCl concentration, fit well between the calculation and the experiment. For the growth rate dependence on temperature, the experiment result deviate from the calculation below 1050 ºC. This indicates that the growth on the wafer surface below 1050 ºC is rather depend on surface kinetic model rather than thermal dynamic model. To ensure the growth is under source gas-controlled regime with a high growth rate, i.e., in thermal dynamic controlled regime but close to surface kinetic controlled regime, the growth temperature was set to 1050 ºC.

Based on the analysis in this chapter, finally an optimized growth condition is summarized in Table 2.3.

Table 2.3 Optimized growth condition for long time growth

Condition for pre-reaction zone		**Unit**	**Values**
Total flow		sccm	95
HCl flow		sccm	30
H_2 flow		sccm	65
N_2 flow		sccm	0
HCl concentration		%	31.6
Flow residence time		second	40
Ga tank temperature		ºC	800
Condition for flow from nozzle		**Unit**	**Values**
From all nozzles	Total flow	sccm	11903
From GaCl nozzles	Total flow	sccm	1018
	GaCl flow	sccm	30
	N_2 flow	sccm	393
	H_2 flow	sccm	595
From NH3 nozzles	Total flow	sccm	4948
	NH_3 flow	sccm	3000
	N_2 flow	sccm	1948
	H_2 flow	sccm	0
From barrier nozzles	N_2 flow	sccm	4948
	H_2 flow	sccm	0
Average flow speed		cm/s	8.6
From GaCl nozzles		cm/s	15.0
From NH_3 nozzles		cm/s	15.0
From barrier nozzles		cm/s	20.0
Condition for growth zone		Unit	Values
GaCl concentration		%	0.27
NH_3 concentration		%	27.49
H_2 concentration		%	5.45
V/III			100
Growth temperature		ºC	1050
Rotation		rpm	12
Pressure		atm	1.0

2.6 References

[1] *D.K. Jaiswal, A. Kumar, R.R. Yadav, Analytical Solution to the One-Dimensional Advection-Diffusion Equation with Temporally Dependent Coefficients, J. Water Resour. Prot. 03 (2011) 76–84. https://doi.org/10.4236/jwarp.2011.31009.*

[2] P. Kempisty, B. Łucznik, B. Pastuszka, I. Grzegory, M. Boćkowski, S. Krukowski, S. Porowski, CFD and reaction computational analysis of the growth of GaN by HVPE method, J. Cryst. Growth. 296 (2006) 31–42. https://doi.org/10.1016/j.jcrysgro.2006.08.008.

[3] H. Schlichting (Deceased), K. Gersten, Boundary-Layer Theory, Springer, 2016.

[4] A.A. Howling, B. Legradic, M. Chesaux, C. Hollenstein, Plasma deposition in an ideal showerhead reactor: a two-dimensional analytical solution, Plasma Sources Sci. Technol. 21 (2012) 015005. https://doi.org/10.1088/0963-0252/21/1/015005.

[5] A.S. Segal, A.V. Kondratyev, S.Yu. Karpov, D. Martin, V. Wagner, M. Ilegems, Surface chemistry and transport effects in GaN hydride vapor phase epitaxy, J. Cryst. Growth. 270 (2004) 384–395. https://doi.org/10.1016/j.jcrysgro.2004.07.018.

[6] Z. Ye, S. Nitta, K. Nagamatsu, N. Fujimoto, M. Kushimoto, M. Deki, A. Tanaka, Y. Honda, M. Pristovsek, H. Amano, Ammonia decomposition and reaction by high-resolution mass spectrometry for group III–Nitride epitaxial growth, J. Cryst. Growth. 516 (2019) 63–66.

Chapter 3

3 Bulk crystal growth

In this chapter, the technics to achieve bulk GaN crystal growth by HVPE were discussed.

Firstly, the seed for homo-epitaxial crystal growth is important because the crystallinity and dislocation density of the epilayer can be inherent from the seed. And in Section 3.1, homo-epitaxial crystal growth on seeds fabricated by different methods were proceeded and evaluated. The seed was selected due to the evaluation result, and stress in the epilayer was analyzed by calculation based on the evaluation result.

Secondly, the stress which determines the thickness limitation of the epilayer is strongly influenced by the various edge effects ranging from spurious growth on the edges or formation of facets. In Section 3.2.2, protection rings made of different material were experimentally compared and the ring has the best performance for long time growth was selected based on the experiment result.

Thirdly, pocket is not preferred in bulk crystal growth because the epilayer thickness is much larger than the pocket depth, so seed fixation becomes important. Besides, the growth time is usually very long for bulk crystal growth, so the backside protection is also important. In Section 3.2.3, cement and protection methods which are commonly used in sublimation were experimentally compared, and the fixation method was finally selected based on the experimental result.

Finally, long time growth experiment was proceeded and described in Section 3.2.4, and to extend the thickness limitation, regrowth was described in Section 3.2.5.

3.1 Seed selection

To achieve best bulk GaN crystal, the seed for homo-epitaxial crystal growth is important because the crystallinity and dislocation density of the epilayer can be inherent from the seed. Besides, the initial lattice bow of the wafer is also important because it not only influences the thickness limitation, but also influence the epilayer uniform growth and doping across the entire wafer, which is paramount for achieving high reliability and high yield. Therefore, a tight control of the surface offcut is required for all device layers, usually within 0.1° [1], which translates to a lattice curvature greater than 30 m for a 2 inch wafer [2].

3.1.1 Samples

Commercially available 2-inch ammonothermal, HVPE (HVPE1 and HVPE2 from two different company) and Na-flux GaN (0001) wafers were chosen for this study to cover a range of initial dislocation densities, lattice bows, and doping conditions. All wafers were n-type and the pertinent wafer parameters are listed in Table 3.1 Various initial GaN wafer parameters; all wafers were 2 inch in diameter. All growth studies were performed on squares diced from the commercial 2-inch wafers.

Table 3.1 Various initial GaN wafer parameters; all wafers were 2 inch in diameter

Sample	Electron density [cm^{-3}]	RMS roughness [nm]	Offcut/ direction [deg]	Thickness [μm]	Dislocation density [cm^{-2}]
Ammono-thermal	$< 10^{19}$	< 0.5	0.3/[1$\bar{1}$00]	500	$< 5\times10^{4}$
HVPE1	$\sim10^{19}$	< 0.35	0.3/[1$\bar{1}$00]	356	7.9×10^{5}
HVPE2	1.3×10^{18}	< 0.35	0.5/[11$\bar{2}$0]	415	4.6×10^{6}
Na-flux	$< 10^{17}$	< 0.5	0.1/[1$\bar{1}$00]	399	$< 5\times10^{4}$

All the seeds were placed in the same susceptor pocket with same orientation during the growth procedure to make sure they were all prepared at same growth condition. Their placement position, as well as the dimensions label, is shown in Figure 3.1.

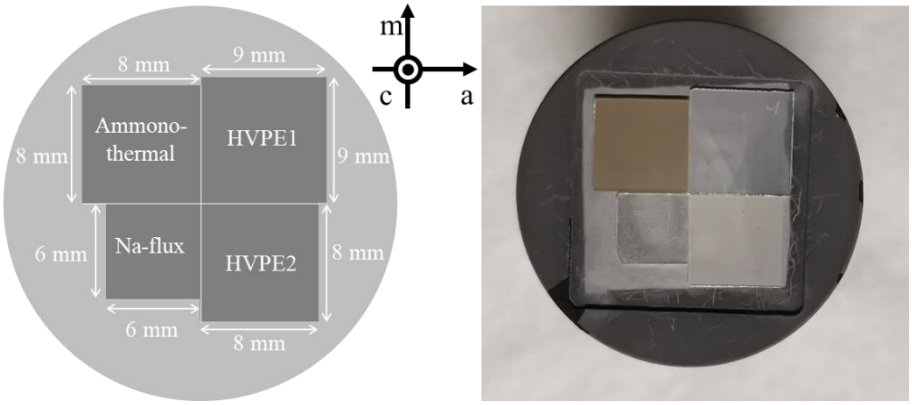

Figure 3.1 Sample placement position, orientation, and dimension

3.1.2 Growth procedure

The epilayers were prepared by our homemade HVPE reactor. The growth zone temperature was 1050 ºC and pre-reaction zone temperature was 750 ºC. The input V/III ratio was 30 with HCl flow rate of 13 sccm and NH_3 flow rate of 390 sccm. With these parameters, the growth was at III-species limited regime, and the growth rate was proportional to III-species input flow rate. Flow condition 1 in Table 2.1 was used in this experiment because the growth time is not long, and flow condition 1 may lead to a better uniformity.

Prior to growth, both the source and growth zones were preheated in the nitrogen atmosphere to 500 ºC. At this point, ammonia flow was initiated and heating to the final temperatures of the two zones continued at 12.5 ºC/min and 25 ºC/min, respectively. When the desired temperatures were reached, hydrogen and HCl flows were initiated and the crystallization process began. After a thickness of 40 μm was reached, the flow to the Ga source was switched off and the growth zone was cooled down at 20ºC/min in ammonia atmosphere until a temperature of 400 ºC was reached. The flow chart is shown in Figure 3.2.

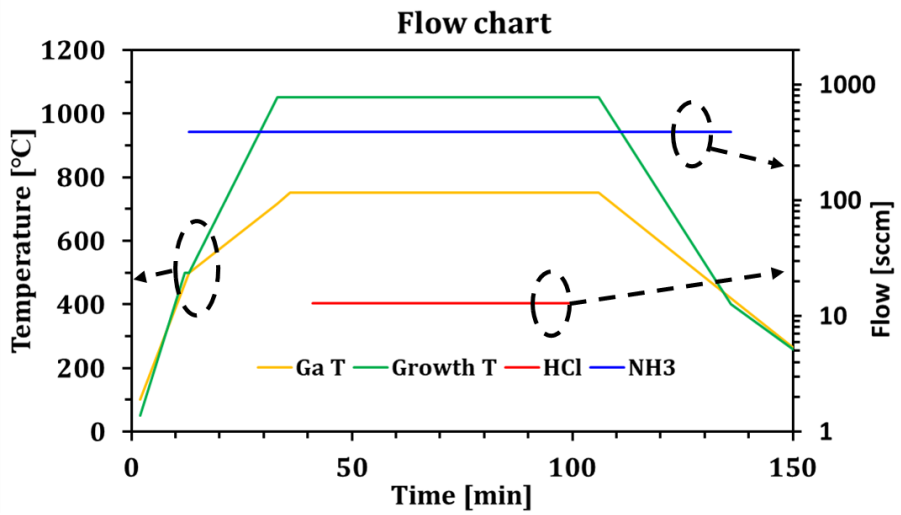

Figure 3.2 Flow chart of the experiment

3.1.3 Evaluation and result

The macroscopic photographs of as-grown samples and differential interference contrast (DIC) micrographs of the morphology are shown in Figure 3.3 (a) and (b), respectively. All the samples are placed with the same orientation. On as-grown seeds surface, sub millimeter level hexagonal hillocks and macro-steps were observed on surface of epilayer on ammonothermal, Na flux and HVPE seeds. However, the hillock size, density and macro-step orientation are different on different samples. The hillock edge is parallel to a-axis, and the macro-step shows a trace of successive m- and a-oriented steps. Hexagonal hillocks representing growth centers [3] and macro-steps, indicative of a low surface supersaturation process [4] dominated the growth surface.

X-ray diffraction (XRD) measurements were carried out prior and after the growth using a Philips X'Pert Pro materials research diffractometer employing a Cu anode and a four-crystal monochromator in Ge×220 configuration. This diffractometer equipped a Eulerian-cradle and a xyz-stage for sample mount. Rocking curves of the symmetric (0002) and asymmetric ($10\bar{1}2$) reflections were recorded in a double-axis configuration with a four-bounce Ge (220) symmetrical monochromator to evaluate the tilt and twist, respectively.

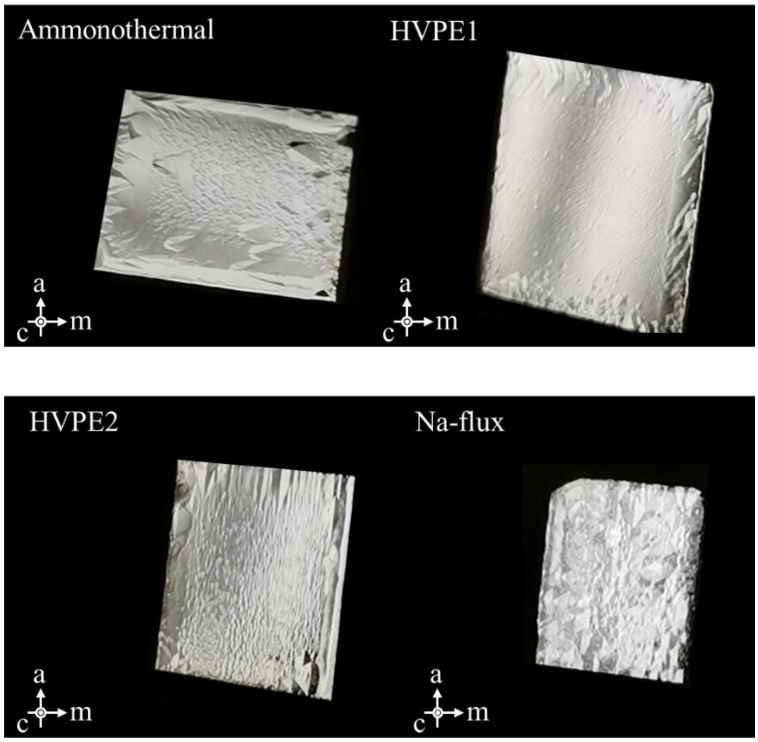

(a)

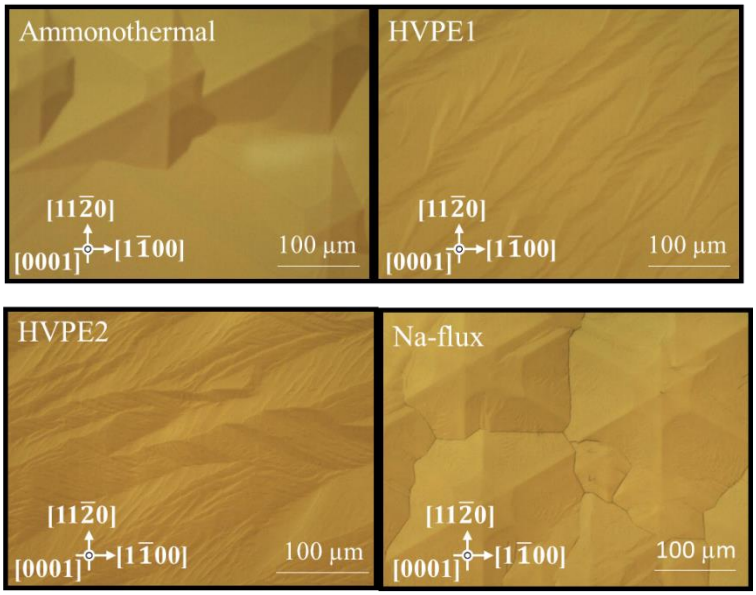

(b)

Figure 3.3 (a) As-grown sample photos, (b) DIC optical micrographs of as-grown GaN samples

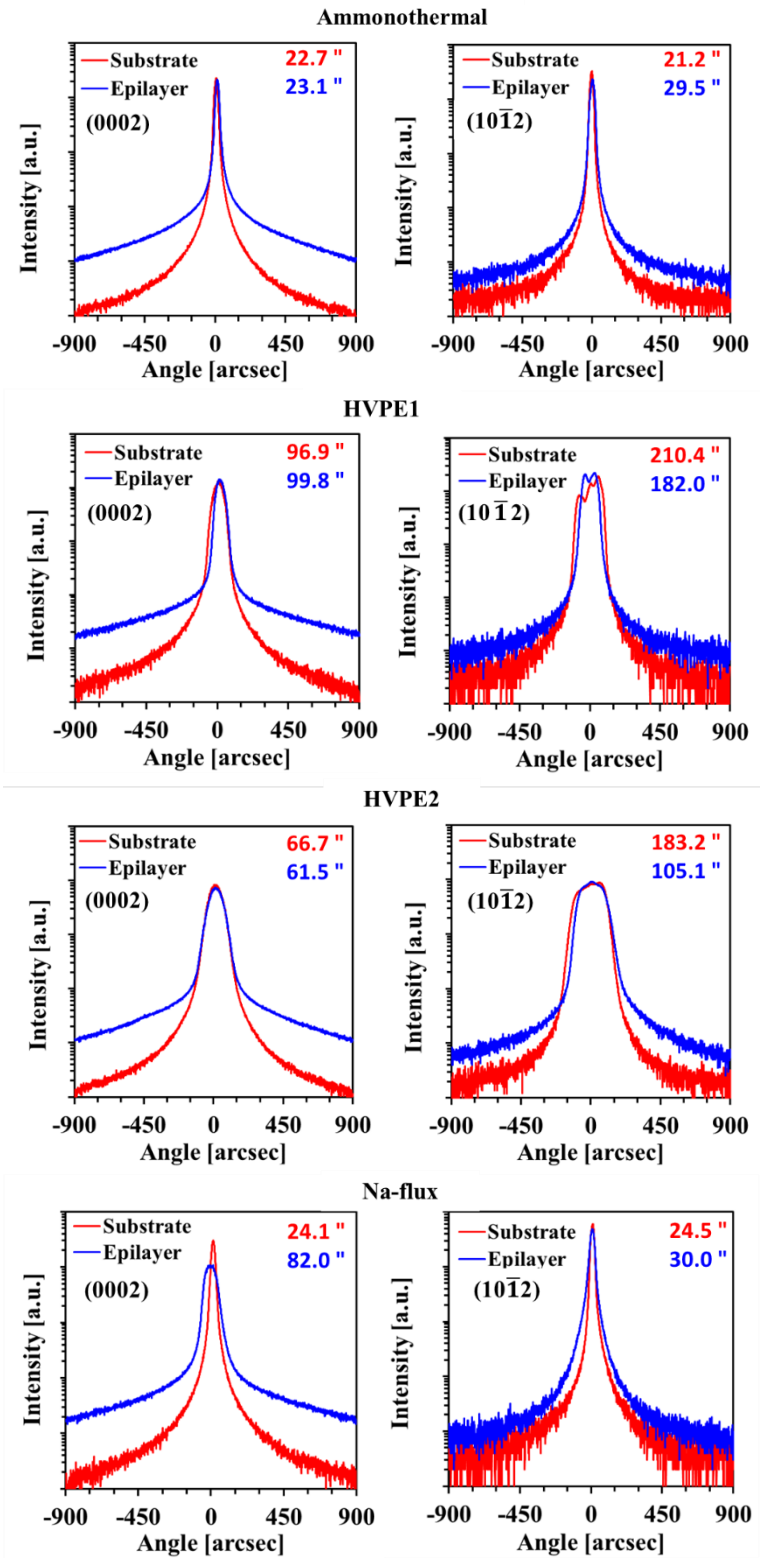

Figure 3.4 Logarithmic plots of (0002) and (10$\bar{1}$2) XRCs, evaluating the tilt and twist, respectively, before and after the growth.

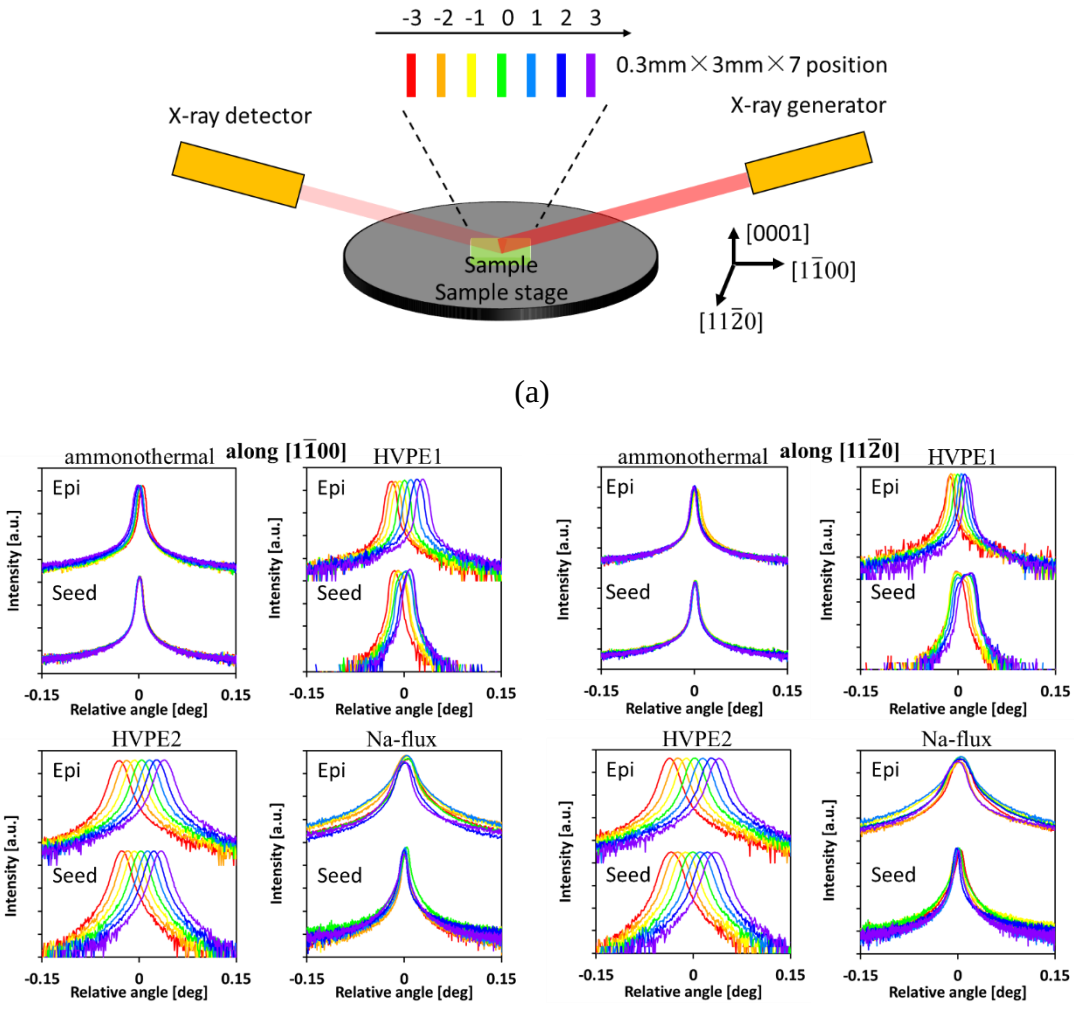

Figure 3.5 (a) Curvature measurement setup, the sample is along [1$\bar{1}$00] direction, to measure along [11$\bar{2}$0] direction, the sample stage need to rotate 90°; (0002) peak shift along (b) [1$\bar{1}$00] direction and (c) [11$\bar{2}$0] direction.

The (0002) and (10$\bar{1}$2) X-ray rocking curves (XRCs) of the samples before and after the growth are shown in Figure 3.4. The full width of half maximum (FWHM) values of the peaks are listed in the upper right corners of the figures. Generally, Ammonothermal sample showed narrower peaks, indicative of high crystalline quality, while HVPE1 and HVPE2 sample exhibited values typical for commercial free-standing HVPE wafers. Special case appeared in Na-flux epilayer, the XRC of (0002) peak widened, even the XRC shape has changed. The twist values for HVPE1 and HVPE2 sample showed a measurable improvement after the growth.

Lattice bow, measured as the radius of curvature, R_C, was evaluated using seven (0002) rocking curves taken along the orthogonal [1$\bar{1}$00] and [11$\bar{2}$0] directions at an interval of 1 mm, similar to the method described in Ref. [5]. Along each direction, 7 X-ray rocking curves from (0002) plane were collected on the sample in a line with distance of 1 mm, the spot size was 0.3 mm × 3 mm with the longer dimension perpendicular to the diffraction plane, as shown in Figure 3.5 (a).

Figure 3.5 (b) and (c) show the XRC peak shifting of (0002) plane measuring along [1$\bar{1}$00] and [11$\bar{2}$0] direction, respectively. Bottom curve series of each figure are the measurement results of seed, and top curve series of each figure are the measurement results of epi-layer. The color in each series of curve is corresponded to the different measurement positions in Figure 3.5 (a).

Table 3.2 Radii of curvature measured along two orthogonal directions before and after the growth. Note: "-" designates convex bow

Direction	**Ammonothermal [m]**		**HVPE1 [m]**		**HVPE2 [m]**		**Na-flux [m]**	
	substrate	epilayer	substrate	epilayer	substrate	epilayer	substrate	epilayer
[1$\bar{1}$00]	-677.3	-49.1	13.4	10.0	5.0	4.0	-56.4	-50.5
[11$\bar{2}$0]	-245.7	-72.3	14.0	11.8	5.0	4.5	-76.6	-82.3

Table 3.2 lists the measured lattice bow as radius of curvature, R_C, in two orthogonal directions ([1$\bar{1}$00] and [11$\bar{2}$0]) for all samples before (substrate) and after (epilayer) the growth. It is important to point out that the sample before growth is not the same ample with the sample after growth, but they are cut from the same 2-inch wafer from adjacent area, so their lattice bow and other property can be considered as the same. The R_C values for the ammonothermally-grown substrate were generally several hundred meters in either direction, while those of the HVPE-derived wafers were in the low teens (HVPE1 sample) or even single digits (HVPE2 sample), which is typical for commercial HVPE wafers and commensurate with the specified dislocation density (see Table 3.1). The R_C values for Na-flux grown substrate was several tens meters in

either direction. Following the growth, all radii of curvature further decreased, indicating an accumulation of additional stress in the epilayers.

The lattice constant of each sample before (substrate) and after (epilayer) growth are shown in Table 3.3. The lattice constant is calculated from the 2theta scan peak position value of (0006) plane and $(1\bar{1}03)$ plane. The accuracy of the lattice constant is ±0.0002 Å in c and ±0.0002 Å in a. Lattice constant c varies in the fourth digit (0.0001 Å), while lattice constant a varies in the third digit (0.001 Å).

Table 3.3 Lattice constant calculated from (0006) scan and $(1\bar{1}03)$ scan

Direction	Ammonothermal [Å]		HVPE1 [Å]		HVPE2 [Å]		Na-flux [Å]	
	substrate	epilayer	substrate	epilayer	substrate	epilayer	substrate	epilayer
a	3.18899	3.18895	3.18867	3.18890	3.18874	3.18896	3.18890	3.18890
c	5.18535	5.18536	5.18536	5.18536	5.18536	5.18533	5.18540	5.18530

To make the lattice constant change clearer, the lattice constant was plotted in Figure 3.6. Before growth, lattice constant a of HVPE1 and HVPE2 sample are smaller than ammonothermal and Na-flux sample, but the lattice constant crowded together for the epilayers on all the samples.

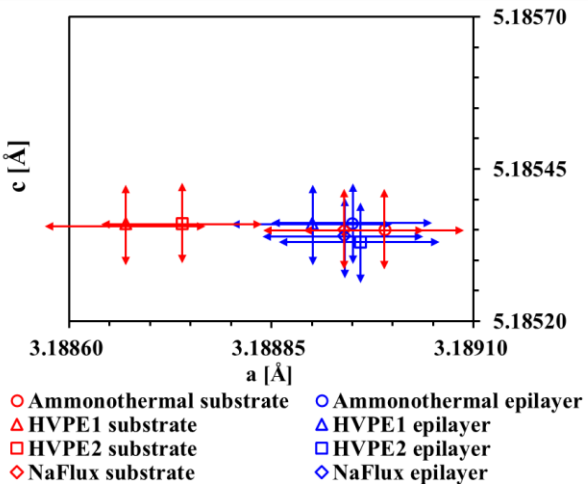

Figure 3.6 Lattice constant plot with error bar of ±0.0002 Å in c and ±0.0004 Å in c

The dislocations in the substrates and epilayers were analyzed using two-photon excitation photoluminescence (2PPL) [6]. The method allowed for a direct visualization of dislocations as a function of the depth in the sample. The dislocation inclination angle, α, in the epi-layers was calculated from the 3D dislocation model built from 50 × 50 μm^2 2PPL slices taken at 1 μm depth intervals. The direction of the inclination and the inclination angle were calculated from the x-y coordinate change in the images taken 2 and 12 μm above the substrate–epilayer interface.

Figure 3.7 shows a 3D view of dislocations in a volume 20 μm below to 20 μm above the homoepitaxial interface along with 2D slices taken 2 μm below (substrate) and 5 μm above (epilayer) the interface. A perusal of these images reveals several observations: (1) most dislocations propagate from the substrate into the epilayer, (2) many dislocations incline at the interface, and (3) new dislocations or even dislocation bundles form at the homoepitaxial interface. Dislocation bundles were observed on both HVPE-derived wafers and Na-flux derived wafers, and are likely a consequence of some surface residue from the polishing process. The dislocation bundles will increase the dislocation density in the epilayer and worsen the crystal quality, and they are preferred to be eliminated by proper surface treatment before growth.

The dark spot of each seed and the epilayer on them are all listed in Table 3.4. For HVPE samples and ammonothermal sample, dark spot of epilayer and seed have the same order of magnitude. Dark spot of epilayer on ammonothermal is slightly lower than dark spot in ammonothermal seed. Dark spot of HVPE epilayer is slightly higher than dark spot in HVPE seed. But for Na-flux sample, the dark spot in epilayer is much higher than seed due to high density of dislocation bundles generated at interface.

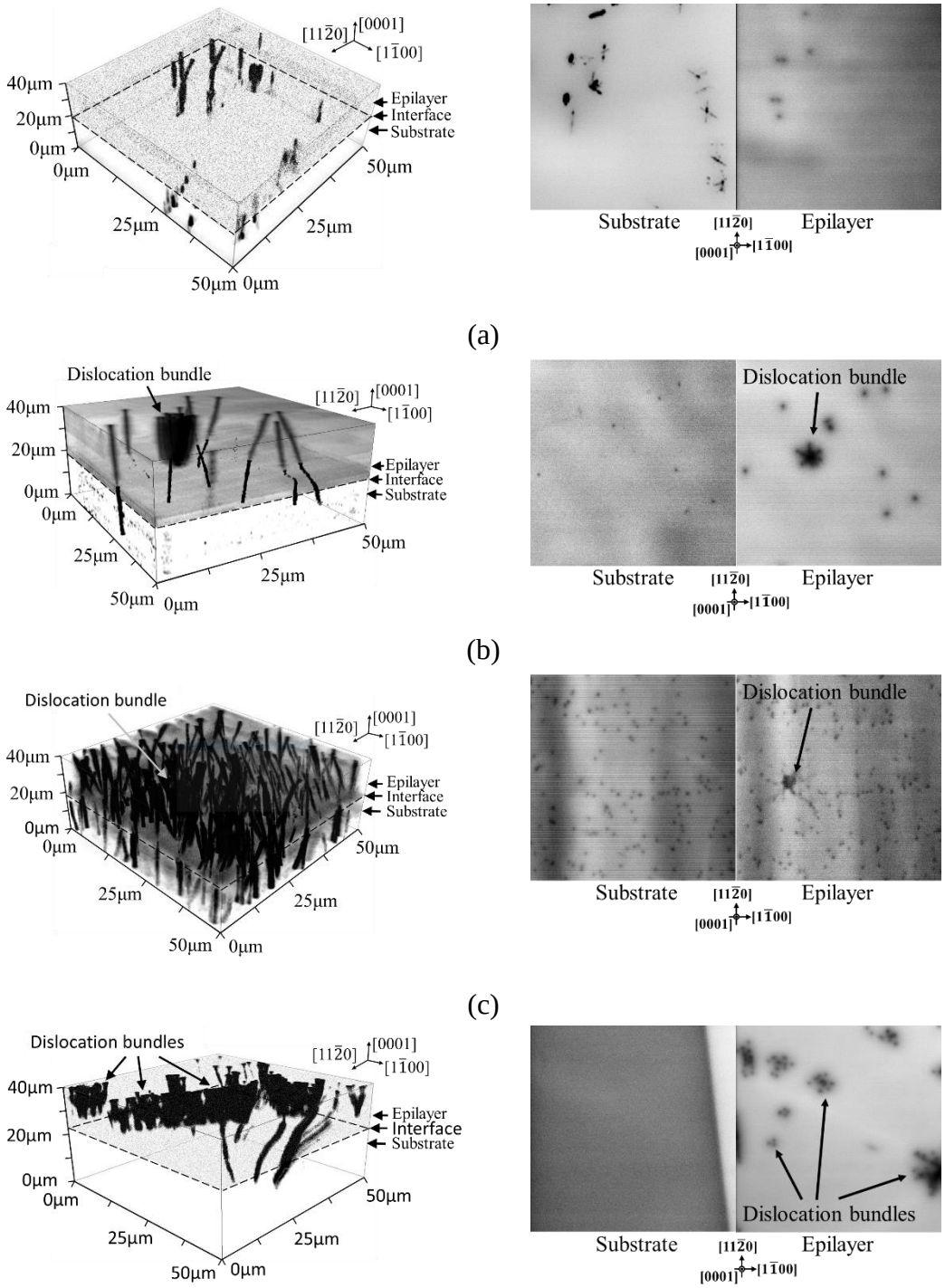

Figure 3.7 (left) 3D visualization of dislocation propagation through the interface; (right) 2D 2PPL images from the substrates and epilayers for (a) ammonothermal sample, (b) HVPE 1 sample, (c) HVPE 2 sample and (d) Na-flux sample.

Table 3.4 Dark spot density as measured by 2PPL

	Ammonothermal [cm^{-2}]	HVPE1 [cm^{-2}]	HVPE2 [cm^{-2}]	Na-flux [cm^{-2}]
Seed	4.80×10^{4}	3.60×10^{5}	5.36×10^{6}	0
Epilayer	2.88×10^{4}	1.12×10^{6}	3.56×10^{6}	4.2×10^{6}

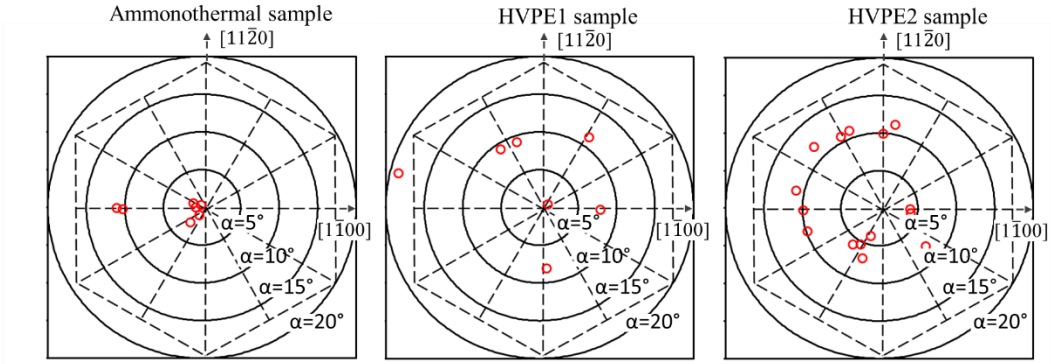

Figure 3.8 Polar plots of dislocation inclination for the 3 samples. Each circle represents 5°; dashed hexagon illustrates the crystallographic directions

The calculated values of the inclination angle, α, and direction of inclination are plotted in Figure 3.8. All individual dislocations visible in the 50x50 μm^2 were included for ammonothermal samples and HVPE1 sample, while for HVPE2 sample, which has a much higher dislocation density, 25 dislocations were chosen at random for this analysis. Most dislocations in the GaN epilayer in ammonothermal propagated more or less perpendicular to the epilayer interface, as indicated by the cluster of measurement points in the center of Figure 3.8, while a few were inclined about 10° from the c-direction. The α values measured in HVPE1 and HVPE2 sample were mostly around 10°, although inclination as high as 20° was observed. Interestingly, the inclination direction seemed to be random, as can be seen in Figure 3.8. There is report about V-shape dislocation generation at the interface of MOVPE-grown GaN on ammonothermal substrate [7], lack of dislocations and difference in the lattice constant between the substrate and the epitaxial layer are considered to be a cause of generation of V-shape dislocation. The lattice constant between the epilayer (a=3.18895 Å) and the substrate (a=3.18899 Å) are very close, hence the directional dependence of inclination, the result from ammonothermal sample may be statistically irrelevant.

3.1.4 Discussion

In Figure 3.4, except for Na-flux sample, the tilt values for the substrates and epilayers were similar in all cases (similar FWHM of the symmetric reflection), but epilayers exhibited in the symmetric reflections a higher peak-tail intensity. This was attributed to the broadening of the specular reflection intensity due to slight lattice undulations caused by inhomogeneous, growth-related stress [8]. Besides, this phenomenon was also analyzed using a method proposed by Kaganer in Ref. [9]. For simplify the explanation, we plotted the XRC of (0002) of Sample C in log-log scale as an example, as shown in Figure 3.9.

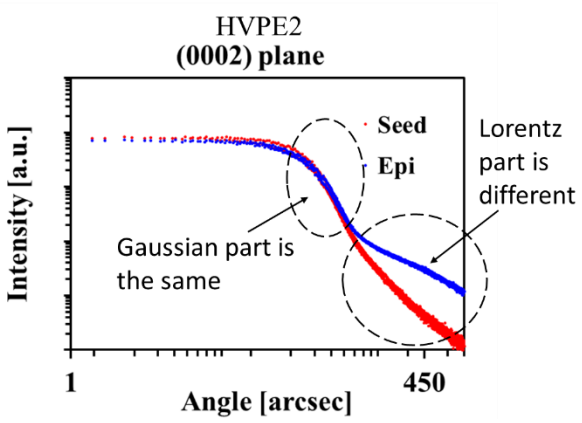

Figure 3.9 (0002) plane XRC of HVPE2 sample in log-log plot, the Gaussian part and the Lorentz part can be distinguished with this method.

The XRD line broadening are mainly from four aspects: instrument, crystallite size, strain, and dislocations. Aside from broadening from instrument, size effect is related with Lorentz part, and strain effect is related with Gaussian part. The dislocation effect related with both as shown in Ref. [9]. We used the same instrument, and the dislocation density of the epilayer and substrate are in the same order. From Figure 3.10, the Lorentz part for (0002) plot is always bigger for the epilayer than the substrate. But for $(10\bar{1}2)$ plane, the tail is more complex, the Lorentz part can be same (ammonothermal sample), smaller (HVPE1 sample) or bigger (HVPE2 sample) for the epilayer than substrate. Although the as-grown morphology is too big to interact with X-ray, but it

distorts the measurement area and enhanced the Lorentz part of (0002) XRCs. The incident angle is much bigger for $(10\bar{1}2)$ plane than (0002) plane, so $(10\bar{1}2)$ plane is less influenced by the different measurement area caused by surface morphology.

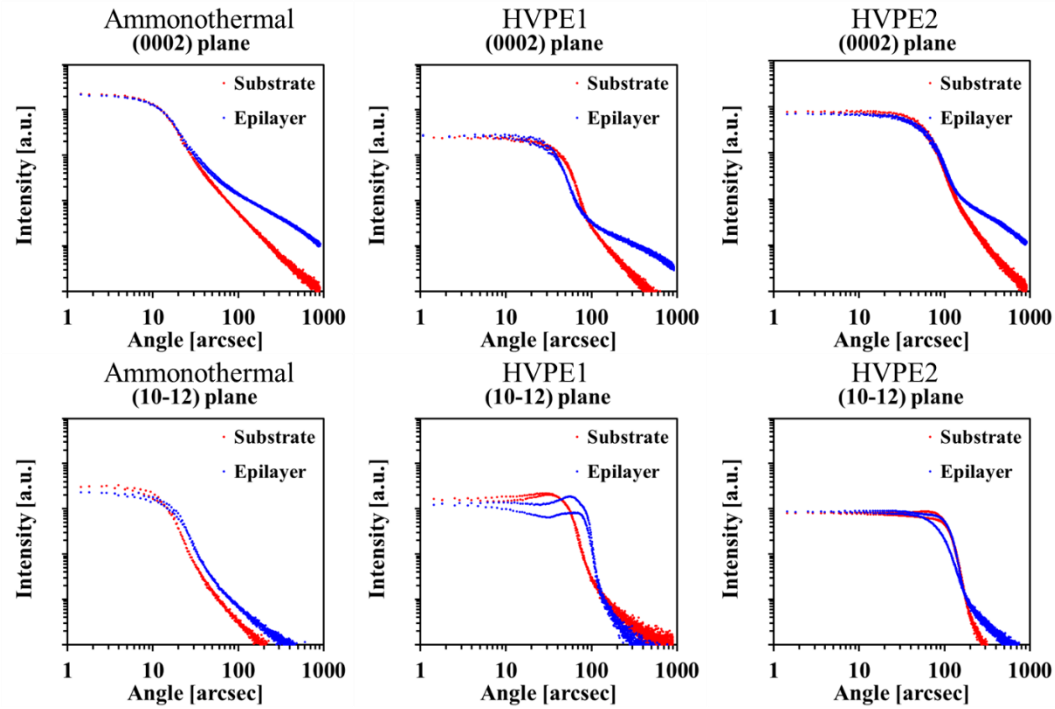

Figure 3.10 (0002) and $(10\bar{1}2)$ plane XRCs of ammonothermal, HVPE1 and HVPE2 sample in log-log plot.

As shown in Figure 3.11 (a), if a film with thickness of t_f is deposited on a substrate with thickness of t_s, when the film is under stress of σ_f, and the radius of curvature is R. Then based on Stoney equation [10], they have relationship of

$$\sigma = \left(\frac{E_s}{1-\upsilon_s}\right)\varepsilon = \frac{1}{6}\left(C_{11}+C_{12}-\frac{2C_{13}^2}{C_{33}}\right)\left(\frac{{t_s}^2}{t_f}\right)\left(\frac{1}{R_s}-\frac{1}{R_f}\right) \qquad 3.1$$

where σ is the stress, ε is the strain, C_{11}, C_{12}, C_{13} and C_{33} are the hexagonal stiffness constants of GaN, t_s is the substrate thickness, t_f is the film thickness, R_s is the substrate radii and R_f is the film radii.

The strain and stress in of ammonothermal sample, HVPE1 and HVPE2 sample can be calculated as shown in Table 3.5, where the stiffness constants $C_{11} = 353.93$ GPa, $C_{12} = 82.59$ GPa, $C_{13} = 94.46$ GPa and $C_{33} = 380.44$ GPa.

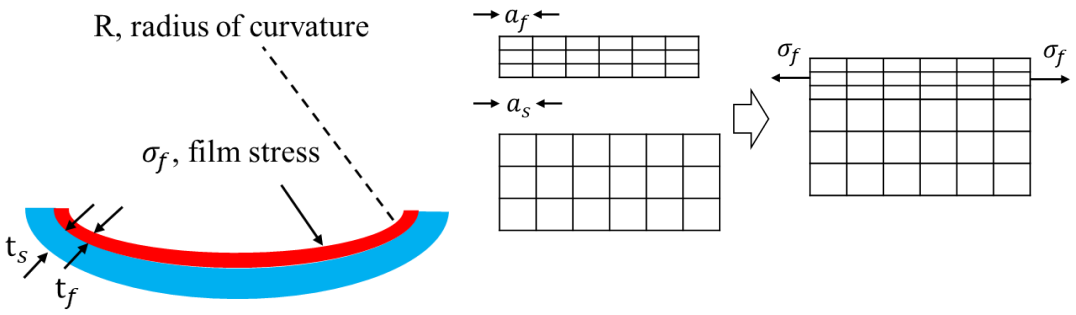

(a) (b)

Figure 3.11 (a) Thin film deposit on a substrate, (b) lattice mismatch between film and substrate

Although the change in the curvature of the ammonothermal sample appeared to be the largest, the additional stress induced by the epilayer was small as compared to the stress in the epilayers in HVPE1 and HVPE2 sample.

Table 3.5 Calculated total strain and stress by Stoney equation

Sample		Ammonothermal		HVPE1		HVPE2	
Item	**Unit**	along $[1\bar{1}00]$	along $[11\bar{2}0]$	along $[1\bar{1}00]$	along $[11\bar{2}0]$	along $[1\bar{1}00]$	along $[11\bar{2}0]$
$\boldsymbol{t_s}$	um	500	500	356	356	415	415
$\boldsymbol{t_f}$	um	40	40	40	40	40	40
$\boldsymbol{R_s}$	m	-677	-246	13	14	5	5
$\boldsymbol{R_f}$	m	-50	-72	10	12	4	4
$\boldsymbol{\varepsilon}$	a.u.	-1.9E-05	-1.0E-05	1.2E-05	6.3E-06	3.6E-05	3.6E-05
$\boldsymbol{\sigma}$	GPa	-7.5E-03	-4.0E-03	4.7E-03	2.4E-03	1.4E-02	1.4E-02
	MPa	-7.52	-3.99	4.75	2.45	13.98	13.98

In general, wafer bow in homoepitaxy can be influenced by: (1) slight lattice mismatch between the substrate and overgrowth due to different point defect densities (for example, void defect will reduce the lattice mismatch), (2) change in dislocation density and the associated strain energy due to dislocation inclination or generation of new dislocations, or (3) various edge effects ranging from spurious growth on the edges or formation of facets. For the first two cases, simple models exist to evaluate additional

stress and associated bow while the last case is related to some challenge in controlling the growth process and requires a system-specific solution.

The total stain can be calculated from the sum of the strain sources discussed above by formula 3.2,

$$\varepsilon = \varepsilon_1 + \varepsilon_2 + \varepsilon_3 \qquad 3.2$$

where ε_1 to ε_3 are corresponded to source (1) to (3).

For source (1), to evaluate the contribution of the slight lattice parameter difference between the different substrates and overgrowth, i.e., the model shown in Figure 3.11 (b), the lattice constant for substrate is a_s, and for the film is a_f, then the strain ε_f generated after they stacking together is

$$\varepsilon_f = \frac{a_s - a_f}{a_f} \qquad 3.3$$

and the corresponded stress σ_f is

$$\sigma_f = \frac{E_f}{(1 - \nu_f)}\varepsilon_f \qquad 3.4$$

From formula 3.3 and 3.4, we can calculated the require lattice constant difference of $a_{epilayer} - a_{substrate}$ is 0.0291 Å, -0.2049 Å and -0.4413 Å, and these values are too big for the lattice parameters of the wafers and epilayers determined from high resolution XRD scans as shown in Table 3.3 (lattice constant a varies from the third digit, i.e., 0.001 Å), and expected bow was calculated using the measured mismatch values and the Stoney equation (formula 3.1). The resulting maximum mismatch bow was calculated to result in radii of curvature larger than 1 km for all cases, which rendered the contribution from the point-defect-related mismatch insignificant.

For source (2), Since each dislocation segment adds strain energy to the system, the total strain energy will increase with increasing dislocation density. This can happen by generation of new threading dislocations or by elongation of the existing ones via inclination (glide and climb). Figure 3.12 shows the expected bow as a function of

dislocation density (dashed curves) employing the model proposed in Ref. [5]. The radius of curvature R and threading dislocation density ρ_{TD} has the relationship of

$$R = \frac{4B}{\rho_{TD} \tan \alpha} \qquad 3.5$$

where α is the inclination angle, and B is the fitting coefficient with unit of [m^{-1}], this coefficient in Ref. [5] is 6.0×10^{8} m^{-1}.

With the dark spot density as measured by 2PPL listed in Table 3.4, and TDI of 5º, 9º and 5º as shown in Figure 3.8, the calculated strain in ammonothermal, HVPE1 and HVPE2 sample by the model in Ref. [5] was 4.2e-7, 2.96e-5 and 5.19e-5, the stresses were 0.16 MPa, 11.52 MPa and 20.22 MPa.

For source (3), there is no analytical model to calculate this stress, only simulation result was found in Ref. [11]. The crystal at edges has a bigger lattice constant so it will provide a compressive stress to the crystal at center. This stress is related to growth time and crystal thickness. If we assume the compressive stress of the ammonothermal sample is all from source (3), i.e. -7 MPa, so the same compressive stress will also be applied to HVPE1 and HVPE2 sample.

Finally, the total stress for ammonothermal sample, HVPE1 sample and HVPE2 sample be -6.84 MPa, 4.52 MPa and 13.22 MPa. These calculation values are close to the measurement values in the Table 3.5.

3.2 Thick epitaxy growth technologies

3.2.1 HVPE GaN on ammonothermal GaN

The first HVPE GaN grown on ammonothermal GaN (Am-GaN) substrate was proposed by Sochacki in 2013 [12,13]. Substrate fabricated by HVPE GaN grown on Am-GaN substrate can repeat the crystallinity, but the lattice bow increased to 40 m. The growth rate of HVPE GaN epilayer on Am-GaN was studied in 2014 [14], maximum growth rate of 350 μm/h was achieved. Besides, the growth rate does not influence the structural properties of the growing crystal but will influence the purity of the

crystallizing material. HVPE GaN grown on Am-GaN substrate with different misorientation angle of 0.3, 0.5 and 1 degree to the [10$\bar{1}$0] direction and also to the [11$\bar{2}$ 0] direction were studied [3]. It demonstrated that crystallization process firstly follows the macro-step flow growth mode caused by the misorientation, then spiral growth mode dominate after all the steps was filled. Besides, HVPE-GaN grown on the Am-GaN seed misoriented to the [10$\bar{1}$0] direction have low etch pits density (EPD) at the level of the applied Am-GaN substrate, while crystal grown on that misoriented to the [11 $\bar{2}$ 0] direction have EPD two order of magnitude higher. By studying with transmission electron microscopy [15], the difference in EPD was attributed to the formation of micro-steps on polar the (10$\bar{1}$0) plane which is edge-on only for the [11$\bar{2}$ 0] direction but not to the [10$\bar{1}$0] direction. This is a slow growth plane, responsible for the formation of V-defects, where accumulation of a high density of impurities (especially oxygen). Later, the critical thickness of HVPE GaN/Am-GaN was studied [16]. If the HVPE GaN epilayer is thicker than 1.9 mm, then strain generated in the new grown material is too high and leads to the formation of many defects and finally the crystal was cracked. The increasing strain in HVPE epilayers on Am-GaN in the c-direction was attributed to non-polar and semi-polar growth of “wings” by Raman spectroscopy [17]. The wings will lead to formation of large stress in the growing crystal, close to its edges. Avoiding the lateral growth during crystallization in the c-direction seems crucial for developing GaN bulk growth technology.

3.2.2 Protection rings used for long time growth

Rings was used to protect the edge to prevent poly crystal growth on seed edge. The schematic and the actual picture of the ring is shown in Figure 3.12.

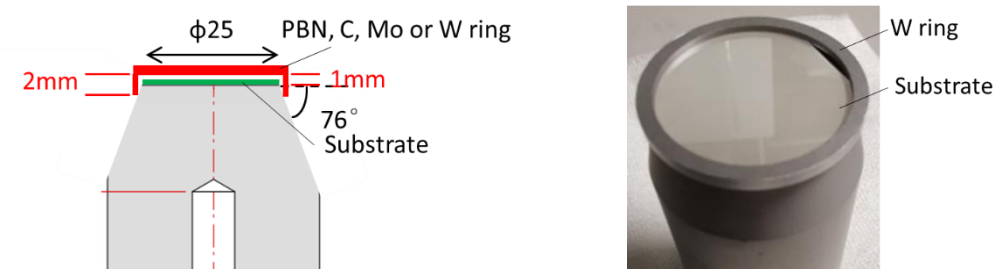

Figure 3.12 Ring on susceptor to protect the edge and fix the seed, (a) schematic, (b) actual picture

We have tested rings made of four different kinds of material, they are pyrolytic boron nitride (PBN), W, carbon, and Mo. The as-grown rings and rings during growth are shown in Figure 3.13.

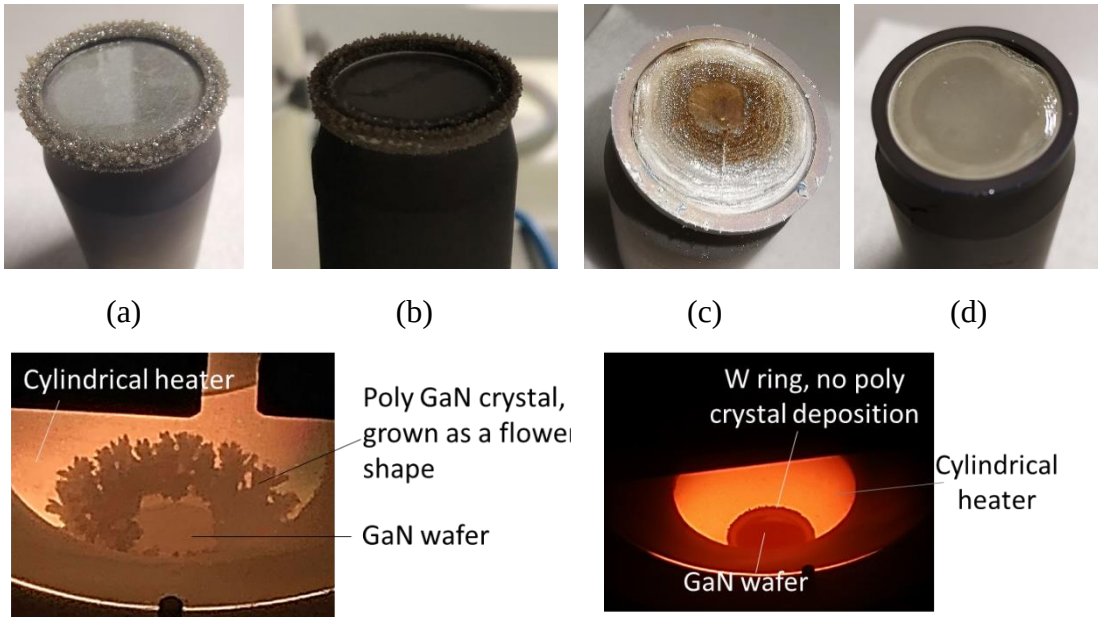

Figure 3.13 As-grown rings made of (a) PBN, (b) carbon, (c) Mo and (d) W; Rings during growth made of (e) Mo with poly crystal growth and (f) W without poly crystal growth

PBN ring cannot couple with RF power and heated by eddy current, but carbon ring has high electrical conductivity and can be heated by RF power. By comparing the result of PBN ring and carbon ring, we can have two conclusions. Firstly, both rings have poly crystalline grown on ring surface, both two materials are not preferred for

long time growth. Secondly, the temperature at edge would be different by using these two rings, i.e., the temperature with using C ring will be higher than that with using PBN ring, but the morphology at edge of the wafer are similar, so temperature difference at edge seems not enough to have any influence for neither poly crystalline deposition on the rings nor the epitaxial growth at edge. PBN coated carbon ring was not included in this experiment because it will neither change the poly crystal deposition nor have any influence to edge crystal growth.

Either W or Mo has catalytic effect to NH_3 and the decomposed hydrogen radicals can decompose GaN crystal. So, W and Mo rings were compared to prevent parasitic deposition during growth. Although both as-grown rings have no poly crystalline grown on the surface after growth (see Figure 3.14 (c) and (d)), there was actually poly crystalline on Mo ring surface during growth (see Figure 3.14 (e)). However, these poly-crystalline will automatically drop during cooling down process. W ring had no poly crystal growth during the whole process. From the experiment result, W has stronger catalytic effect to decompose GaN crystal.

W ring was finally selected for long time growth. However, the W ring cannot solve the lateral growth problem. There will also be laterally grown wings with W ring protect the seed edge, as shown in Figure 3.14.

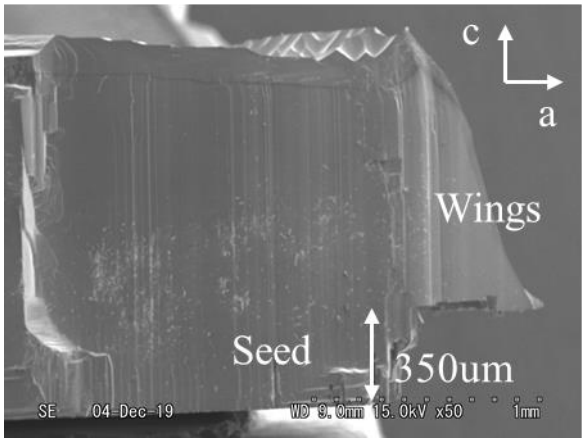

Figure 3.14 Laterally grown wings with W ring after 8 hours growth

In the future, we will try to upgrade current reactor and design a “growth channel” to fix the crystal size, then the lateral growth may be possibly fixed. The schematic diagram of the structure at growth zone is shown in Figure 3.15. A carbon susceptor with proper coating is surrounded by a W tube which can move up and down. The susceptor size should be just the same (or slightly bigger) with wafer, the channel between the W and susceptor should be as close as possible. The W tube thickness should select by experiment to achieve the following two goals. Firstly, it should be thin enough to ensure enough RF power that can penetrate the W tube and loaded on the susceptor. Secondly, it should be thick enough to make sure part of RF power can load on the W tube and ensure the W tube temperature higher than the susceptor. The top of the tube should be an inclined plane, so poly crystal deposited on the surface have change to slide down from the inclined surface. Based on current experiment, no poly crystal was observed depositing on the side surface of the ring, so there will be also no poly crystal depositing on the side surface of the tube. At beginning of growth, the tube is slightly higher than the susceptor, and the tube then slightly move upward at the same speed with growth rate to keep the distance of the tube top to wafer growth surface. With this design, the lateral growth can be prevented, and the growth mode should be always stable during the whole growth time.

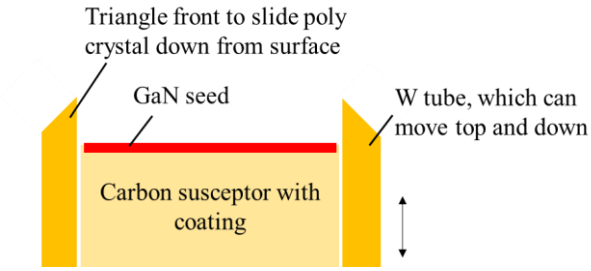

Figure 3.15 Schematic of the “growth channel” design.

3.2.3 Seed fixation and backside protection

In high temperature sublimation growth of SiC, the seed was chemically attached to the lid using molten sugar, while for AlN seed, AlN ceramic cement was always used. These two kinds of glue were tested to fix the seed in HVPE reactor as shown in Figure 3.16.

5 mg of sugar was weighted and uniformly coated onto susceptor surface, the calculated thickness of molten sugar layer was 5 μm. After growth, molten sugar decomposed into carbon but the seed cannot bond with the susceptor through this process, so the wafer automatically separated from the susceptor after growth. Molten sugar cannot be used to fix GaN seed in HVPE reactor. In another experiment, 350 mg AlN ceramic cement was coated onto susceptor surface, the calculated thickness of cement was approximately 20 μm. After growth, the seed was still bonded onto carbon susceptor, but the susceptor cannot be reused anymore, so this way of fixation was eventually deposited, too.

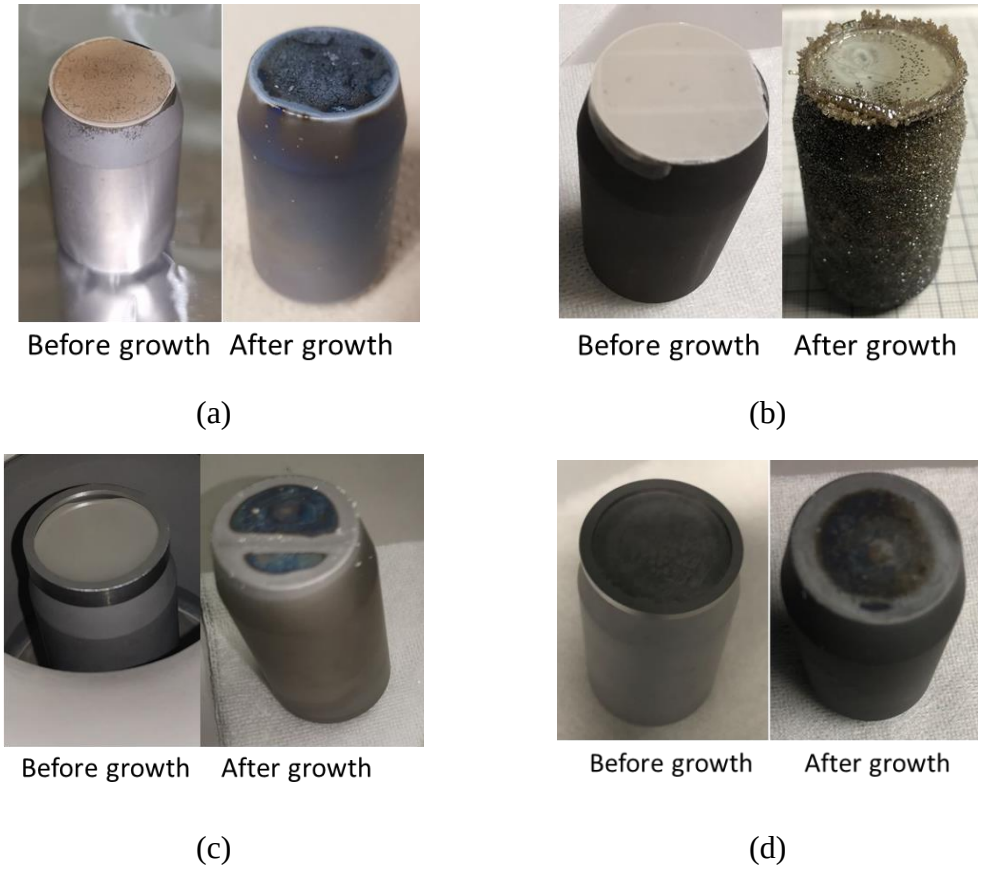

Figure 3.16 Seed fixation with (a) molten sugar, (b) AlN ceramic cement; Seed backside protection (c) with SiN coating and (d) without SiN coating

At last, W ring was designed and used to fix the seed position on the susceptor. And then we tested the backside protection with sputtering 10 μm SiN film on seed backside. After growth, Si element from SiN coating layer diffused into susceptor and make color

the susceptor blue, this is harm to the susceptor. Seed without any treatment was directly placed on susceptor and fixed by W ring.

Seed fixation and backside protection is important because for long enough growth time (typically several hundreds of hours), the edge of the bottom side of the seed may be decomposed and this will result in two problems. Firstly, temperature uniformity on the wafer growth surface may be changed. Secondly, threading dislocation may occur from seed backside and move upward to wafer surface and eventually worsen the growth morphology. GaN seed fixation is a new research area and there is not yet any relative report found. The commonly used cement does not fit the material and the growth atmosphere very well because there is HCl in the growth atmosphere so the cement should have strong corrosion resistance, or it will be decomposed during the growth.

Currently, this is not yet a problem because the growth time is only below 10 hours. Therefore, seed fixation without cement or backside protection is acceptable, but for longer growth time, this problem will become a limiting factor.

3.2.4 Long time growth of GaN on ammonothermal substrate

To achieve a higher growth rate, the growth procedure discussed in Section 3.1.2 was further optimized. The input HCl and NH_3 flow rate was increased to 30 and 3000 sccm, respectively, the pre-reaction zone temperature was 800 ℃, and the growth zone temperature was 1050 ℃. Flow condition 2 in Table 2.1 was selected for 8 hours growth. The total thickness after growth (including 350 μm seed) was 2.3 mm measured by a Vernier caliper. The estimated growth rate was 250 μm/h.

The as-grown wafer outlook and surface morphology are shown in Figure 3.17. The dominant growth mechanism is in spiral growth mode for thick crystal growth, where a spiral originates from threading screw dislocations after all the steps were fixed [3]. Step bunching was also observed on wafer surface close to edge. This growth mode were also reported on the basal plane growth of SiC and AlN crystals [18,19].

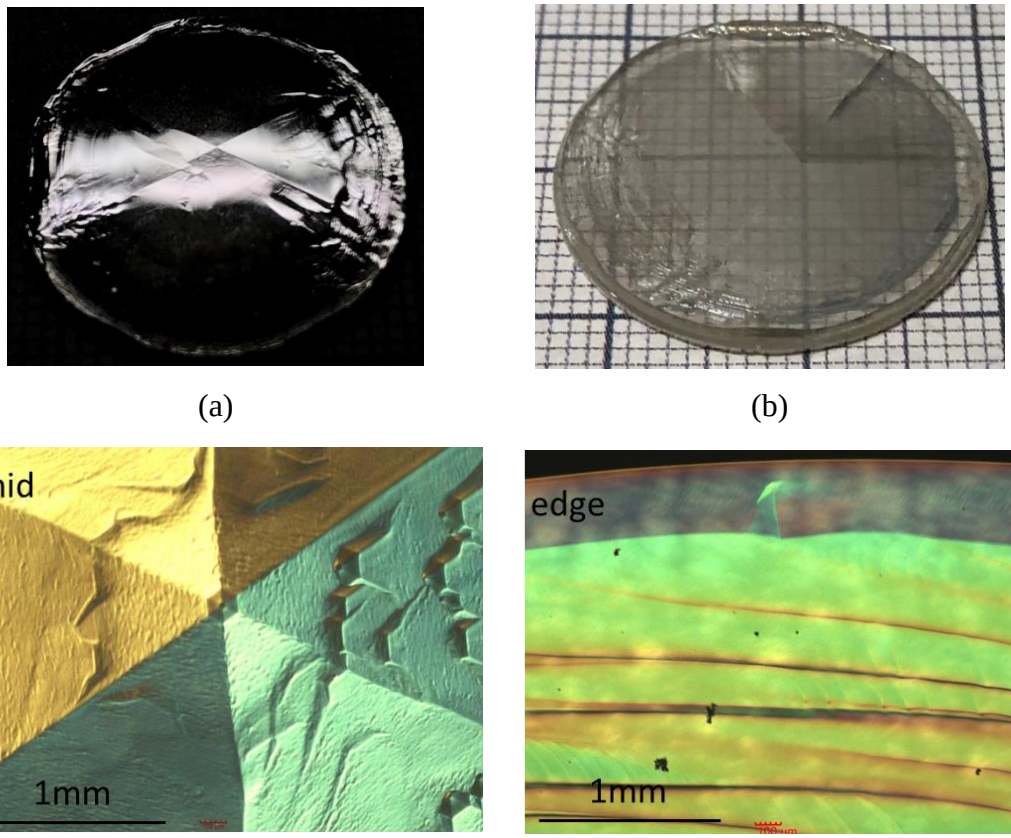

Figure 3.17 As-grown crystal after 8 hours growth, (a) reflection picture, (b) bird eye view and DIC image of (c) middle hillock and (d) edge step bunching.

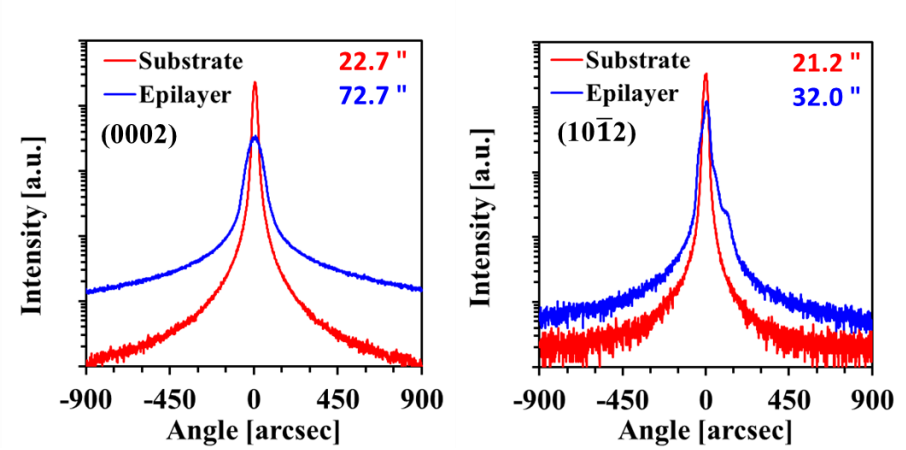

Figure 3.18 Rocking curve for substrate before growth and 2.3 mm epilayer on it.

The crystal quality degraded after growth. As shown in Figure 3.18, (0002) brodened and subpeaks appeared in $(10\bar{1}2)$ scan. The lattice bows also increased, the epilayer R_C was 6m (before growth, substrate R_C was 600m).

Surface with step bounching will stop growth because there is little low energy positions left on wafer surface (terrace or kink), which will further limit the growth time. Furthermore, regrowth method was also used for thick crystal growth.

3.2.5 GaN regrowth on HVPE GaN on ammonothermal-grown substrate

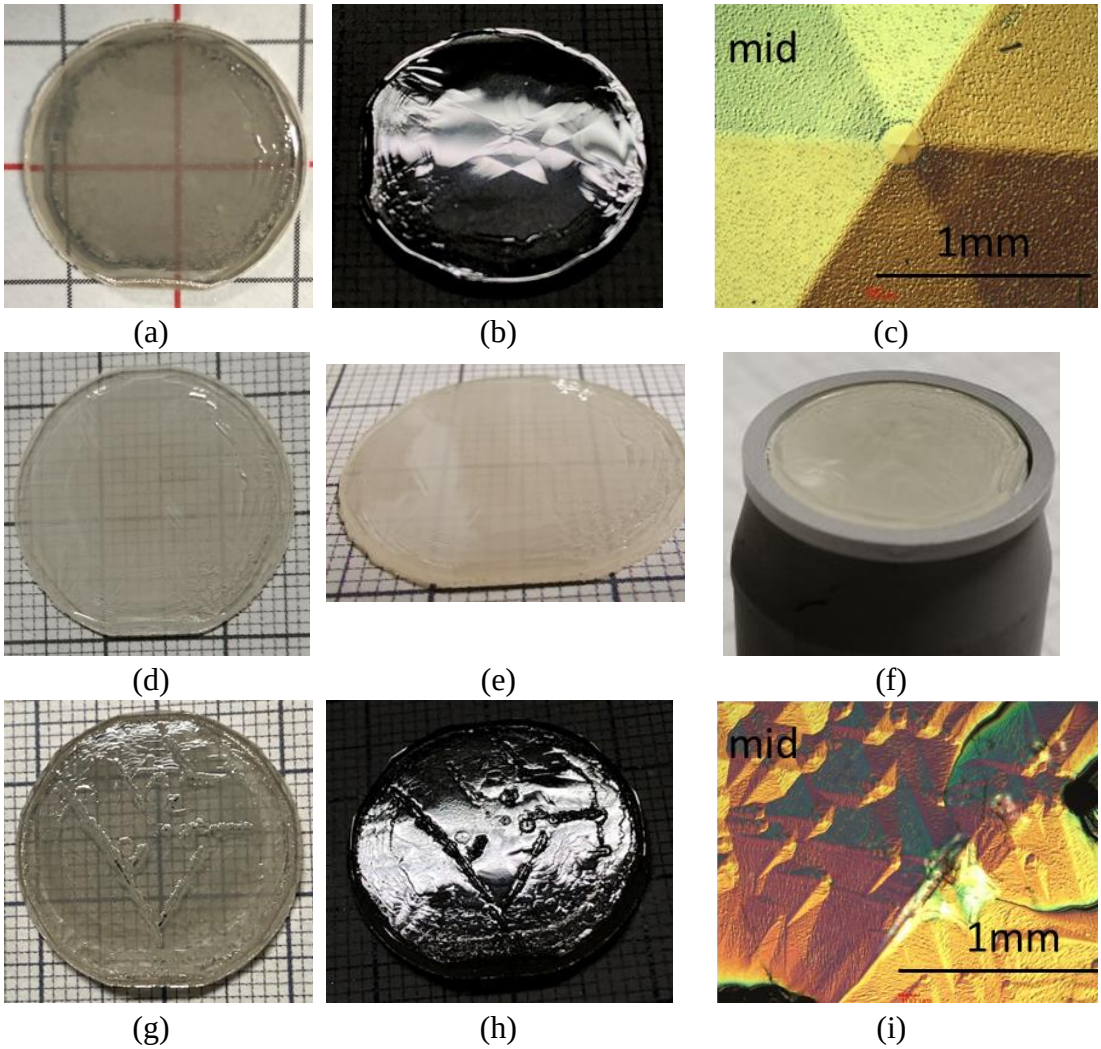

(a) (b) (c)

(d) (e) (f)

(g) (h) (i)

Figure 3.19 Regrowth technic, (a)-(c) as-grwon wafer photos and DIC image of center after first growth, (d)-(f) wafer photos after cleaning and mounted on the susceptor, (g)-(i) as-grown wafer photos and DIC image of center after second growth.

With the same growth conditions and growth procedure discussed in Section 3.2.4, first growth procedure of 6 hours was proceeded. 1.8 mm thick crack free crystal was obtained. The wafer was ultrasonic cleaned in acetone, methanol, isopropanol and pure water in order, and the cleaning time was 5 mins for each step. Then the wafer was dried under nitrogen gun. After cleaning the as-grown wafer, a second growth with the same growth condition of another 6 hours was proceeded. Finally, crack appeared on wafer surface but merged later during growth. But the morphology was ruined due to the crack. The final total thickness of the sample was 3.2 mm. The wafer pictures during these procedures are shown in Figure 3.19.

3.3 Summary of thick epitaxial growth technology

In this chapter, the key factors that influence the thick epitaxial growth were surveyed. They are seed selection, edge protection, seed fixation, long time growth and regrowth.

In seed selection section, homoepitaxial crystal growth on seeds fabricated by different methods were proceeded. The morphology, crystallinity, radii of curvature, dislocation density and dislocation propagation at interface were evaluated. Three facts are key to thick epilayer growth. Firstly, the epilayer can succeed the crystallinity from the substrate, i.e., epilayer on the substrate with higher crystallinity will also result in a better crystallinity. Secondly, the stress for all the seeds will increase after epilayer growth regardless of the substrate is under compressive stress or tensile stress. Thirdly, the dislocation bundles generated at interface will worsen the epilayer quality. Considering the above three facts, ammonothermal substrate was finally selected for thick epilayer owning to its supreme advantages in high crystallinity, flat lattice bow and no dislocation bundle generation at interface.

In edge protection section, protection rings made of four kinds of different material were tested in the growth experiments. W ring was selected for long time growth owing to its catalytic effect in preventing parasitic deposition.

In seed fixation and backside protection section, different methods were tested including seed fixation by sugar or AlN ceramic cement, backside protection by SiN thin film. None of these methods work out well. Finally, W ring was temporarily used to fix the seed because the growth time is below 10 hours and seed fixation is not yet a serious problem.

With the above preparation, long time growth on ammonothermal substrate was proceeded with W ring protecting the edge. The growth rate of 250 μm/h and thickness of 2.3 mm were finally achieved after 8 hours growth.

Regrowth technic showed there is a limit thickness for the epilayer with the current configuration, epilayer thicker than this critical value will result in the crack in the epilayer.

3.4 References

[1] *Bryan, Z. Bryan, S. Mita, A. Rice, J. Tweedie, R. Collazo, Z. Sitar, Surface kinetics in AlN growth: A universal model for the control of surface morphology in III-nitrides, J. Cryst. Growth. 438 (2016) 81–89. https://doi.org/10.1016/j.jcrysgro.2015.12.022.*

[2] *M. Bockowski, Z. Sitar, Hybrid approach yields the best GaN crystals and wafers, Compd. Semicond. 20 (2014) 48–51.*

[3] *T. Sochacki, M. Amilusik, B. Lucznik, M. Fijalkowski, J.L. Weyher, G. Nowak, B. Sadovyi, G. Kamler, R. Kucharski, M. Iwinska, I. Grzegory, M. Bockowski, HVPE-GaN growth on misoriented ammonothermal GaN seeds, J. Cryst. Growth. 403 (2014) 32–37. https://doi.org/10.1016/j.jcrysgro.2014.06.020.*

[4] *C.T. Shelton, I. Bryan, E.A. Paisley, E. Sachet, J.F. Ihlefeld, N. Lavrik, R. Collazo, Z. Sitar, J.-P. Maria, Step-free GaN surfaces grown by confined-area metal-organic vapor phase epitaxy, APL Mater. 5 (2017) 096109. https://doi.org/10.1063/1.4993840.*

[5] *H.M. Foronda, A.E. Romanov, E.C. Young, C.A. Robertson, G.E. Beltz, J.S. Speck, Curvature and bow of bulk GaN substrates, J. Appl. Phys. 120 (2016) 035104. https://doi.org/10.1063/1.4959073.*

[6] *T. Tanikawa, K. Ohnishi, M. Kanoh, T. Mukai, T. Matsuoka, Three-dimensional imaging of threading dislocations in GaN crystals using two-photon excitation photoluminescence, Appl. Phys. Express. 11 (2018) 031004. https://doi.org/10.7567/APEX.11.031004.*

[7] *Tanaka, K. Nagamatsu, S. Usami, M. Kushimoto, M. Deki, S. Nitta, Y. Honda, M. Bockowski, H. Amano, V-shaped dislocations in a GaN epitaxial layer on GaN substrate, AIP Adv. 9 (2019) 095002. https://doi.org/10.1063/1.5114866.*

[8] P.F. Fewster, Estimating the structure factors in X-ray diffraction, Acta Crystallogr. Sect. Found. Adv. 74 (2018) 481–498. https://doi.org/10.1107/S2053273318007593.

[9] V.M. Kaganer, O. Brandt, A. Trampert, K.H. Ploog, X-ray diffraction peak profiles from threading dislocations in GaN epitaxial films, Phys. Rev. B. 72 (2005) 045423. https://doi.org/10.1103/PhysRevB.72.045423.

[10] G.G. Stoney, The tension of metallic films deposited by electrolysis, Proc. R. Soc. Lond. Ser. Contain. Pap. Math. Phys. Character. 82 (1909) 172–175. https://doi.org/10.1098/rspa.1909.0021.

[11] J.Z. Domagala, J. Smalc-Koziorowska, M. Iwinska, T. Sochacki, M. Amilusik, B. Lucznik, M. Fijalkowski, G. Kamler, I. Grzegory, R. Kucharski, M. Zajac, M. Bockowski, Influence of edge-grown HVPE GaN on the structural quality of c-plane oriented HVPE-GaN grown on ammonothermal GaN substrates, J. Cryst. Growth. 456 (2016) 80–85. https://doi.org/10.1016/j.jcrysgro.2016.07.043.

[12] T. Sochacki, M. Amilusik, B. Lucznik, M. Boćkowski, J.L. Weyher, G. Nowak, B. Sadovyi, G. Kamler, I. Grzegory, R. Kucharski, M. Zajac, R. Doradzinski, R. Dwilinski, HVPE-GaN growth on ammonothermal GaN crystals, in: Gallium Nitride Mater. Devices VIII, International Society for Optics and Photonics, 2013: p. 86250B. https://doi.org/10.1117/12.2003699.

[13] T. Sochacki, Z. Bryan, M. Amilusik, R. Collazo, B. Lucznik, J.L. Weyher, G. Nowak, B. Sadovyi, G. Kamler, R. Kucharski, M. Zajac, R. Doradzinski, R. Dwilinski, I. Grzegory, M. Bockowski, Z. Sitar, Preparation of Free-Standing GaN Substrates from Thick GaN Layers Crystallized by Hydride Vapor Phase Epitaxy on Ammonothermally Grown GaN Seeds, Appl. Phys. Express. 6 (2013) 075504. https://doi.org/10.7567/APEX.6.075504.

[14] T. Sochacki, M. Amilusik, M. Fijalkowski, B. Lucznik, J.L. Weyher, I. Grzegory, R. Kucharski, M. Iwinska, M. Bockowski, Examination of growth rate during hydride vapor phase epitaxy of GaN on ammonothermal GaN seeds, J. Cryst. Growth. 407 (2014) 52–57. https://doi.org/10.1016/j.jcrysgro.2014.09.007.

[15] Z. Liliental-Weber, R. dos Reis, T. Sochacki, M. Bockowski, The influence of the substrate misorientation on the structural quality of GaN layers grown by HVPE, J. Cryst. Growth. 498 (2018) 346–351. https://doi.org/10.1016/j.jcrysgro.2018.07.010.

[16] T. Sochacki, M. Amilusik, M. Fijalkowski, M. Iwinska, B. Lucznik, J.L. Weyher, G. Kamler, R. Kucharski, I. Grzegory, M. Bockowski, Examination of defects and the seed's critical thickness in HVPE-GaN growth on ammonothermal GaN seed, Phys. Status Solidi B. 252 (2015) 1172–1179. https://doi.org/10.1002/pssb.201451604.

[17] M. Amilusik, D. Wlodarczyk, A. Suchocki, M. Bockowski, Micro-Raman studies of strain in bulk GaN crystals grown by hydride vapor phase epitaxy on ammonothermal GaN seeds, Jpn. J. Appl. Phys. 58 (2019) SCCB32. https://doi.org/10.7567/1347-4065/ab1390.

[18] J. Giocondi, G.S. Rohrer, M. Skowronski, V. Balakrishna, G. Augustine, H.M. Hobgood, R.H. Hopkins, An atomic force microscopy study of super-dislocation/micropipe complexes on the 6H-SiC(0 0 0 1) growth surface, J. Cryst. Growth. 181 (1997) 351–362. https://doi.org/10.1016/S0022-0248(97)00303-5.

[19] R.R. Sumathi, Bulk AlN single crystal growth on foreign substrate and preparation of free-standing native seeds, CrystEngComm. 15 (2013) 2232–2240. https://doi.org/10.1039/C2CE26599K.

Chapter 4

4 Large size wafer growth

4.1 Reactor structure

The actual picture and schematic diagram of the home-built vertical reactor for large size wafer growth is shown in Figure 4.1. To avoid GaCl from spontaneously self-reaction on the reactor wall at temperature lower than 500 ºC, which can form Ga metal and $GaCl_3$, the vertical reactor has a classical hot-wall design with resistively heated multiple zone furnace systems. The heterogeneous GaN nucleation on showerhead can lead to GaN parasitic deposition, and small particles of parasitic deposition may frequently fall on as growing GaN layer surface. These particles may finally lead to small pits on GaN layer surface as reported in Ref. [1]. We designed the inverted wafer configuration to conquer this problem. With an inverted wafer design, the gravity is opposite to the direction of gas flow and can lead to better uniformity of species near the substrate [2]. The process-relevant gas inlets and the exhaust gas outlet are both located at the bottom. Two purge gas inlets are implanted at the top and the bottom, respectively. The purge gas can help to prevent back diffusion of exhaust gas. The flow is denoted by the arrows in the figure. The wafer is placed in a wafer holder which can rotate at a maximum speed of 10 rpm with either clockwise or counter clockwise. This slow rotation can help to improve the crystal growth uniformity. The Ga tank was equally split to two independent part, where pre-reaction of inner flow and outer flow

proceed independently.

The reactor is heated by a resistively heated multiple zone (six zones, namely zone 1 to 6 from top to bottom) furnace.3 sets of semitransparent quartz plate (set 1 to 3 from top to bottom) were used as thermal isolators to create two temperature zone for pre-reaction and GaN crystal growth, respectively. 6 thermocouples planted in the middle of each zone are used to detect the temperature of each zone, a pyrometer on top is used to monitor the temperature on wafer back surface. The temperature distribution through zone 2 to zone 6 plotted on the left was measured along the center position with a dummy quartz showerhead. GaN crystal growth is in zone 2 and pre-reaction is between zone 4 and 5. The temperature was uniformly controlled along vertical direction. Besides, the semitransparent quartz plate thermal isolators are very effective. The temperature difference along radius is within 10 ºC.

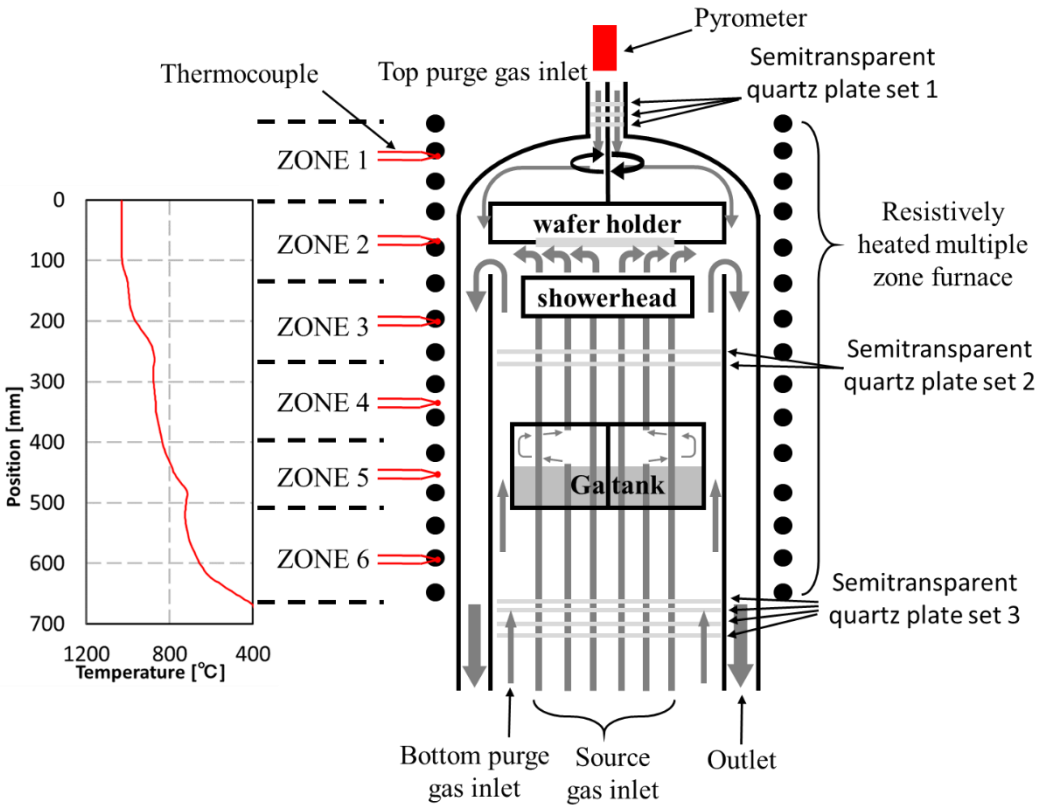

Figure 4.1 Schematic of the HVPE reactor for large wafer growth

Figure 4.2 shows the showerhead structure. The process-relevant gases flow onto wafer surface across the entire showerhead surface. The distance from showerhead to wafer is 30 mm. The gas inlets are well designed so that individual gases are separated by many narrow tubes up to the showerhead surface. The whole showerhead surface is divided into inner and outer regions. The flow of inner region (inner flow) and outer region (outer flow), separated by inner/outer region boundary line in the figure, are controlled by two sets of independent gas supply systems. This design brings additional control ability on the input mass flux. For each gas supply system, there are three kinds of nozzles, namely GaCl nozzles, NH_3 nozzles and barrier nozzles. The distribution of the nozzle is shown in the figure. Each nozzle insists of a source gas nozzle and a surrounded ring type barrier nozzle. N_2 from barrier nozzle can make the mixing of source gas far from showerhead surface in order to help preventing parasitic deposition on the showerhead. Showerhead was made of BN ceramic material. This material has high chemical stability. W plate was placed on showerhead surface to further decompose the slightly deposited GaN poly crystalline on showerhead surface.

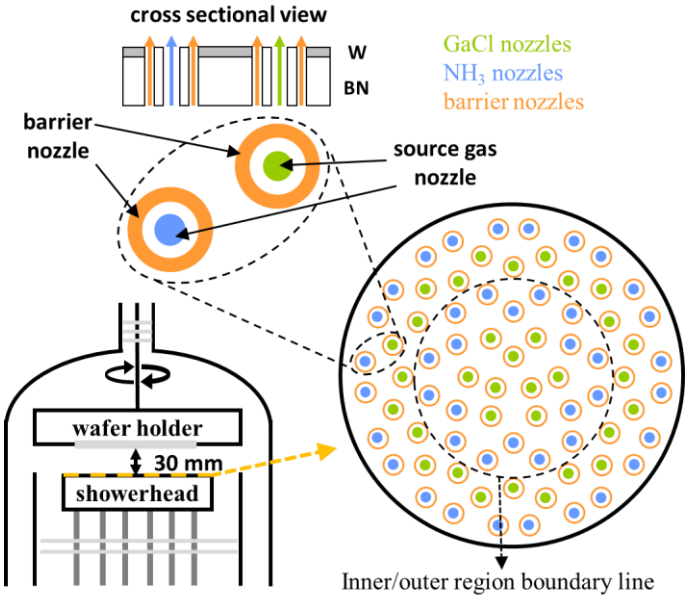

Figure 4.2 Showerhead structure.

The actual of the reactor, the wafer holder and the showerhead are shown in Figure 4.3.

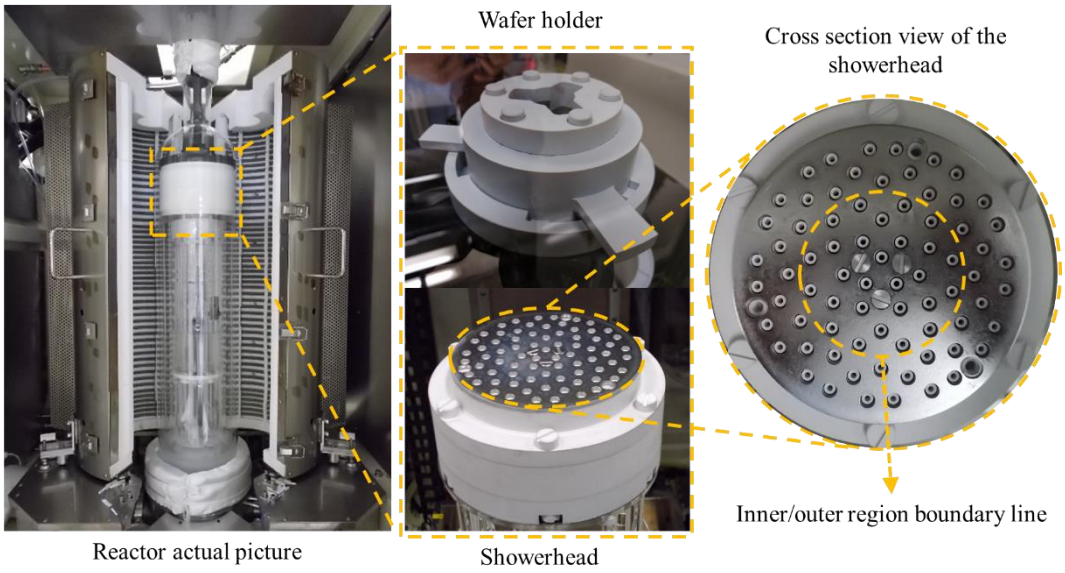

Figure 4.3 Actual picture of the reactor, showerhead and wafer holder.

4.2 Growth condition optimization

The flow of the system was also optimized through dozens of experiments with the similar method introduced in Chapter 2. Because there are two independently controlled gas supply system in this reactor, flow balance from showerhead was especially studied, including the flow speed ratio of inner flow to outer flow, the flow speed ratio of barrier gas flow to source gas flow. However, the concentration of source gas for both inner flow and outer flow were the same to reduce the complexity. Different inner/outer source gas concentration was only studied by simulation, and will be introduced in Section 4.4. Eventually, the optimized growth condition is listed in Table 4.1.

Table 4.1 The optimized growth condition of the reactor for large size wafer growth

Condition for pre-reaction zone		**Unit**	**Inner line**	**Outer line**
Total flow		sccm	400	400
HCl flow		sccm	38	102
H_2 flow		sccm	0	0
N_2 flow		sccm	362	298
HCl concentration		a.u.	9.5%	25.5%
Flow residence time		second	45	45
Ga tank temperature		ºC	850	
Condition for flow from showerhead		**Unit**	**Inner line**	**Outer line**
Inner + Outer	Total flow	sccm	13173	
Inner / Outer	Total flow	sccm	3654	9519
From GaCl nozzles	Total flow	sccm	545	2182
	GaCl flow	sccm	38	102
	N_2 flow	sccm	507	2080
	H_2 flow	sccm	0	0
From NH3 nozzles	Total flow	sccm	1429	2857
	NH_3 flow	sccm	1200	1600
	N_2 flow	sccm	229	1257
	H_2 flow	sccm	0	0
From barrier nozzles	N_2 flow	sccm	1680	4480
	H_2 flow	sccm	0	0
Inner + Outer	Average flow speed	cm/s	3.9	
Inner / Outer	Average flow speed	cm/s	3.5	4.1
Inner / Outer	From GaCl nozzles	cm/s	32.1	48.2
Inner / Outer	From NH_3 nozzles	cm/s	42.1	63.2
Inner / Outer	From barrier nozzles	cm/s	14.7	22.0
Condition of growth zone		**Unit**	**Inner line**	**Outer line**
GaCl concentration		%	1.0	1.0
NH_3 concentration		%	32.8	16.8
H_2 concentration		%	0.0	0.0
V/III		a.u.	20	
Growth temperature		ºC	1080	
Rotation		rpm	6	
Pressure		atm	1.0	

The flow speed from each nozzle are calculated by dividing the flow rate with corresponded nozzle total area, respectively. The average flow speed was calculated by

dividing corresponded showerhead area. The ratio of showerhead total area to nozzle total area is 7.4. The GaCl line is similarly to the structure shown in Figure 2.8 (b), namely, the flow from Ga tank will mix with the flow from dopant line, and the mixed gas finally flow out through inner and outer GaCl nozzles on the showerhead, respectively.

For the growth at pre-reaction zone, the residence time is enough for the reaction fully proceeding. Difference of HCl conversion rate is small enough to be omitted because the Ga tank temperature is high enough (within 5% as shown in Figure 2.2 (d)). NH3 is saturated and the growth rate is controlled by HCl flow. The GaCl concentration of inner and outer flow system are the same. The outer flow speed is slightly higher than the inner flow speed.

With this optimized flow speed, growth rate of GaN film on big area of 4-inch diameter can be uniformly achieved as shown in Figure 4.4. The growth rate was measured by SEM cross sectional with accuracy of ±1 μm.

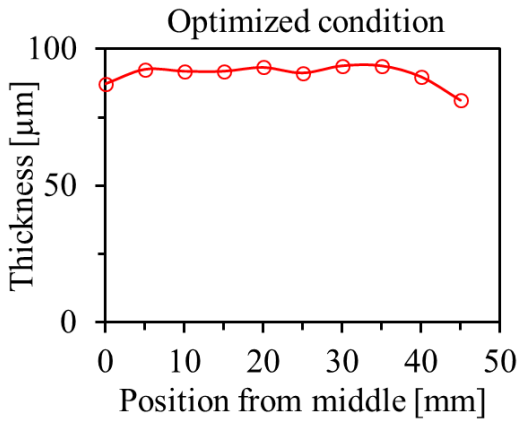

Figure 4.4 Epilayer thickness distribution along the radius direction from wafer center (0 mm) to edge (50 mm).

4.3 Showerhead with W surface

W has catalyst effect to decompose GaN crystal which was studied with various of ELOG growth [3-5]. GaN crystal was decomposed under W mask and void was observed.

The reason was attributed to the generation of H_2 molecules or their radicals by catalyst effect of W to NH_3 [6,7].

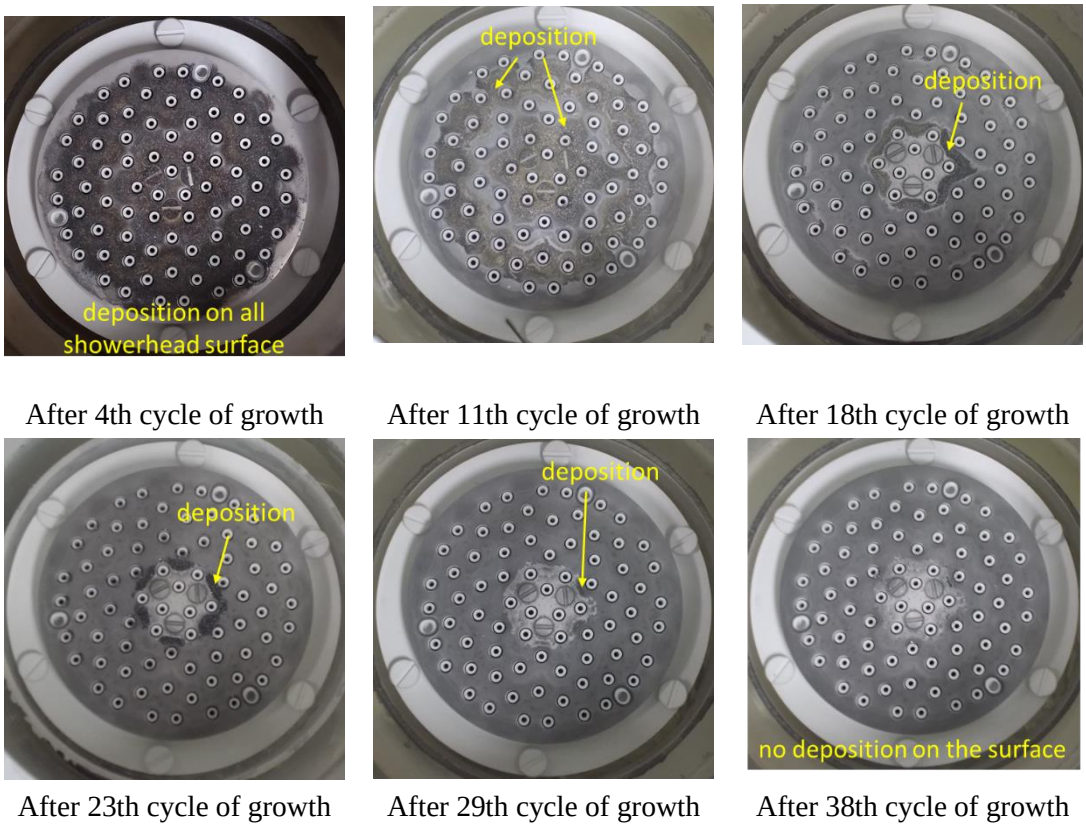

After 4th cycle of growth | After 11th cycle of growth | After 18th cycle of growth

After 23th cycle of growth | After 29th cycle of growth | After 38th cycle of growth

Figure 4.5 Photo of showerhead with W plate just after growth procedure, the dark color pattern is the GaN poly crystal deposited on W surface after growth, the dark color pattern area decreased with increasing of growth cycles.

The showerhead has a W surface to decompose the GaN poly crystal synthesized on the surface of showerhead. We observed that the ability of W to decompose GaN will strengthen with the increasing number of cycles of aging as shown in Figure 4.5. Each cycle of aging including 1 hour of crystal growth procedure with flowing of 1% of GaCl and 20% of NH_3 in N_2 atmosphere under 1080 ºC, and 1 hour of baking procedure with flowing of 1% of HCl in H_2 atmosphere under 1100 ºC. All the showerhead shown in Figure 4.5, the growth condition was the same, so the change of the deposition pattern can show the increasing ability of W decomposition on GaN. After the 4th cycle of growth, GaN poly will synthesize on the whole W plate surface. After 11th cycle,

surrounding area of GaCl nozzles on the showerhead have deposition and formed a big ring and a small ring. After 18th cycle, the big ring disappeared, and the small ring area decreased. After 23th cycle of growth and 29th cycle of growth, poly crystal deposition area kept decreasing, and eventually after 38th cycle of growth, no deposition on the surface was observed.

Currently, why the GaN poly crystalline decomposition ability enhancement of W is still unknown. Possible estimation is the synthesis of WN on the W plate surface after several round of treating.

(a) (b) (c)

Figure 4.6 Photo of showerhead with W plate after 10 hours growth, (a) top view, (b) bird eye view, (c) side view.

To further demonstrate the GaN crystal decomposition ability of W, 10 hours growth was proceeded. The showerhead after growth was shown in Figure 4.6. Although there is still region where GaN poly deposition remained, what is really exciting is that there is region that no deposition on W at all. Furthermore, the region with GaN poly deposition can be eventually improved by adjusting the flow speed of barrier nozzles and source gas nozzles. This result also demonstrate that W has the potential to decompose the poly crystal after long enough aging cycles without barrier gas to delay the gas mixing. Based on this concept, the showerhead version II was designed.

4.4 Design of new showerhead

4.4.1 Design concept

As discussed in last section, in the new showerhead, we cancelled the barrier gas, then the nozzle size can be decreased, nozzle density can be increased, and total flow can be decreased. These changes finally result to a much shorter mixing distance, so wafer can be placed closer to the showerhead. As discussed in Figure 2.7 (c), with decreasing H_C, both growth rate and source gas yield can be improved. Besides, in new version of showerhead, GaCl nozzles and NH_3 nozzles arrangement was also improved to further shorten gas mixing distance.

4.4.2 Simulation model and calculation procedure

An axisymmetric vertical reactor geometry with wafer face-down and showerhead configuration is taken into consideration here. A two-dimensional (2-D) simulation model for the growth zone of the reactor has been used for numerical modeling. The schematic illustration of the geometry and mesh grids of the model are shown in Figure 4.7.

The reactor has an inverse-flow showerhead configuration, and two purge gas lines were employed to speed up the flow speed of gas mixture to avoid additional parasitic deposition on the quartz wall. One geometrical irregularity of this model is the wafer holder which rotates the wafer. In numerical model, the influence of wafer holder to the flow is nontrivial due to its comparable thickness (3 mm) with the distance between showerhead and wafer surface (15 mm). The problem was further simplified by cancelling the gas mixing process after showerhead. The inner and outer input gas has been pre-mixed in the gas mixing blocks before being injected through ring shape nozzles on the showerhead. However, the input inner and outer source gas concentration and flow rate can be separately controlled.

The distance (H) between showerhead and wafer is 15 mm, wafer radius (R0) is 50.4 mm (4 inch), effective wafer area radius (R) is 48 mm, showerhead inner region radius (SR1) is 24.5 mm, and showerhead outer region outer edge radius (SR2) is 48.5 mm.

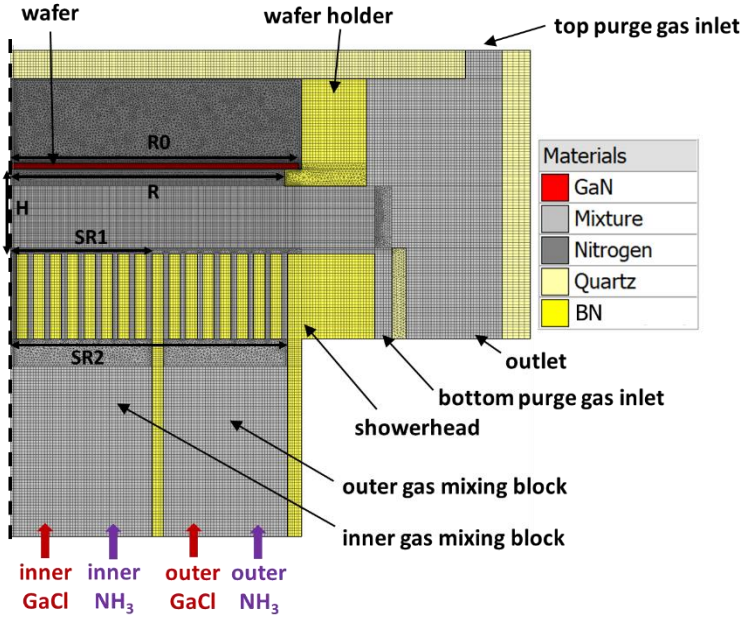

Figure 4.7 Simplified axial rotation 2-D simulation model.

Both non-uniform and uniform mesh grids were used (in the mesh grid shown in Figure 4.7). And special care was taken in the regions where large variation of the velocity and chemical species were expected. We had totally over 50000 cells and over 4000 boundary faces in each simulation. The simulator control criterion were convergence and maximum number of iterations. Residual values can directly quantify the error in the solution of the system of equations and is used as convergence criterion. The residual criterion for temperature, chemical species, velocity, pressure, and growth rate were 10^{-3}, 10^{-7}, 10^{-5}, 10^{-3} and 10^{-3}, and the maximum number of iterations was 50000.

4.4.3 Parameters definition and simulation conditions

The input concentration of GaCl $\boldsymbol{C_{input}}$ is proportional to GaCl partial density in the gas mixture $\boldsymbol{\rho_{GaCl}}$ due to the pre-mixing.

$$\mathbf{C_{input}} = \frac{\mathbf{Q_{GaCl}}}{\mathbf{Q_{total}}} \propto \frac{\mathbf{n_{GaCl}}}{\mathbf{n_{total}}} \frac{\mathbf{M_{GaCl}}}{\mathbf{V_m}} = \frac{\mathbf{m_{GaCl}}}{\mathbf{V_{total}}} = \boldsymbol{\rho}_{\mathbf{GaCl}} \quad 4.1$$

where $\boldsymbol{Q_{GaCl}}$ is the flow rate of input GaCl, $\boldsymbol{Q_{total}}$ is the total flow rate of the gas mixture, $\boldsymbol{n_{GaCl}}$ is the molar quantity of GaCl, $\boldsymbol{n_{total}}$ is the molar quantity of the gas mixture, $\boldsymbol{M_{GaCl}}$ is the molar mass of GaCl (105.176 g/mol), $\boldsymbol{V_m}$ is the standard volume of 1 mole of an ideal gas at standard temperature and pressure (22.4 L/mol), $\boldsymbol{m_{GaCl}}$ is the mass of input GaCl, $\boldsymbol{V_{total}}$ is the total volume of the gas mixture, and $\boldsymbol{\rho_{GaCl}}$ is GaCl density of the gas mixture.

The average input flow velocity $\boldsymbol{V_{input}}$ of gas mixture from ring shape nozzles is another key factor that influence the GaCl arriving quantity on wafer surface, and is the same as GaCl velocity due to pre-mixing.

$$\mathbf{V_{input}} = \frac{\mathbf{Q_{total}}}{\mathbf{S_{nozzle}}} \propto \mathbf{v_{GaCl}} \quad 4.2$$

where $\boldsymbol{S_{nozzle}}$ is the total area of the ring-shape nozzles that are connected to inner or outer gas mixing blocks.

The product of $\boldsymbol{V_{input}}$ and $\boldsymbol{C_{input}}$ ($\boldsymbol{VC\ product}$) is proportional to mass flux of GaCl $\boldsymbol{J_{m,GaCl}}$.

$$\mathbf{VC\ product} = \mathbf{V_{input}} \cdot \mathbf{C_{input}} \propto \boldsymbol{\rho}_{\mathbf{GaCl}} \cdot \mathbf{v_{GaCl}} = \mathbf{J_{m,GaCl}} \quad 4.3$$

For easy to use, we chose $\boldsymbol{V_{input}}$, $\boldsymbol{C_{input}}$ and $\boldsymbol{VC\ product}$ as key simulation parameters.

Due to the independent control of inner and outer flow, we define inner $\boldsymbol{C_{input}}$ and inner $\boldsymbol{V_{input}}$ as $\boldsymbol{C_{inner}}$ and $\boldsymbol{V_{inner}}$, outer $\boldsymbol{C_{input}}$ and outer $\boldsymbol{V_{inner}}$ as $\boldsymbol{C_{outer}}$ and $\boldsymbol{V_{outer}}$ for simplification.

The carrier gas was pure nitrogen (N_2). We only changed $\boldsymbol{V_{inner}}$, $\boldsymbol{V_{outer}}$, $\boldsymbol{C_{inner}}$ and $\boldsymbol{C_{outer}}$ and kept other conditions constant. The common simulation conditions are shown in Table 4.2.

Table 4.2 Common simulation conditions used in all simulation experiments.

Pressure	Growth temperature	Wafer rotation	Growth time	V/III ratio	Top purge gas flow	Bottom purge gas flow
Pa	K	rpm	min		slm	slm
101325	1330	6	60	20	1	1

In simulation experiment one, we compared different flow conditions between the conventional showerhead reactor and this reactor by two subsets of simulation experiments. In subset one, for each $\boldsymbol{C_{inner} = C_{outer}}$ value of 1.00%, 0.75%, 0.50% and 0.10%, we had 10 different $\boldsymbol{V_{inner} = V_{outer}}$ values of 0.001, 0.002, 0.005, 0.01, 0.02, 0.05, 0.1, 0.2, 0.4, 1 m/s. In subset two, $\boldsymbol{C_{inner}}:\boldsymbol{C_{outer}} = 2:1$, and for both $\boldsymbol{C_{inner}}$ value of 1.58%, 1.19%, 0.79%, 0.16% and $\boldsymbol{C_{outer}}$ value of 0.79%, 0.59%, 0.40%, 0.08%. The values for $\boldsymbol{V_{inner} = V_{outer}}$ are the same as subset one.

In simulation experiment two, we performed simulations with four different models (model I~IV), the inner/outer region area ratio of the showerhead changed from 0.023 to 0.943, as shown in Figure 4.8.

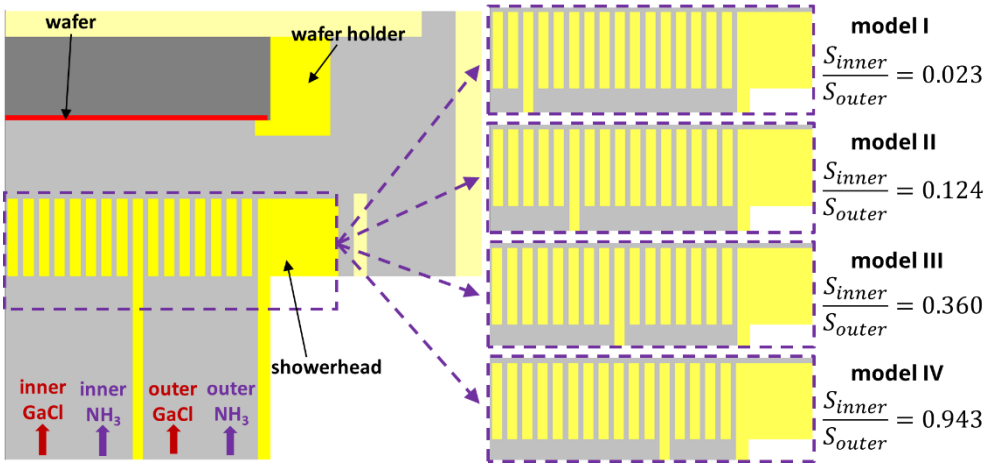

Figure 4.8 Four different showerhead configurations of the simulation models.

The $\boldsymbol{VC\ product}$ of both inner flow and outer flow for all the simulations in experiment two were fixed to be 0.001, and the total input GaCl flow was fixed to be 153.86 sccm. For each simulation model (model 1-4), $\boldsymbol{C_{inner}}:\boldsymbol{C_{outer}}$ includes 8 different values of 1:1, 1.5:1, 2:1, 2.5:1, 3:1, 3.5:1, 4:1, and 5:1, $\boldsymbol{V_{inner}}:\boldsymbol{V_{outer}}$ were the corresponding reciprocals.

4.4.4 Results and discussion

The results obtained by the simulator include flow field distribution, crystal growth rate on wafer surface, and chemical species composition distribution of the gas mixture in the reactor. However, to study the influence of the input mass flux to the crystal growth in the reactor, we developed three parameters to evaluate the simulation result. These three parameters are average growth rate $\overline{g_r}$, Ga yield η and crystal thickness distribution uniformity DU. They are defined in equations 4.4-4.6.

$$\overline{g_r} = \frac{V_{GaN}}{S \cdot t} \tag{4.4}$$

$$\eta = \frac{n_{GaN}}{n_{GaCl}} \tag{4.5}$$

$$DU = 1 - \sqrt{\frac{\sum_{i=1}^{N}(g_{r,i} - \overline{g_r})^2}{N-1}} / \overline{g_r} \tag{4.6}$$

where V_{GaN} is the grown GaN crystal volume with growth time of t, S is the wafer area, n_{GaN} and n_{GaCl} is the molar quantity of the GaN crystal and GaCl, $g_{r,i}$ is the growth rate at **i**th point, N is the total point number for calculating thickness distribution uniformity.

In a HVPE reactor, the growth rate is limited by input GaCl flow if input NH_3 flow is high enough. This is because that Cl atom has a relatively high adsorption speed, so the reaction rate is not limited by the surface kinetics. With the input V/III ratio being 20, the arrival rate of GaCl molecule to wafer surface is the limiting factor that determines the growth rate.

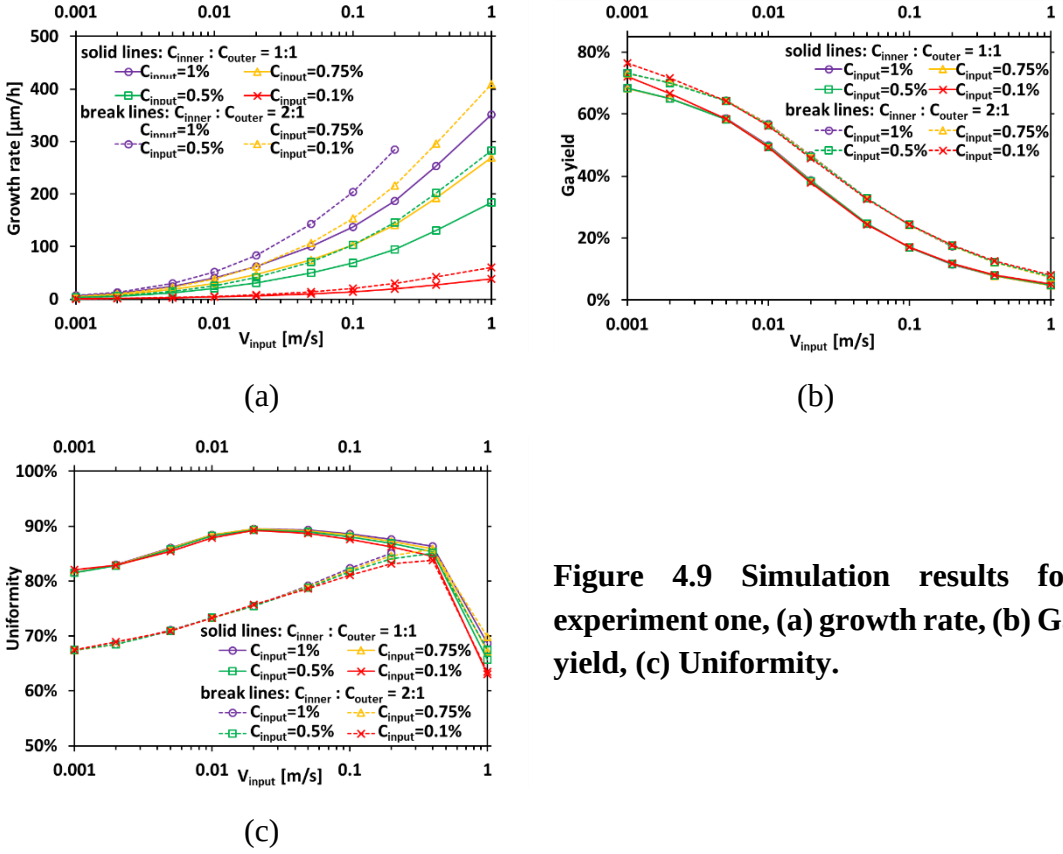

Figure 4.9 Simulation results for experiment one, (a) growth rate, (b) Ga yield, (c) Uniformity.

According to the theory of stagnation point flow model in Ref. 34, the boundary layer thickness δ is independent of the radial position and can be given by

$$\boldsymbol{\delta = 3\sqrt{\nu \frac{H_c}{v_{in}}}} \qquad 4.7$$

4.7

where $\boldsymbol{\nu}$ is the kinetic viscosity, $\boldsymbol{H_c}$ is the distance between wafer and showerhead, and $\boldsymbol{v_{in}}$ is the input flow speed from showerhead nozzles. The boundary layer thickness was calculated based on the assumption that $\boldsymbol{v_{in}}$ is uniform on the whole showerhead, so it is no longer applicable in our reactor because the flow speed of inner and outer are independently controlled. However, the formula can still help to understand the mass transfer process taken place in the reactor. Boundary layer can approximately separate convection dominant region and diffusion dominant region. Mass transfer is more efficient through convection than diffusion, so a thinner boundary layer will have a higher surface arrival rate, i.e., a higher growth rate.

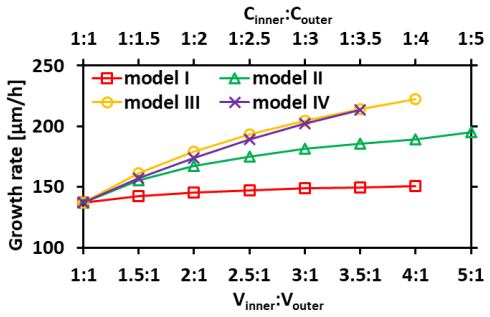

(a)

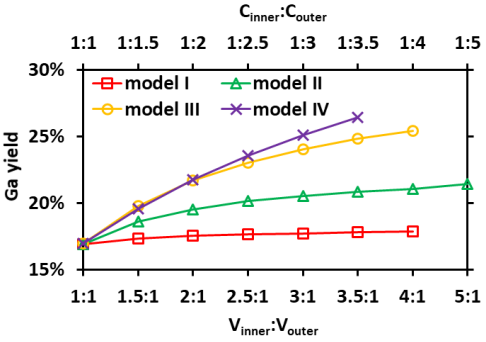

(b)

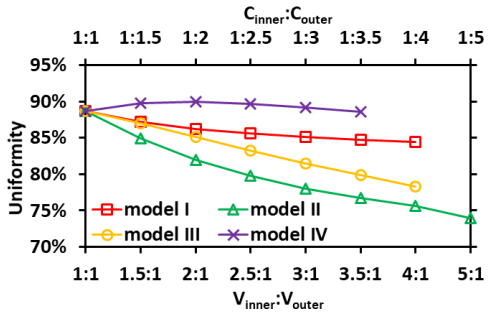

(c)

Figure 4.10 Simulation results for experiment two, (a) growth rate, (b) Ga yield and (c) uniformity.

In the current simulation model, the temperature, pressure, and geometry are fixed, and the input gas velocity $\boldsymbol{V_{input}}$ is the main factor that determines the flow field distribution in the reactor. With the flow field being fixed, increasing GaCl concentration can only increase the growth rate without influencing Ga yield and uniformity because the latter two are only determined by the flow field. With increasing $\boldsymbol{V_{input}}$, more source gas can be transferred to diffusion boundary, diffused to wafer surface, and incorporated into the crystal. Figure 4.9 (a) showed that the growth rate increases with increasing $\boldsymbol{V_{input}}$. But the increase in $\boldsymbol{V_{input}}$ will also lead to higher lateral flow speed, and more source gas may exhaust with lateral flow before they reach the diffusion region. As a result, the Ga yield is decreasing with increasing $\boldsymbol{V_{input}}$, as shown in Figure 4.9 (b). The uniformity is determined by both diffusion dominant region and the convection dominant region. The best uniformity can be achieved with an optimal input flow speed. The uniformity dependency on $\boldsymbol{V_{input}}$ is shown in Figure 4.9 (c).

According to the above analysis, in order to improve the Ga yield, we need to decrease the lateral flow and maintain the GaCl input mass flux. This can be achieved by simply increasing the ratio of $\boldsymbol{V_{inner}}$:$\boldsymbol{V_{outer}}$ and decreasing the ratio of $\boldsymbol{C_{inner}}$:$\boldsymbol{C_{outer}}$. We tried different ratios of $\boldsymbol{V_{inner}}$:$\boldsymbol{V_{outer}}$ in the four models with different ratios of $\boldsymbol{S_{inner}}$:$\boldsymbol{S_{outer}}$ to find the best balance point. The simulation results of $\overline{\boldsymbol{g_r}}$, $\boldsymbol{\eta}$ and $\boldsymbol{DU}$ are shown in Figure 4.10 (a)-(c), respectively.

Both average growth rate and Ga yield are increasing with decreasing the ratio of $\boldsymbol{V_{inner}}$: $\boldsymbol{V_{outer}}$, but uniformity is degraded with decreasing the ratio of $\boldsymbol{V_{inner}}$: $\boldsymbol{V_{outer}}$. Among the four models, model IV has the highest growth rate, Ga yield, and the best uniformity.

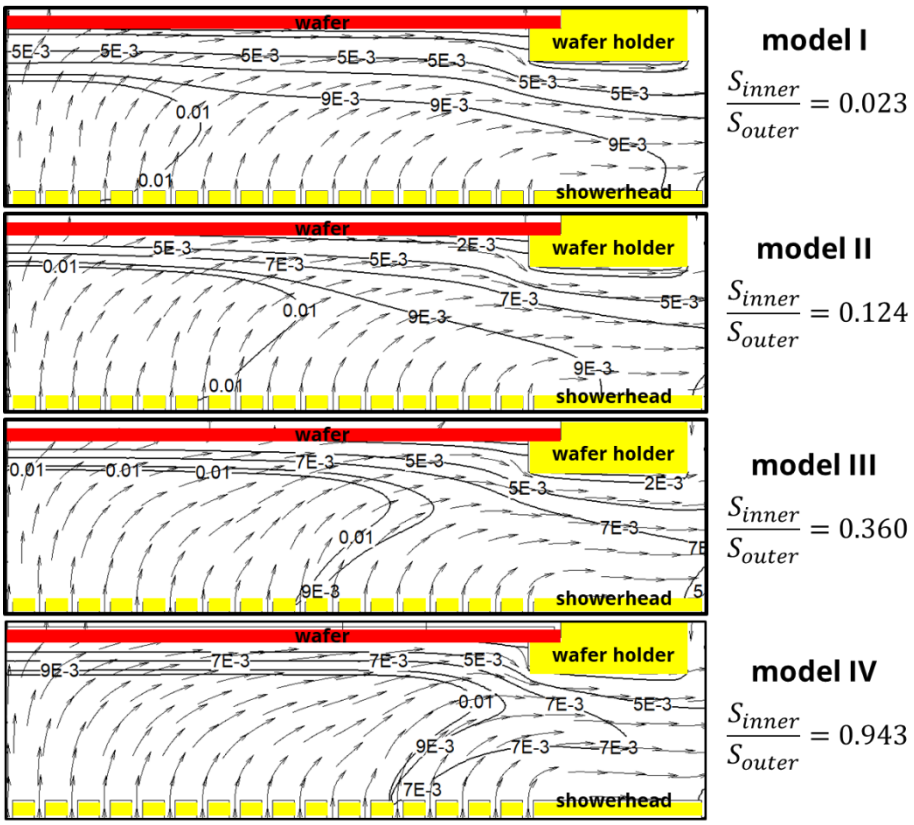

Figure 4.11 Flow lines and GaCl isoconcentration lines for different models with the same input condition of V_{inner}: V_{outer}=1:3.5 (C_{inner}: C_{outer}=3.5:1)

The flow lines and GaCl isoconcentration lines were plotted for model I~IV at the same input condition of $\boldsymbol{V_{inner}}$:$\boldsymbol{V_{outer}}$ = 1: 3.5 ($\boldsymbol{C_{inner}}$:$\boldsymbol{C_{outer}}$ = 3.5: 1), as shown in

Figure 4.11. The inner flow with high concentration and low velocity is the main source that provide GaCl source gas, and the outer flow with low concentration and high velocity is used to help to push the outgoing inner flow near wafer holder up to wafer surface. The GaCl isoconcentration lines uniformly get crowded near wafer surface and the thinnest diffusion boundary layer was achieved with proper inner/outer region area ratio. The optimized condition is the balance point between growth rate, Ga yield and uniformity. The Ga yield may be further increased by decreasing GaCl concentration in the outer flow, but this will surely be compromising the uniformity. To further optimize the uniformity, we need to upgrade the design by decreasing wafer holder size.

4.5 New showerhead demonstration

4.5.1 Design of showerhead version II

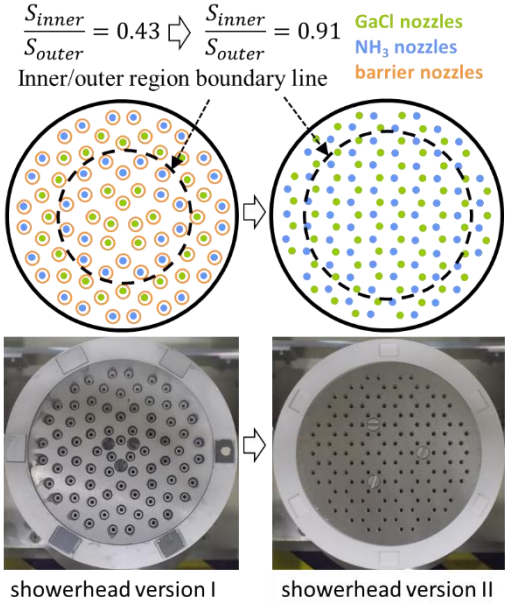

Figure 4.12 Showerhead version I and II comparison

The new showerhead was then designed as shown in Figure 4.12. Compared with showerhead version I, showerhead version II has following changes. Firstly, the source gas nozzle diameter was decreased from 2 mm to 1 mm. Secondly, the total source nozzle number was increased from 75 to 138. Thirdly, the ring type barrier nozzles were

canceled. Fourthly, the GaCl nozzles and NH_3 nozzles arrangement was also changed. And at last, the area ratio of inner to outer region was increased to 0.91 from 0.43.

4.5.2 Experimental demonstration of the new designed showerhead

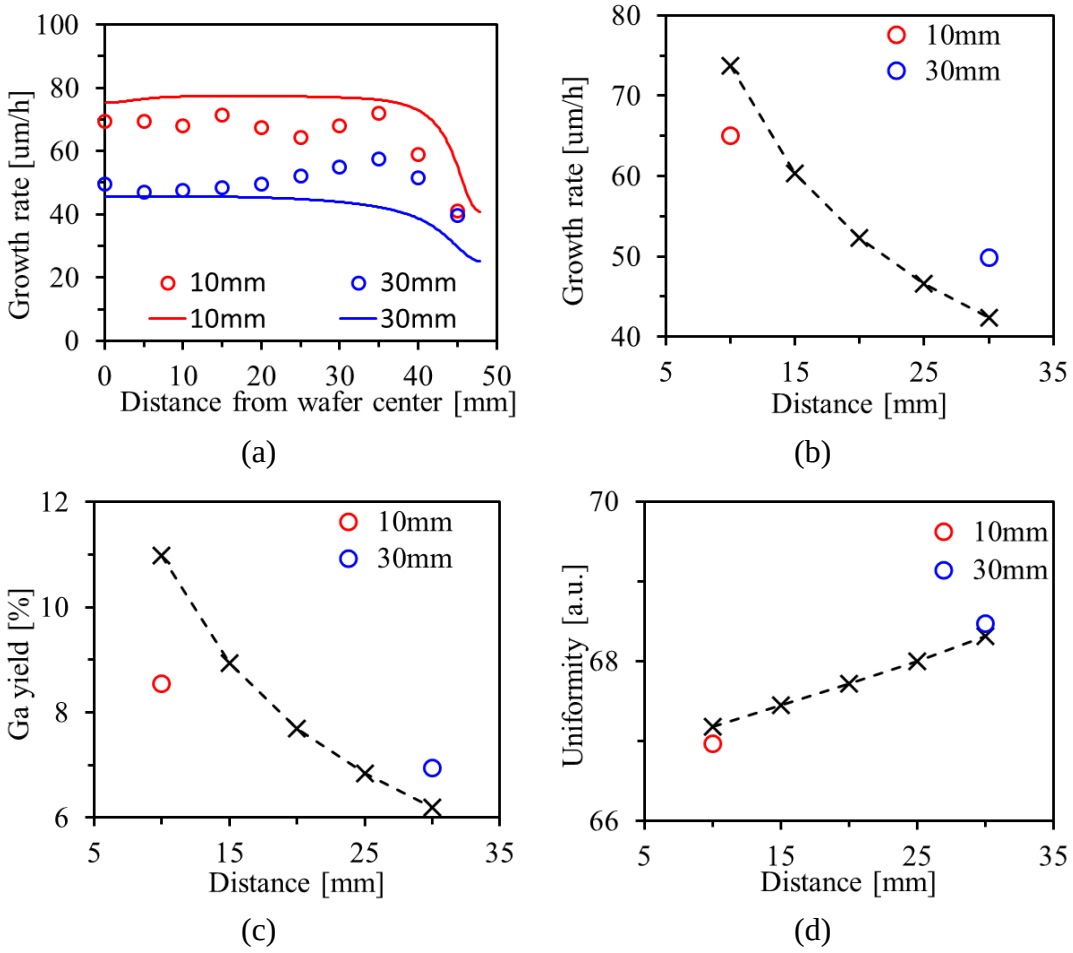

Figure 4.13 Comparison of simulation and experiment result with distance between wafer and showerhead of 10mm and 30mm, (a) growth rate distribution along wafer radius direction, circle is the experiment result, break line is the simulation result; distance dependence of (b) growth rate, (d) Ga yield and (e) uniformity, cross is the simulation result and circles are the experiment result

The distance from wafer holder to showerhead was decreased from 30mm to 10mm with the new showerhead. With the optimized growth condition, 3 experiment with different growth time were carried out at each distance. The substrates were 2 μm MOVPE grown GaN on 4-inch sapphire template. The epilayer thickness was measured by SEM cross section view with accuracy of ±2μm, as shown in Figure 4.13 (a). The

calculated growth rate, Ga yield and uniformity as defined in Formula 4.4 to 4.6 are also plotted in Figure 4.13 (b) to (d).

This result fit with the analytical model proposed in Section 2.3 and the simulation result shown in Section 4.4. The growth rate and Ga yield both increased with smaller distance between wafer and showerhead, with compromising the uniformity. The simulation was also carried out with the simulation model discussed in Section 4.4. The simulation used the same flow condition with the experiment, and the result are also compared in Figure 4.13. To fit the experiment with the simulation, fitting coefficient k was 0.44.

4.5.3 Impurity in the crystal

Table 4.3 SIMS result of epilayer grown with 10mm distance to W plate

Element	H	C	O	Si	Ca	Fe	Mg
Unit	cm^{-3}	cm^{-3}	cm^{-3}	cm^{-3}	cm^{-3}	cm^{-3}	cm^{-3}
Value	$<4\times10^{16}$	$<1\times10^{16}$	$<3\times10^{15}$	$<2\times10^{15}$	1×10^{14}	1×10^{15}	5×10^{16}

With using W plate to prevent parasitic deposition, new impurities may also incorporate into the crystal from W plate. We tried experiment with wafer to showerhead distance of 10mm. The growth was on a 4-inch sapphire template with 2μm MOVPE grown GaN layer. The growth condition was the optimized one, and the growth time was 1 hour. SIMS result of the epilayer is shown in Table 4.3. The Ca impurity is from Ga metal, Fe is from stainless steel part of the reactor, and Mg is from the BN parts in the reactor. No impurity is specifically from W metal.

4.6 Summary of large size wafer growth

The reactor for large wafer growth was introduced, the optimized growth condition was obtained which can achieve film with good uniformity on large wafer area. W catalyst effect to decompose GaN can be enhanced by cycles of aging procedure.

Simulation experiments were performed to study the flow in a vertical HVPE reactor with inner/outer flow independently controlled showerhead configuration. The flow field in the reactor become more complex with extra input flow, but both growth rate and Ga yield can be improved at the same time without compromising the uniformity

by controlling the balance between the two input flows. Besides, Area ratio of inner to outer region was optimized to 0.943, and showerhead version II was designed based on the result.

The experiment result fitted with the simulation result with a fitting coefficient of 0.44. Besides, based on the SIMS result of the epilayer grown 10mm distance away from W plate, it shows that there are no extra impurities from W metal.

4.7 References

[1] *T. Bohnen, H. Ashraf, G.W.G. van Dreumel, S. Verhagen, J.L. Weyher, P.R. Hageman, E. Vlieg, Enhanced growth rates and reduced parasitic deposition by the substitution of Cl2 for HCl in GaN HVPE, J. Cryst. Growth. 312 (2010) 2542–2550. https://doi.org/10.1016/j.jcrysgro.2010.04.010.*

[2] *Ł.J. Sytniewski, A.A. Lapkin, Sergey. Stepanov, W.N. Wang, CFD optimisation of up-flow vertical HVPE reactor for GaN growth, J. Cryst. Growth. 310 (2008) 3358–3365. https://doi.org/10.1016/j.jcrysgro.2008.04.017.*

[3] *Y. Honda, Y. Iyechika, T. Maeda, H. Miyake, K. Hiramatsu, H. Sone, N. Sawaki, Crystal Orientation Fluctuation of Epitaxial-Lateral-Overgrown GaN with W Mask and SiO2 Mask Observed by Transmission Electron Diffraction and X-Ray Rocking Curves, Jpn. J. Appl. Phys. 38 (1999) L1299. https://doi.org/10.1143/JJAP.38.L1299.*

[4] *H. Sone, S. Nambu, Y. Kawaguchi, M. Yamaguchi, H. Miyake, K. Hiramatsu, Y. Iyechika, T. Maeda, N. Sawaki, Optical and Crystalline Properties of Epitaxial-Lateral-Overgrown-GaN Using Tungsten Mask by Hydride Vapor Phase Epitaxy, Jpn. J. Appl. Phys. 38 (1999) L356. https://doi.org/10.1143/JJAP.38.L356.*

[5] *M. Haino, M. Yamaguchi, H. Miyake, A. Motogaito, K. Hiramatsu, Y. Kawaguchi, N. Sawaki, Y. Iyechika, T. Maeda, Buried Tungsten Metal Structure Fabricated by Epitaxial-Lateral-Overgrown GaN via Low-Pressure Metalorganic Vapor Phase Epitaxy, Jpn. J. Appl. Phys. 39 (2000) L449. https://doi.org/10.1143/JJAP.39.L449.*

[6] *L.V. Gurvich, I.V. Veyts, C.B. Alcock, Institut vysokikh temperatur (Akademiia nauk SSSR), Gosudarstvennyĭ institut prikladnoĭ khimii (Soviet Union), Thermodynamic properties of individual substances, Hemisphere Pub. Corp., New York, 1989. http://books.google.com/books?id=EaQRAQAAMAAJ (accessed January 9, 2020).*

[7] *L.V. Gurvich, I.V. Veyts, C.B. Alcock, Thermodynamic Properties of Individual Substances: Volume 3, CRC-Press, 1994.*

Chapter 5

5 Conclusions and future outlook

5.1 Conclusions

In this dissertation, I have achieved 2.3 mm thick GaN epilayer growth by halide vapor phase epitaxy method with (0002) and ($10\bar{1}2$) rocking curve of 72.7 and 32.0 arcsec in a home-made reactor. The growth was achieved by optimizing of the growth condition, selecting the best seed, and protecting the edge with a W ring.

There are mainly two goals for growth condition optimization, i.e., a higher growth rate and less parasitic deposition on the nozzle. To achieve these two goals, firstly the thermal dynamic calculation was proceeded to study the reaction near Ga liquid surface and wafer growth surface. Secondly analytical equations of the stagnation point flow model and a simulation model were used to study the mass transportation in the reactor. Thirdly experimental comparison of three different growth conditions was performed. The maximum growth rate was 280 μm/h and the parasitic deposition on the nozzles were minimized.

By comparing the homoepitaxial crystal growth on seeds fabricated by different methods, three important facts were found out. Firstly, the epilayer can succeed the crystallinity from the substrate, i.e., epilayer on the substrate with higher crystallinity will also result in a better crystallinity. Secondly, the stress for all the seeds will increase after epilayer growth regardless of the substrate is under compressive stress or tensile

stress. Thirdly, the dislocation bundles generated at interface will worsen the epilayer quality. Considering the above three facts, ammonothermal substrate was finally selected for thick epilayer owning to its supreme advantages in high crystallinity, flat lattice bow and no dislocation bundle generation at interface.

By comparing the protection rings made of four kinds of different material in the growth experiments. W ring was selected to protect the seed edge and fix the seed position for long time growth mainly owing to its catalytic effect in preventing parasitic deposition.

Besides for thick epilayer growth, a reactor for large size wafer growth was also introduced. The reactor is a vertical one with independent inner/outer flow-controlled showerhead configuration. With an optimized growth condition, the reactor can achieve film with good uniformity on large wafer area. Simulation model was used to study the flow in the reactor and it demonstrated that both growth rate and Ga yield can be improved at the same time without compromising the uniformity by controlling the balance between the two input flows. By optimizing the inner/outer area ratio, increasing nozzle density, and decreasing nozzle size, new version of the showerhead was designed based on the result.

W metal was used in both reactors owning to its catalyst effect to decompose GaN. It is found that this effect can be enhanced by cycles of aging procedure. Besides, based on the SIMS result of the epilayer grown 10mm distance away from W plate, it shows that there are no extra impurities from W metal.

5.2 Future perspective

5.2.1 Thick epilayer growth

The key to further improve the critical thickness with current approach is to prevent lateral growth in non-polar and semi-polar directions. Although W ring was not

effective in this dissertation, but I still think physical fixation is not yet thoroughly studied. The “growth cannel” configuration shown in Figure 3.16 is expected. This design may both prevent the lateral growth and keep the flow filed stable during the whole growth time.

The stress is currently limiting the critical thickness of the epilayer, and it is found that the stress will always increase regardless whether the stress in the seed is compressive or tensile. Micro-Raman and other evaluation methods should be used to further analyze the stress in the crystal. After understanding the mechanism of the generation of stress during epilayer growth, countermeasures can be taken to further decrease the stress increasing and enlarge the critical thickness of the epilayer.

To further decrease the TDD in epilayers on native GaN seed, dislocation movement at interface need to be further studied.

5.2.2 Large size wafer growth

We have fitted the experiment result with simulation, and further effort need to be done in following aspects.

1. Aged W catalytic effect to prevent parasitic deposition in long time growth.
2. Higher growth rate for long time growth.

Besides, further optimization of showerhead configuration design and flow condition is expected to combine with machine learning. This will greatly improve the research efficiency.

Eventually, with thoroughly study the above aspects, large size (4-inch even 6-inch) bulk crystal with uniform thickness distribution, with thickness in centimeter level, and dislocation level lower than 10^4 cm^{-2} is expected.

Appendix

Appendix I: Thermal dynamic data for species involved in a GaN HVPE reactor

For an individual substance, its Gibbs free energy $G(P,T)$ is a function of pressure P and temperature T, and can be defined as formula I.1.

$$G(P,T) = G^0(P_0,T) + \int_{P_0}^{P} \left(\frac{\partial G}{\partial P}\right)_T dP \qquad \text{I. 1}$$

where $G^0(P_0,T)$ is the Gibbs thermodynamic potential taken at the standard pressure of 1 atm. From Ref. [1,2], $G^0(P_0,T)$ can be approximated by a polynomial

$$G^0(P_0,T) = H(298K) - T\cdot\left(\varphi \ln\chi + \sum_{k=-2}^{3} \varphi_k \chi^k\right) \qquad \text{I. 2}$$

and

$$\chi = T/10^4 \qquad \text{I. 3}$$

For reaction shown in formula I.4

$$aA + bB \leftrightarrow cC + dD \qquad \text{I. 4}$$

its Gibbs free energy change $\Delta G^0(P_0,T)$ can be calculated by formula I.5

$$\Delta G^0 = c\cdot G_C^0 + d\cdot G_D^0 - a\cdot G_A^0 - b\cdot G_B^0 \qquad \text{I. 5}$$

The thermodynamic properties of each species involved in GaN HVPE reactor is listed in Table I.1. All the data are applicable in the range of 298K to 3000K at the standard pressure of 1 atm.

Table I.1 Thermodynamic data of 10 species involved in HVPE reactor

Species	H 298K	φ	φ_{-2}	φ_{-1}	φ_0	φ_1	φ_2	φ_3
Ga (l)	0	26.24945	0.001124	0.147769	126.5938	-3.3068	7.960486	-4.11799
H_2 (g)	0	29.50487	0.000168	0.860656	205.5368	-14.9531	78.18955	-82.7898
N_2 (g)	0	21.47467	0.001749	0.591004	242.8156	81.08497	-103.627	71.30775
GaCl (g)	-70553	37.11052	-0.00075	1.160651	332.2718	4.891346	-4.46759	5.506236
$GaCl_2$ (g)	-241238	57.74584	-0.00227	1.875555	443.2976	3.66186	-9.35634	15.88245
$GaCl_3$ (g)	-431573	82.03355	-0.00349	2.685592	526.8113	8.278878	-14.5678	12.8899
Ga_2Cl_6 (g)	-957552	180.9567	-0.00772	5.923436	945.776	14.74793	-26.2997	23.6243
HCl (g)	-92310	23.15984	0.00182	0.614738	243.9878	51.16604	-36.895	9.174252
NH_3 (g)	-45940	20.52222	0.000716	0.767724	231.1183	244.6296	-251.69	146.6947
GaN (g)	-114000	52.86351	-0.00799	2.113389	160.2647	1.313428	-2.44113	1.945731

Appendix II Reference

[1] L.V. Gurvich, I.V. Veyts, C.B. Alcock, Institut vysokikh temperatur (Akademiia nauk SSSR), Gosudarstvennyĭ institut prikladnoĭ khimii (Soviet Union), Thermodynamic properties of individual substances, Hemisphere Pub. Corp., New York, 1989. http://books.google.com/books?id=EaQRAQAAMAAJ (accessed January 9, 2020).

[2] L.V. Gurvich, I.V. Veyts, C.B. Alcock, Thermodynamic Properties of Individual Substances: Volume 3, CRC-Press, 1994.

Acknowledgment

This paper is carried out during my study in Department of Electronics, Graduate School of Engineering, Nagoya University, from April of 2017 to March of 2020. On the completion of my thesis, I would like to express my gratitude to all those whose kindness and advice have made this work possible.

First and foremost, I would like to express my sincere gratitude to my supervisor, Professor Hiroshi Amano, for his encouragement extended throughout the study. He is respectable, responsible, and resourceful scholar, who has provided me with valuable guidance in every stage of writing this dissertation. Without his enlightening instruction, impressive kindness, and patience, I could not have completed my dissertation. His keen and vigorous academic observation enlightens me not only in this dissertation but also in my future study.

I would like to express my sincere gratitude to Professor Michał Boćkowski, a funny person who can always keep optimistic, for his selfless help on my research and life. He is my tutor for crystal growth and gave me lessons which helped me to rapidly build a knowledge frame of crystal growth. He is also an experienced who shared me a lot of valuable experience in crystal growth.

I would like to express my sincere gratitude to Professor Zlatko Sitar, a wise and strict person, for his help in my research. He can always provide ideas that can enlighten me when I feel there no way to go. He is an expert in designing and commissioning of reactors and I have learnt a lot from him.

I would like to express my sincere gratitude to Professor Yoshinao Kumagai, Professor Akira Usui, Professor Yusuke Mori, Professor Masayuki Imanishi, Dr. Miki Moriyama, Dr. Kazuyoshi Iida for their valuable advices on this work.

I would like to express my sincere gratitude to Professor Yoshio Honda, a knowledgeable and conscientious person, who not only guided me in the scientific writing but also gave me a lot of valuable advices in my research.

I would like to express my sincere gratitude to my adviser Professor Shugo Nitta. He is a knowledgeable and kind person who guided me both on research and about my life in Japan. The discussions and feedbacks on my research work and his extensive experience in research guided our research group of HVPE. He is also a barrel of laugh and made me always feel relaxed and happy to do research together with him.

I would like to express my sincere gratitude to Mr. Naoki Fujimoto, who is senior in our HVPE research group, for his help at the beginning of my research work. He taught me how to manipulate the reactor and basic evaluation equipment such as SEM. He is always kind and helpful not only on research but also on my life.

I would like to express my sincere gratitude to Professor Manato Deki, Professor Maki Kushimoto and Professor Atsushi Tanaka for their scientific conversation for making the research work easier in this laboratory.

I would like to express my sincere gratitude to the secretaries in Amano laboratory for their excellent work for making the laboratory such an enjoyable place to work.

I would like to express my sincere gratitude to Jian Shen, Jia Wang, Zhibin Liu, Xu Yang, Zheng Ye, Nan Hu, Yaqiang Liao, Ting Liu, Guohao Yu, Wentao Cai and Donglin Wu, who helped me with my research and take company in my life in Japan. I did not feel lonely owing to their company.

I would like to express my sincere gratitude to Kazuki Ohnishi and Yuki Amano, who also contributed a lot in HVPE research group and enlightened me on my own research.

I would like to gratefully acknowledge Department of Electrical and Electronic Engineering, Faculty of Engineering, Nagoya University for providing the resources and needs during the dissertation. I would like to extend my appreciation to Professor Jun Suda, Professor Toru Ujihara and Professor Hideto Miyake for their unconditional help and comments for writing this dissertation.

Finally, I would like to express my deepest gratitude towards my parents and my wife for their unconditional support, understanding and enduring patience.